TELESEISMIC P AND S WAVE ATTENUATION CONSTRAINTS ON TEMPERATURE AND MELT OF THE UPPER MANTLE IN THE ALASKA SUBDUCTION ZONE

A Thesis

Presented to the Faculty of the Graduate School

of Cornell University

In Partial Fulfillment of the Requirements for the Degree of

Master of Science

by

Roque Alberto Soto Castaneda

May 2020

ABSTRACT

Recent broadband deployments in Alaska provide an excellent opportunity to advance our understanding of the Alaska-Aleutians subduction system, with implications for subduction processes worldwide. Seismic attenuation, measured from teleseismic body waves, provides a strong constraint on thermal structure. We measure P and S wave attenuation from pairwise amplitude and phase spectral ratios for teleseisms recorded at 204 stations including the WVLF (Wrangell Volcanics & subducting Lithosphere Fate) array. This study applies a novel method for measuring teleseismic attenuation by Eilon and Abers (2017) to subduction zones for the first time and the results are encouraging. Low attenuation across both the WVF and east of the Alaska Range suggest Yakutat subduction beneath the WVF and Pacific/Yakutat subduction extending past the east edge of the Alaskan-Aleutians Wadati-Benioff zone. Comparison with previous Alaska attenuation studies shows slightly higher attenuation, which are likely due to a difference in paths sampled.

BIOGRAPHICAL SKETCH

Roque was born in Caracas, Venezuela to his parents Natalie Marshall and Roque Soto. He has two younger siblings, Maya Marshall and Sebastian Soto. In 2003 he moved to the south Florida where he later graduated from Atlantic Community High School's IB Programme. Roque then earned his Bachelor of Science degree *cum laude* from Brown University in Geology: Physics and Mathematics in May 2016. He began attending Cornell University in August 2016 and entered the Geophysics PhD program. In July 2018 he went on leave from Cornell University to work as a Geologist in Philadelphia. Then, in January 2019 he enrolled in the University of Pennsylvania's Masters' in Computer and Information Technology program. After graduating from Cornell, he plans to continue his work & studies in computer and information technology in Pittsburgh.

Dedicated to Marisa Millenson and Percy Soto Castaneda, whose support made the completion of this thesis a reality.

ACKNOWLEDGMENTS

SOMETHING ABOUT NSF?

This project is funded by NSF grant EAR-1460291 for support of the Wrangell Volcanics & Lithospheric Fates (WVLF) project. All data was collected through the IRIS-PASSCAL Instrument Center and all waveform data are archived at the IRIS Data Management Center. Thanks to my advisor, Dr. Geoffrey Abers, for his continuous support and encouragement throughout this project, without his guidance and patience, none of this could have been possible. Thanks as well to Dr. Katie Keranen for her flexibility and assistance as a part of my committee. Many thanks to Dr. Zachary Eilon and all of my labmates - Michael Mann, Jade Crosbie, Nate Stevens, Dana Peterson, Cat Lambert and Doyeon Kim for all of their help and support through these past several years. Special thanks to Dr. Doug Christensen and Dr. Carl Tape for their help in obtaining the data for WVLF and SALMON that was used in this study. My fondest appreciation and gratitude to Marisa Millenson for her love and support through both exciting and trying times.

TABLE OF CONTENTS

CHAPTER 1

INTRODUCTION AND BACKGROUND

1.1 Introduction

In subduction zones around the world, a range of interconnected processes are responsible for the location and activity of volcanic arcs, such as dehydration of the subducting slab inducing flux melting in the mantle wedge (Pearce et al. 1995; van Keken 2003; Grove et al. 2006; van Keken et al. 2011). Other processes like slab truncation, tearing and windows can complicate these processes further by producing 3D flow and inducing mantle upwelling (Cross and Pilger 1982; Thorkelson 1996; Campos et al. 2008; Jadamec and Billen 2012). Unusual or unexplained volcanism can often be a result of these complicated interactions, and only by accurately sensing the extent of subduction with tools like attenuation can we narrow down the causes for volcanism. Attenuation's sensitivity to temperature (Anderson et al, 1965; Jackson et al. 2002), and melt (Takei 2000; Dalton et al. 2009) make it an exceptionally useful tool for imaging cold subducting slabs, hot mantle wedges, and any accompanying melt production.

South central Alaska experiences a broad range of volcanism from the Aleutian subduction in the southwest, to the mostly amagmatic Alaskan range in the center and the active Wrangell Volcanic Field (WVF) in the southeast. The Aleutian subduction along the Cook Inlet and the Alaskan Range have been studied in the past using a combination of focused and regional seismic datasets measuring seismic velocity and attenuation (Stachnik et al. 2004; Eberhart-Phillips 2006; Kim et al. 2014; Wang and Tape 2014), but the limited coverage of the datasets prevented the resolution of results in key areas like around the WVF and directly east of the edge of the Alaskan Range. The expansion of the USArray Transportable Array (TA) to south central Alaska from 2014 to 2020 has led to many recent teleseismic velocity studies that

attempt to better characterize the whole south central Alaska region using the broad coverage of stations (Martin-Short et al, 2016; Jiang et al. 2018; Martin-Short et al. 2018). These studies have much greater resolution than previous ones but are still constrained by the 85 km spacing used by the TA. Even in these recent studies there has been disagreement regarding the eastward extent of Pacific slab subduction east of the Alaskan Range, and whether the Yakutat slab extents beneath the WVF or not.

By measuring attenuation using a mix of TA, regional, and focus arrays like the WVLF (Wrangell Volcanism and Lithospheric Fate) (Abers et al., 2019) array to boost resolution in key areas like the WVF, this study provides the first teleseismic attenuation results across all of south central Alaska and address the disagreement of recent studies in the region. To measure attenuation, this study uses a method pioneered by Eilon and Abers (2017) to measure teleseismic attenuation at a mid-ocean ridge and applies it to a subduction zone. Using this method in combination with TA allows us to measure attenuation without resolution and coverage limitations due to any paucities of local seismicity that might hamper previous attenuation studies using local seismicity. By comparing the attenuation results in tectonically complex to tectonically simple areas this study can provide attenuation constraints to previous studies of South-Central Alaska. Not only will these constraints help resolve open questions about local tectonics (Jiang et al. 2018; Martin-Short et al. 2018), but this method can also serve as a roadmap for future attenuation studies to provide new insight into other subduction regions around the world.

1.2 Tectonic Background

South-Central Alaska is a region that has been dominated by plate boundary dynamics shaped by two main collisional events, the Mesozoic collision of the Wrangellia composite

terrane and the Cenozoic collision of the Yakutat terrane (Plafker and Berg 1994; Trop and Ridgway, 2007 Jadamec et al. 2013). The Wrangellia composite terrane is composed of the metamorphosed Middle to Late Jurassic retroarc basin strata of the Talkeetna oceanic arc, which through oblique subduction in the Early Cretaceous were thrust onto the western continental margin of North America. (Plafker and Berg 1994; Trop and Ridgway, 2007; Colpron et al. 2007;). The Yakutat terrane is a micro-plate and originated as a fragment from western North America comprised of accretionary complex rocks and an overthickened oceanic plateau, which has been colliding with the North American continent, alongside the Pacific plate, from the Oligocene to the present, creating the largest coastal mountain range on Earth (Bruns 1983; Plafker 1987; Brocher et al. 1994; Nockleberg 2001; Trop and Ridgway, 2007; Christeson et al. 2010; Worthington et. al 2012). These collisional events have resulted in the orogenic growth and deformation of the North American continental crust through magmatism and accretion and continue to do so in the present day with the partial accretion and subduction of the Yakutat terrane (Plafker and Berg 1994; Colpron et al. 2007; Haeussler 2008; Worthington et al. 2012). The exposed section of the Yakutat terrane presently lies mostly offshore southern Alaska in the Gulf of Alaska, bounded by the Fairweather fault in the north and the Transition fault to the south (Plafker and Berg 1994; Nockleberg 2001). The Yakutat terrane is marked by markedly thick crust of 17-30 km (Christeson et al. 2010; Worthington et al. 2012) that thickens to the east. The Yakutat basin overlies the Yakutat terrain and is comprised various Cenozoic sedimentary strata of approximately 10 km in thickness combined (Trop and Ridgway 2007).

The Aleutian subduction zone in the west end of the region is caused by Pacific plate subduction under the North American plate and extends for several thousand kilometers westward, causing extensive arc volcanism throughout with short trench-arc distances that

increase with slab dip shallowing that begins just west of the Cook Inlet.(Eberhart-Phillips et al., 2006; Kim et al. 2014; Wang and Tape 2014). Subduction-related mountain building and the resulting forearc flexing of the North America plate led to the formation of the Cook Inlet Basin. The basin is an elongate fault-bounded forearc basin extending from the Matanuska Valley south along the Alaskan Peninsula, with sedimentary thicknesses randing from 7.5 kilometers in the Kenai area to 450 meters or less in the Seldovia Arch (Plafker and Berg 1994; Swenson 1997). At the northeast end of the Aleutian subduction zone, the partial subduction of the Yakutat terrane has been linked to flat-slab subduction in the region (Page et al., 1989; Ratchkovski and Hansen, 2002; Ferris et al. 2003; Eberhart-Phillips et al., 2006; Fuis et al. 2008; Jadamec and Billen 2012;). This flat-slab subduction geometry has led to the development of long trench-arc distances and a zone of volcanic quiescence known as the Denali Volcanic Gap (DVG) (Plafker and Berg, 1994; Preece and Hart 2004; Eberhart-Phillips et al., 2006; Rondenay et al. 2010; Worthington et al. 2012; O'Driscoll and Miller, 2015; Martin-Short et al., 2016). The DVG stretches from the easternmost Aleutian Arc volcanism of Mt. Spurr to the Buzzard Creek craters located at the edge of the Alaskan-Aleutian Wadati-Benioff Zone (WBZ) shown in Figure 1.1 and aligns with the northwest extent of the Yakutat terrane. (Plafker and Berg, 1994; Eberhart-Phillips 2006; Hayes et al. 2018).

Although the Aleutian subduction WBZ ends just east of the Buzzard Creek craters as seen by the local seismicity derived slab contours on Figure 1.1, recent analysis of teleseismic Rayleigh wave tomography (Wang and Tape 2014), joint Rayleigh and teleseismic S wave tomography (Jiang et al. 2018), and ambient noise tomography (Ward 2015), indicate a high velocity anomaly extending 85-100 km past the edge of the WBZ but still within the limits of the potential Yakutat slab as described by Eberhart-Phillips et al. (2006) and within the tectonic

tremor zone identified by Wech (2016). These results stand in contrast to another recent joint ambient noise, earthquake-based surface wave, P-S receiver function tomography model and teleseismic S wave model (Martin-Short et. al 2018) which does not report the high velocity anomaly. The same studies also disagree over the extent of the slab beneath the Wrangell Volcanic Field (WVF), with some suggesting the WVF lies above the truncated edge of the slab (Martin-Short et al. 2018), and some suggesting the subducting Yakutat slab extends beneath the WVF towards the northeast (Jiang et al. 2018). The recent studies all report a possible connection to the main Alaskan-Aleutian subduction, particularly at shallower depths (Jiang et al. 2018, Martin-Short et. al 2018, Wang and Tape 2014).

The WVF contains several active volcanoes younger than 25 Ma (Richter et al. 1990) with atypical geochemical composition for a subduction zone (Preece and Hart 1994). Three geochemical trends that provide possible origins for the magmatism as defined by Preece and Hart (2004) include calk-alkaline lavas derived from high partial melt of a mantle wedge MORB source; another suite of calk-alkaline lavas containing adakites suggestive of slab melting; and finally tholeiitic lavas that have been inferred to derive from low partial melt of anhydrous mantle wedge material. The seismic observations in combination with the geochemical trends suggest the seismically imaged subducted slab correlates to the truncated edge of the Yakutat terrane (Martin-Short et al, 2018; Jadamec and Billen 2012, 2010).

1.3 Seismic Attenuation

An alternative measurement to seismic velocity for gauging the effect of the material properties on the seismic signal is seismic attenuation. In contrast to seismic velocity, attenuation is potentially more sensitive to temperature (Anderson et al, 1965; Jackson et al. 2002), less sensitive to major element composition (Darot and Gueguen 1981; Faul and Jackson, 2005), and

more sensitive to water (Jackson et al. 1992; Karato 2006) and melt (Takei 2000; Dalton et al. 2009; Abers et al., 2014). Because of these qualities, attenuation has been used in previous studies to image subduction zones (Roth et al. 1999; Stachnik et al. 2004; Pozgay et al. 2009; Wei et al. 2018). This study will use novel techniques to obtain the first teleseismic attenuation measurements in several complex areas of Alaskan-Aleutian and WVF subduction regions and interprets these alongside travel time arrival results.

1.3.1 Measuring Attenuation

Seismic attenuation measurements are often used to narrow down the non-unique interpretations of velocity results. While seismic velocities in the non-dissipative regime depend nearly linearly on temperature (Romanowicz, 1995), attenuation has been shown to depend on 1/temperature (Anderson et al, 1965; Jackson et al. 2002). Temperatures below approximately 900° C show little effect on attenuation, while temperatures greater than 1000° C show a large impact (Jackson et al. 2002), making attenuation particularly effective at imaging temperature at subduction zone temperatures. The presence of melt also plays a large role in subduction zones (Abers et al. 2014), though experiments suggest that the mechanism of melt transport plays an important role in determining the effects on attenuation and velocity (Dalton et al. 2009). In the case of “melt squirt”, where stress relaxation occurs due to pressure differences between neighboring melt inclusions driving fluid flow, experiments show little effect on attenuation, but noticeable effect on shear velocities (Hammond and Humphreys 2000a,b). On the other hand, grain-boundary sliding enhanced by small amounts of melt increases attenuation but reduces velocities less (Jackson et al. 2004; Dalton et al. 2009; McCarthy et al. 2011; Holtzman 2016). Lab experiments also indicate major element composition plays a minor role on attenuation unlike on velocities (Darot and Gueguen 1981; Faul and Jackson, 2005). In contrast experiments

have shown the addition of water increases attenuation while having a small effect on velocity (Jackson et al. 1992; Karato 2006), although oxygen fugacity may be more critical than the percentage of water (Cline et al., 2018). Because of attenuation's sensitivity to these different mechanisms and properties, the results of this study will provide important complementary information to better interpret existing velocity results.

Seismic wave attenuation Q^{-1} is defined as the loss of energy per cycle. This loss of energy can be caused by anelastic effects (intrinsic attenuation) or by scattering (extrinsic attenuation) as the seismic wave travels from the point of origin to its destination (Aki and Richards, 1980). The intrinsic effect of attenuation on seismic waves can be explored using the solution to the one-dimensional wave equation (Stein and Wysession, 2003):

$$u(x,t) = A(t)\cos\left(\omega\left(t - \frac{x}{c}\right)\right), \quad (1)$$

Where u(t) is the displacement of a mass, A(t) is the amplitude, t is time, x is displacement, c is the intrinsic velocity and ω is the angular frequency. Physical dispersion is accounted for by a frequency-dependent phase velocity c (e.g., Minster & Anderson, 1981). The above equation can used to express the change in amplitude over time as a result of attenuation as follows:

$$A(t) = A_0 e^{-\omega_0 t/2Q}, \quad (2)$$

Here A_0 is the amplitude constant, ω_0 is the natural frequency of the oscillating mass and Q is the quality factor (the inverse of which is attenuation). This equation shows the two key effects of attenuation on a seismic wave signal, both a decay in overall amplitude as a result of the exponential term as well as a change a frequency by an amount depending on the quality factor

Q (Stein and Wysession, 2003). The anelastic effects that cause intrinsic attenuation, and thus changes in amplitude and phase, reflect properties of the earth along the seismic wave's path.

Intrinsic attenuation can be broken down into shear (Q_μ^{-1}) and bulk (Q_κ^{-1}) modulus attenuation depending whether the source of attenuation is relaxation of the shear or bulk modulus at seismic frequencies (Anderson and Hart, 1978). In body wave studies of attenuation, P and S body waves attenuate as Q_P^{-1} and Q_S^{-1} respectively (Aki and Richards, 1980). Whereas $Q_S^{-1} = Q_\mu^{-1}$ because all S phase attenuation is due to shear modulus relaxation, Q_P^{-1} can be described as a combination of both bulk and shear (Anderson and Hart, 1978):

$$Q_P^{-1} = \frac{4}{3}(V_S/V_P)^2 Q_S^{-1} + \left[1 - \frac{4}{3}\left(\frac{V_S}{V_P}\right)^2\right] Q_\kappa^{-1}, \quad (3)$$

where V_S and V_P are the S and P body wave phase velocities respectively. Observed Q_κ^{-1} values can range from negligible to as large as the shear attenuation values (Roth et al. 1999; Stachnik et al. 2004; Pozgay et al. 2009). Often Q_P^{-1} values are easier to measure than Q_S^{-1} values because ray paths from smaller events passing through regions of extremely high attenuation do not produce clear S waves (Roth et al. 1999). In addition, S phase results will include the P phase coda, making the signal noisier (Tilmann et al. 1998). The drawback is that Q_P^{-1} values are more difficult to interpret because it contains a bulk attenuation component Q_κ^{-1} and there is no agreement yet on the relevance of the bulk dissipation attenuation band to seismic frequencies (Ricard et. al 2009; Li, 2010; Durand et al. 2012). As a result, most physical models show shear (Q_μ^{-1}) and not bulk (Q_κ^{-1}) attenuation results.

Attenuation can be measured from surface waves (Dalton et al. 2009; Romanowicz, 2002), body waves of teleseismic events (Eilon and Abers, 2017; Cafferky and Schmandt 2015)

or from the body waves of local events (Stachnik et al. 2004; Roth et al. 1999). Surface-wave measurements have the advantage of providing good vertical resolution in comparison to body waves but suffer from lateral smearing and finite-frequency effects, a large drawback where temperatures show large variations over short lateral distances. Body wave measurements of attenuation are used in this study to provide good lateral resolution. Local earthquake attenuation measurements of body waves at subduction zones are more common (Stachnik et al. 2004; Roth et al. 1999, Rychert et al. 2008, Liu et al. 2014), because they provide absolute measurements of Q^{-1} and subduction zones are notoriously seismically active. However, because the region covered by this study contains several zones of interest with little to no seismic activity, we choose to calculate measurements of teleseismic body wave attenuation.

Attenuation is measured through the path-averaged attenuation operator t^* (Romanowicz and Mitchell, 2007). Like travel time, it is an integrated measurement along the raypath. The equations for t^* and T are as follows:

$$t^* = \int \frac{dL}{QV}, \tag{4}$$

$$T = \int \frac{dL}{V}, \tag{5}$$

Where integrals are along the ray paths, t^* and T are the path averaged attenuation operator and travel time respectively, dL is the incremental path length, V is the seismic velocity for the relevant phase, and Q is the quality factor. In general, both V and Q will vary along the ray path. The above equation can be used to convert measurements in t^* to a path-averaged attenuation $\bar{Q}^{-1}$ via as $\bar{Q}^{-1} = t^* \bar{V}/L$ for path length L and path-averaged velocity $\bar{V}$.

Complications arise in measuring t* as shown in experimental (Jackson and Faul, 2010) and observational (Sipkin and Jordan, 1979; Lekic et al. 2009) studies which indicate a possible frequency dependence of attenuation. The frequency dependence is often described as (Anderson and Minster 1979):

$$Q(\omega) = Q_0 \omega^{\alpha}, \quad (6)$$

Where α describes the frequency dependence, usually measured to be in the range of 0 to 0.5 (Fang and Müller, 1991; Lekic et al. 2009).

1.3.2 Previous Attenuation Studies

Studies of attenuation have been performed in many subduction zones including the Central Andes (Haberland and Rietbrock 2001), Tonga (Roth et al. 1999; Wei and Wiens 2018), Central America (Rychert et al. 2008), New Zealand (Eberhart-Phillips et al. 2008), Japan (e.g. Nakajima 2014; Liu et al. 2014; Liu and Zhao 2015), the Marianas (Pozgay et al. 2009), Italy (De Siena et al. 2010) and Alaska (Stachnik et al. 2004), among others. The seismically active nature of these subduction zones allows local earthquakes to be used for measuring attenuation (Rychert et al. 2008; Chen and Clayton 2012; Bohm et al. 2013; Liu et al. 2014; Stachnik et al. 2014).

Local earthquake studies often calculate t^* values for S and/or P phases from spectral amplitudes, fitting a version of equation (2), simultaneously solving for source terms, and using these to calculate Q (Roth et al. 1999). The reported Q values differ depending on whether a frequency independent (Roth et al. 1999; Liu et al. 2014; Chen and Clayton 2012) or dependent (Stachnik et al. 2004; Rychert et al. 2008) equation for Q is used, and on what frequency Q is

fixed to when a frequency dependence is assumed. Following frequency dependent studies this study reports a Q fixed at 1 Hz.

One of the predominant patterns observed in subduction studies of attenuation are low attenuation (high Q) regions in the forearc and slab with Q_P values generally larger than 500 (Bohm et al. 2013; Haberland and Rietbrock 2001). These low attenuation regions have been attributed to the low temperature in the subducting slab and the nose of the mantle wedge (Abers et al., 2006; van Keken et al. 2018). Other common observations are a highly attenuating (low Q) mantle wedge (beneath the arc and backarc) with Q_P values generally lower than 150 (Roth et al. 1999; Haberland and Rietbrock 2001; Bohm et al. 2013). The high-attenuation portions of the mantle wedge under the arc and back-arc have been attributed to a combination of high temperatures enhanced by the presence of fluid in the form of melt (Abers et al., 2014) or H_2O as impurities in anhydrous minerals (Karato, 2003), although recent studies suggest that it is not H_2O but instead increased oxygen fugacity (Cline et. al, 2018).

Attenuation studies outside of subduction zones often lack the seismicity to measure upper mantle attenuation using the local earthquake methods typically used in subduction zones. Because of this limitation different methods have been used to calculate attenuation, such as use of surface wave attenuation at the regional (Dutta et al. 2004; Yang et al. 2007) and global scales (Dalton et al. 2006) and use of differential teleseismic body-wave attenuation (e.g., Li and Cormier, 2002; Cafferky and Schmandt 2015; Dong and Menke, 2017). A limitation of all attenuation studies is the contamination of amplitudes by elastic focusing effects contributing to apparent attenuation through extrinsic attenuation (Romanowicz and Mitchell, 2007), like long-period focusing (Romanowicz, 1987), short-period defocusing (Allen et al. 1999) or frequency-dependent scattering (Richards and Menke, 1983). Some limitations to surface wave studies are

that their measurements are much lower frequencies and thus larger wavelengths than body wave studies, and as a result the structures resolved are of larger scale. This limitation is particularly troublesome in complex subduction zones like those of south-central Alaska where temperature structure can vary greatly across small distances due to heterogeneity in the subduction geometry.

The approach developed by Eilon and Abers (2017), using differential teleseismic body waves, was designed specifically to improve the resolution of upper mantle attenuation measurements in regions that are not seismically active. This approach was applied to the relatively aseismic Juan de Fuca plate and Mid Ocean Ridge (MOR) to reveal that most attenuation occurs within narrow bands along the ridge axes. We use this method in a broad region in Central Alaska than would be possible with local seismicity alone and measure both S and P phase attenuation.

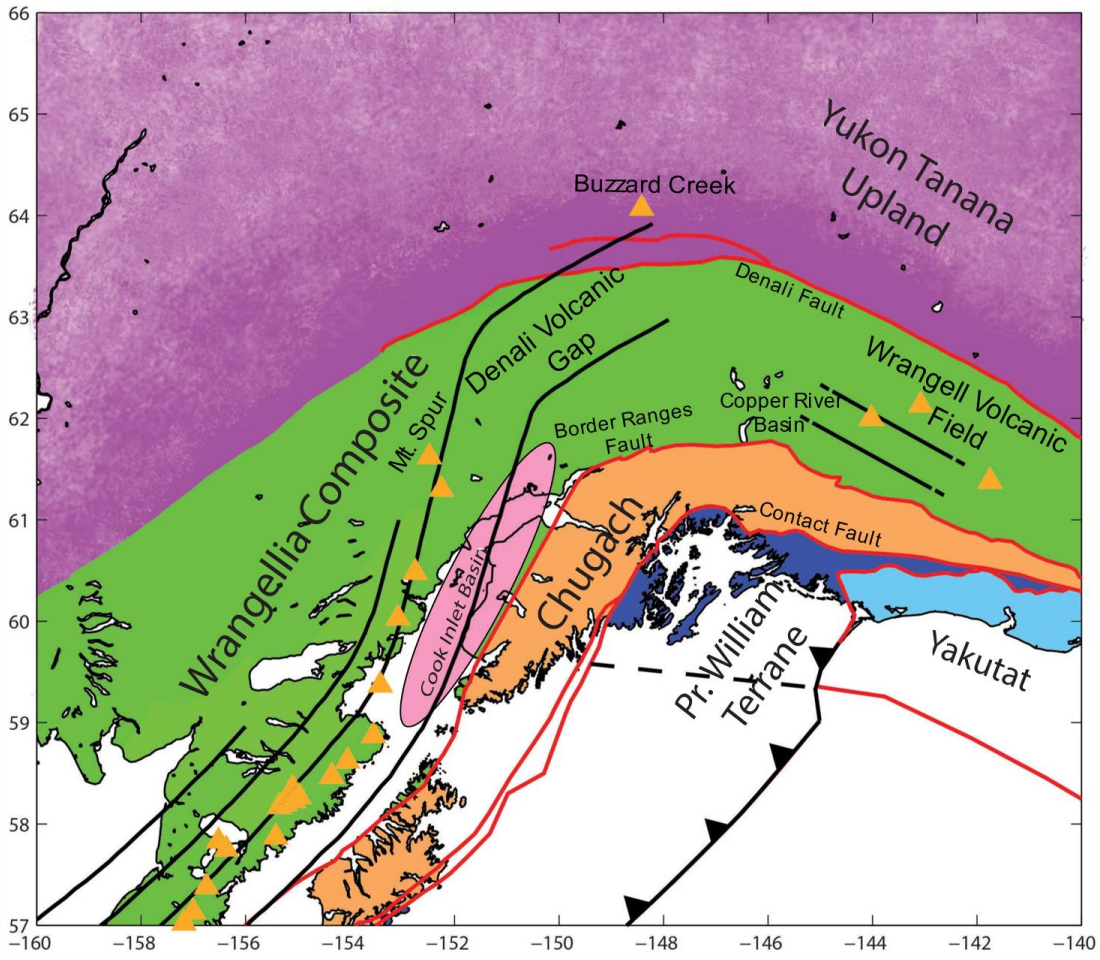

Figure 1.1 - Tectonic regions covered within the study area, adapted from Plafker and Berg 1994. Black solid lines indicated the approximate depth of the subducting slab (50km intervals) from Plafker and Berg (1994) based on WBZ seismicity. Orange triangles indicate volcanoes. Red solid lines indicate the location of known major faults. Black lines with triangles indicate the location of the subduction zone trench and dipping direction as pointing towards the tip of the triangles. Black dashed lines indicate extension of the Yakutat microplate beneath the Pr. William terrane.

CHAPTER 2

Data, Methods and Results

This study uses seismic waveforms collected from arrays across southern Alaska. The waveforms are processed to measure differential travel time delays (ΔT) and body-wave attenuation operators (Δt*) from teleseismic broadband P and S waves at each station. These station-specific observations form the basis for analysis and interpretation.

2.1 Data

Several recent broadband deployments in Alaska provide an unprecedented dataset. We examine data from stations between 55˚ and 65˚ north and 160˚ to 140˚ west collected between 2015 and 2017, spanning the subduction zone and adjacent deforming regions (Figure 2.1). The USArray Transportable Array deployed stations in Alaska during this time period (http://www.usarray.org/researchers/obs/transportable). Those data are supplemented with available Alaska Network and Alaska Volcano Observatory stations to include more dense coverage along the Yakutat terrane and Cook Inlet. In addition, the SALMON (Southern Alaska Lithosphere and Mantle Observation Network) (Tape et al. 2017) and the WVLF (Wrangell Volcanism and Lithospheric Fate) arrays provide increased resolution over areas critical for understanding the extent of subduction in the region (Abers et al., 2019). The WVLF array began in June 2016 and ends in June 2018 in the Central Alaska subduction zone and Wrangell Volcanic Field (WVF) regions; this study only analyzes the first year of recording. The WVLF array is made up of 35 broadband PASSCAL instruments along multiple, linear and dense arrays that can be used to image the subducting crust and upper mantle with high fidelity. The SALMON array is a deployment of 28 broadband, direct-burial posthole seismometers in the Cook Inlet region of the Alaska Subduction zone from summer 2015 to summer 2017 (Tape et

al. 2017). These arrays provide high resolution imaging in a complex region of transition near the Wrangell volcanic field, and along a across the Cook Inlet segment of the Alaska Subduction zone.

The dataset used in this study contains 167 teleseismic (epicentral distances between 30º and 90º) earthquakes with Mw $\geqslant$ 6.0 that occurred between June 4th, 2015 and July 30th, 2017 recorded at up to 207 stations (Figure 2.1, inset). Of these stations, 69 are Alaska Network stations, 11 Alaska Volcano Observatory stations, 65 Transportable Array stations, 35 WVLF stations and 27 SALMON stations.

Multiple core-phase interferences (SKS) are a source of complication for S waves, so we tested a maximum epicentral distance cutoff of 70º for S waves. The cutoff diminished the pool of available events from 167 to 32 and resulted in poor azimuthal coverage for S. We found no systematic changes to results due to this limitation, and thus it was not applied in the final analysis. Instead, events that have visible SKS and S arrival overlap within the spectral calculation window (as described in methods below) on more than half of the recorded traces are manually discarded. After this and other quality control methods described in section 3.3, we are left with 89 events for both S and P phases.

2.2 Methods

2.2.1 Attenuation Measurements

This study calculates attenuation from teleseismic P and S waves using the difference of amplitude and phase of the same event recorded on pairs of stations. The station pairs serve the purpose of isolating the effects of t* on the recorded seismograph specifically to the region of interest. This can be explained by treating the seismogram as a signal modified by several linear

systems. We can characterize the seismogram in the frequency domain as the product of the transfer functions characterizing the source, structure, and instrument:

$$U(\omega) = X(\omega)G(\omega)I(\omega), \quad (7)$$

Where *U(ω)* is the recorded seismogram, *X(ω)* is the source signal, *G(ω)* describes effects of earth structure, and *I(ω)* is the instrument response, at frequency ω (after Chung and Kanamori, 1980). To isolate the structure effects, first the modelled instrument response for each station is deconvolved from the seismogram. Then, by dividing the spectra of the seismogram at one station by the spectra at another station, the source and all structure effects up to the point where the path of the body waves between the two stations diverges are canceled from the spectral ratio. After only the structure effects from the study region remain, the elastic changes in phase can be corrected for by subtracting the predicted phase arrival time for each station, leaving only the anelastic effects on amplitude and phase along the paths beneath each station.

The anelastic effects on amplitude (*A*) and phase lag *(φ)* described in section 2.1 can be expressed in the form $Ae^{-i\omega\varphi}$ and can be separated in the frequency domain in terms of *t** and frequency as formulated by Eilon and Abers (2017) with the following equations:

$$\mathrm{A}(f) = Ce^{(-\pi f t^*)}, \quad (8)$$

$$\varphi(f) = \frac{1}{\pi}\, t^* \ln\left(\frac{f_\infty}{f}\right) = t^*\left[\frac{\ln(f_\infty)}{\pi} - \frac{\ln(f)}{\pi}\right], \quad (9)$$

In this equation, C is a constant describing frequency-independent amplitude effects including geometric spreading and f_∞ is some large reference frequency. The phase term refers to the difference between the ray-theoretical phase and the phase incorporating attenuation effects.

Using equations (8) and (9), we can calculate a differential *t** value between station pairs from the pair-wise amplitude ratios and phase differentials of the spectra recorded at each station pair in an array, to remove source effects and parts of earth structure far from the array. The amplitude ratios and phase differential can be derived from the above relationships (Eilon 2016):

$$\ln(R_{ij}) = k_1 - \pi f \Delta t^*_{ij}, \tag{10}$$

$$\Delta\varphi_{ij} = k_2 + \frac{1}{\pi}\ln\left(\frac{f}{f_0}\right)\Delta t^*_{ij}, \tag{11}$$

Where R_{ij} is the spectral amplitude ratio between stations i and j at frequency *f*, $\Delta\varphi_{ij}$ is the phase shift, *f* is the center frequency of each filter, k_1 is a constant relating to the difference of frequency-independent amplification between each station, k_2 represents any constant-phase shifts, and Δt^* is the differential path averaged attenuation operator (Eilon and Abers, 2017). Each pairwise measurement of amplitude ratio R_{ij} and differential phase $\Delta\varphi_{ij}$ as a function of frequency *f* provides a constraint on the corresponding differential attenuation operator Δt^*_{ij}.

To account for frequency dependence requires a change in the relationships between observables (R_{ij} and $\Delta\varphi_{ij}$) t* (e.g., Minster and Anderson, 1981; Eilon and Abers 2017):

$$\ln(R_{ij}) = k_1 - \pi f_0^{\alpha} f^{1-\alpha} \Delta t^*_0, \tag{12}$$

$$\Delta\varphi_{ij} = k_2 + \frac{1}{2}\cot\left(\frac{\alpha\pi}{2}\right) f_0^{\alpha} f^{-\alpha} \Delta t^*_0, \tag{13}$$

Henceforth, this study presents both results that assume no frequency dependence (α = 0) and a weak frequency dependence (α = 0.27). The latter is consistent with experimental and previous

observational studies (e.g., Faul and Jackson, 2005; Rychert et al., 2008; Stachnik et al., 2004) and is treated as the preferred model for this study, while the former is used to compare with previous attenuation results that also assume no frequency dependence (Roth et al. 1999; Eberhart-Phillips et al. 2008; Liu et al. 2014).

2.2.2 Data Pre-Processing

Three-component seismic waveforms are down-sampled to 10 samples-per-second to achieve a parity in the sampling rate for data from different arrays. Horizontal channels are rotated to transverse polarization to isolate the SH phase and to remove radially-polarized SKS from time windows around SH records. The instrument response is removed from both vertical (Z) and transverse (T) traces for further analysis for P and SH waves respectively. Waveforms are windowed 40s before and after the predicted arrival for each phase (SH and P) and then extended 20% on each side with an additional 1 second of padding prior to applying a 20% Tukey window (Harris, 1978).

2.2.3 Processing

After pre-processing, we analyze the T component waveforms for SH and the Z component waveforms for P. To calculate the differential travel time delays (ΔT), the waveforms are cross-correlated after a bandpass filter of 0.083 – 1 Hz and from 0.2 – 1 Hz for the S and P waveforms respectively, applied to a handpicked window of 10 – 20 s around the first arrival. We discard all waveform pairs with mean cross-correlation coefficients of less than 0.65. The remaining traces are adjusted using the calculated lags to determine relative timing (VanDecar and Crosson, 1990). The phase onset time for the stacked traces is manually picked and added to the offset relative phase arrival from the cross-correlation lags to generate an absolute arrival time. This absolute arrival time is used as the time reference in the Δt^* (differential t^*)

calculation, which considers phase as well as amplitude. Station-averaged delays are calculated over all earthquakes or over select back azimuthal ranges, after removing outliers with lags more than 3 standard deviations from the mean.

Signals for each station pair are used to calculate amplitude ratios and phase differences at a range of narrow frequency bands, through a multiple-narrowband-filter technique (Dziewonski et al. 1969). The frequency-dependent amplitudes are calculated from waveforms by selecting a 35s window around the first arrival, starting 5s before it. Subsequently, a comb of 30 narrow-band filters, equally spaced in center frequency from 0.05 – 1 Hz and equal in width, is applied to the windowed waveform. At each frequency where the signal exceeds noise, the phase shift and amplitude ratio for each station pair is computed from these narrow-band-filtered waveforms (e.g., Figure 2.2). As a means of quality control, we discard any station pair for which fewer than four frequencies have signal that exceeds 10 times the pre-event noise, and any trace for which the cross-correlation coefficient with the stacked trace is less than 0.5. The expected effect of attenuation on the phase and amplitude spectra in the frequency domain is described in Section 2.

The station-pair Δt^* values are calculated using the system of equations defined by equations 10 and 11 or 12 and 13, which can be solved by a least squares method at each narrow-band frequency for Δt^*. These pairwise Δt^* values for the comb-of-filters method are then determined with a one-step constrained least squared fitting to derive event-specific individual-station Δt^* values, in a manner similar to that used for differential travel times (VanDecar and Crosson, 1990). To make stable comparisons of S to P phase data on both Δt^* and ΔT, we discard all results where we do not have Δt^* and ΔT data for both S and P phases, for each

station-event pair. In total, this study calculates 4300 measurements for both S & P phase Δt* and ΔT data, from 89 earthquakes.

2.2.4 Spectral Ratio and Comb of Filter Comparison

In parallel, we also calculate Δt* values through a direct Fourier-domain amplitude spectral ratio calculation (similar to Roth et al. 1999) as an independent method to verify Δt^*results. In this method, we calculate the Thompson multitaper Fourier amplitude spectrum (Thomson, 1982) for the pre-processed and travel-time delay-adjusted waveforms for a pair of stations. These amplitude spectra are then divided in the Fourier domain to calculate spectral ratios for the pair of stations within a frequency band from 0.05 Hz to 0.5 Hz. This approach works as outlined in previous sections, by deconvolving the source and structure effects from out study region out of the signal. Using equation 10, we can calculate Δt* values for this pair of stations using the best-fit line's slope divided by -π.

The Fourier-domain method has been found to be less stable than the comb-of-filters method, which gives usable results over a wider frequency band (Eilon and Abers, 2017). One advantage of the filter comb method is that it fits both the spectral amplitude and phase residuals of the station waveforms (Figure 2.2), whereas the spectral ratio method does not account for phase information; the filter comb method also appears to be more robust with respect to Fourier-domain noise (Eilon, 2016). To compare the methods' results, the standard deviations of each station per event are calculated from the pairwise Δt* values. These standard deviations are plotted as a histogram for both S and P phase results (Figure 2.3). Calculating the median standard deviation for each method from the values within the histograms shows a median standard deviation that is 0.13 s smaller in the P phase for the comb of filter methods than for the spectral ratios method. This difference could be attributed to the stability of results over a wider

frequency band as mentioned above. In contrast, the comparison of medians for the S phase shows the spectral ratios median is 0.08 s smaller. In both cases, these results could be influenced by the local variability of attenuation around any given station wherein a higher standard deviation could also be more appropriate to the actual structure.

2.3 Results

2.3.1 Overview

The study region can be effectively segmented into six zones based on regional geology and the Alaska-Aleutian Wadati-Benioff seismicity (Figure 2.4). **Region 1** is the Aleutian arc-backarc region, which is bounded in the east by the edge of the Alaskan-Aleutian Wadati-Benioff seismicity (green dividing line in Figure 2.4) and by the Forearc region to the south. **Region 2** is the Cook Inlet Basin bounded by the Border Range Fault in the south. In this region, thick basin sediments should have strong effects on signals (Smith and Tape, 2019). **Region 3** is the Aleutian Forearc in the Kenai-Chugach Range area, bounded by the eastern edge of the Alaska-Aleutian Wadati-Benioff zone (WBZ) seismicity in the east and by the 75 km slab depth contour to the north and west, excluding the Cook Inlet Basin region. Both region 1 and 3 comprise a region of normal Pacific/Yakutat plate subduction in the southwest, typically referred to as the Aleutian subduction region, and a region of largely amagmatic subduction of both the Pacific and Yakutat plates referred to as the Denali segment (Eberhart-Phillips et al., 2006; Kim et al. 2014). The remainder of the study area located west of the Alaskan-Aleutian WBZ seismicity can be broken up into three regions. The area north of the Denali fault and east of Aleutian WBZ is referred to as **Region 4,** the Continental Interior region. The region south of the Denali fault and north of the Contact Fault zone, extending to the edge of Wadati-Benioff seismicity is **Region 5,** the Wrangell region. Finally, the southern area within and directly

surrounding the Yakutat terrane, south of the Contact Fault, is **Region 6** the Yakutat region. The following is a summary of the ΔT and Δt* results shown in Table 2.1 by region, reporting the median values and the 2-sigma standard deviation of the mean of the station-average results for each region.

The results (Figure 2.5) are shown in maps with station-average (arithmetic mean) values for each station. To calculate these station-average values, the sample standard deviation of the individual ΔT and Δt* measurements for each event at a given station are calculated, results lying outside of 3 standard deviations from the mean are removed, and then the mean is recalculated from the remaining data. The mean, median and standard deviations of the mean for the individual measurements are evaluated across each region (Table 2.1) discussed below. The results indicate strong correlations between measurements and regional variations.

The slowest arrivals (most positive ΔT) occur at stations in Region 6, the Yakutat terrane region. The next slowest arrivals are found in Region 5, the Wrangell Volcanic Field (WVF) with and in Region 1, the Cook Inlet Basin (Figure 2.5). The fastest paths occur Region 3, the Aleutian Forearc and Region 1, the Aleutian arc-backarc regions. In addition, individual measurements (Figure 2.6) reveal strong back-azimuthal variations at some stations. Station averages split by back-azimuth (BA) highlight those variations, separating events originating west of the array (as defined by BA > 180°, generally from northwest Pacific subduction zones) from events to the east (as defined by 180° > BA > 0°; generally events from Central and South America) (Figure 2.7, Table 2.2, 2.3).

The highest attenuation regions are Region 1, the Alaska-Aleutian back-arc and Region 4, the continental interior region (Figure 2.6, 2.5). In contrast to the ΔT measurements, the lowest

attenuation area is Region 2, the Cook Inlet Basin. Like ΔT, the Δt* results have also been grouped into east and west event groups to study the azimuthally dependent variability of the data (Figure 2.7, Table 2.2, 2.3).

2.3.2 Regions 1 & 3 - Alaska-Aleutian Subduction

The Alaska-Aleutian subduction region is the most well-understood region of our study area (Page et al. 1989; Ratchkovski and Hansen 2002; Stachnik et al. 2004; Martin-Short 2016) and with relatively well-understood geometry of subduction of the Pacific and Yakutat plates (Eberhart-Phillips et al. 2006). This makes the Alaska-Aleutian subduction region an important basis for comparison with the other more complex areas in our study like the WVF.

The simplicity of the region is reflected in the ΔT results, which align with the expected temperature gradient across the subduction zone. The arc and backarc region (Figure 2.5, Region 1; Table 2.1) shows ΔT_S & ΔT_P arrival values of -0.44 s ± 0.02 and -0.14 s ± 0.01 with faster arrivals closer to the subduction zone than further inland. Meanwhile, the colder forearc region (Figure 2.5, Region 3) shows arrivals with ΔT_S & ΔT_P of -1.13 s ± 0.06 and -0.37 s ± 0.02 that are significantly (2-sigma, Table 2.1) faster than the arc and backarc region results. The azimuthally separated data (Figure 2.7) show a clearer, slow mantle wedge for the west-originating results. The east-originating results on the other hand, show faster arrivals in the arc to backarc (Region 1) than in the forearc (Region 3).

By contrast the Δt* results (Figure 2.5) clearly distinguish between the arc to backarc and the forearc region. The arc to backarc region reports high attenuation with Δt_S^* & Δt_P^* results of 0.21 s ± 0.01 and 0.07 s ± 0.005 and the forearc region reports low attenuation with Δt_S^* & Δt_P^* results of -0.14 s ± 0.02 and -0.01 s ± 0.01. In addition, these results show large variation across

the subduction zone with the Δt* variation between the highest attenuation results in the arc-backarc and the lowest attenuation results in the forearc is 2.5 s. The azimuthally separated data (Figure 2.7) once again confirm this pattern.

We can compare with previous studies of attenuation (local earthquake Q measurements) performed along different transects of this subduction zone (Stachnik et al. 2004). In the Cook Inlet beneath the SALMON array (Figure 2.8), it is clear that stations located above slab depths of 80 km or greater (Region 1), not only show higher attenuation (especially for the S phase) in comparison to the forearc but also show a slowing of arrivals and an increase in attenuation towards deeper slab depths. It is also clear that fast arrivals and low attenuation are uniform throughout the forearc region (Region 3).

2.3.3 Region 4 - The Continental Interior

The Continental Interior region (Figure 2.5, Region 4) is north of the Denali Fault. The ΔT_S & ΔT_P results of 0.11s ± 0.09 and -0.14s ± 0.03 reflect a mix of fast arrivals near the Alaskan Range and a gradient from west to east of slowing arrivals along the Denali Fault. The zone of fast arrivals corresponds closely to subducting material extending past the Wadati-Benioff zone seen in recent seismic velocity analyses (Wang and Tape, 2014; Martin-Short et al., 2018). This fast arrival zone stands in contrast to the uniformly high attenuation results of Δt_S^* & Δt_P^* of 0.40s ± 0.03 and 0.19 s ± 0.01 throughout the continental interior region. The region reports the highest median Δt* values in the region.

Azimuth impacts the distribution of slow and fast arrivals across the Continental Interior region (4). Arrival results for west originating events with ΔT_S & ΔT_P of -0.02s ± 0.11 and -0.12s ± 0.04 while results for east originating events with ΔT_S & ΔT_P results of 0.17s ± 0.03 and 0.03s

$\pm$ 0.03 mark a decrease of fast arrivals towards the west. By contrast, the azimuthal variation of the Δt^* results are minimal in this region (Figure 2.7).

2.3.4 Region 5 - The Wrangell Volcanic Field

The Wrangell region (Figure 2.5, Region 5) shows a relatively simple pattern of arrival times with a group of faster than average arrivals to the northwest of the Wrangell Volcanic Field (WVF), and a group of slower than average arrivals elsewhere. The region overall is dominated by slow arrivals with ΔT_S , ΔT_P of 0.71 s $\pm$ 0.03 s and 0.19 s $\pm$ 0.01 s. The transition between the fast and slow regions occurs over a relatively short distance across the Border Ranges Fault south of the WVF (approximately a 1 s difference in P and a 0.5 s difference in S over 30 km). In both S and P, arrivals become slower near the thick Yakutat sediments. The pattern differs from that of the Alaska-Aleutian subduction system, with little obvious evidence for the Wrangell slab.

The station averaged Δt^* results of the Wrangell region (Figure 2.5, Region 5) are more complex, with clear coherence between nearby stations, but low-attenuation regions and high-attenuation regions separated by as little as 30 kilometers. The sharp boundaries reflect a strong signal and suggest a potentially shallow source for the attenuation anomaly in the region. In both S and P, the region shows high attenuation (negative Δt^*) in the north and south, and lower attenuation in the middle of the region. The northern region of higher than average attenuation stretches from the Denali Fault to the northern edge of the Wrangell Volcanic field. The low attenuation region stretches from the east edge of the Alaska-Aleutian Wadati-Benioff seismicity to the western edge of the Wrangell Volcanic Field and may be associated with Wrangell volcanism although only two stations were located directly on the volcanoes. The southern low-attenuation region lies south of the Border Ranges Fault. The patterns show little azimuthal

variation, though the sparsity of viable station data (at least 5 Δt* measurements per station) makes interpreting a pattern more difficult.

To best analyze the complex nature of the Wrangell region and compare to the simpler Alaskan-Aleutian subduction, we look at a north-south cross section across the WVLF array stations and a cross section of local seismicity (Figure 2.9). The cross section and Δt* results show three main attenuation sub-regions. Assuming attenuation at a station is accumulated entirely between the subducting slab and the station, we can compare the results at a station to the depth of the subducting slab beneath it. A high-attenuation region in S dominates the Wrangell slab region where the slab is approximately 25km to 40km deep, and a low attenuation region from 40km to 110km depth. The stations farther north are once again highly attenuating. Compared to the Alaska-Aleutian subduction region (Regions 1,3), the WVF results show the transition from low to high Δt_S^* at stations overlying deeper slab depths (100 km) than the Alaska-Aleutian results (80 km). In addition, there is a region of high Δt* located 70-120km south of the WVF that does not have a parallel in the Alaska-Aleutian subduction region.

2.3.5 Regions 6 & 2 - The Yakutat Terrane and the Cook Inlet Basin

The Yakutat Terrane, Region 6, is overlaid by the Yakutat basin, a collection of various marine sedimentary strata of approximately 10km in thickness (Trop and Ridgway 2007). These sediments are made up of predominantly sandstone, mudstone, and siltstone so slow arrivals in this region are to be expected, as observed this region (6) contains the slowest arrivals within the study area with ΔT_S & ΔT_P of 1.76 s ± 0.04 and 0.63 s ± 0.02. These results also show little dependence on azimuthal variations.

The Yakutat region Δt* (Figure 2.5, Region 6) results show a much more complex pattern than ΔT with Δt_S^* & Δt_P^* of 0.05 s ± 0.03 and 0.009s ± 0.013 and numerous stations reporting either more or less attenuation than average over short (~30km) distances. The large azimuthal variability shown in this region (Figure 2.6) also makes distinguishing a pattern more difficult.

The Cook Inlet Basin, Region 2, contains the thickest sedimentary structures in our study region, with a sedimentary cover sequence reaching depths approximately 8 km at its deepest parts in the west of the basin (Plafker and Berg, 1994; Shellenbaum et al. 2010; Smith & Tape 2019). Within the Cook Inlet basin (Figure 2.5, Region 2) arrivals are relatively slowed with the slowest arrivals located at the center of the basin. Relative to the median arrivals in the surrounding regions (1 & 3) ΔT is larger by 1.25 s ± 0.08 and 0.44 s ± 0.03 for ΔT_S & ΔT_P within the Cook Inlet. These results also show minimal azimuthal dependence (Figure 2.6, 2.7). East originating events do indicate some widening of the slow arrival zone within the Cook Inlet, but sparsity of viable data makes the pattern inconclusive.

The Δt* results for the Cook Inlet are more uniform but show the lowest attenuation of any region within our study area with Δt_S^*, & Δt_P^*, of -0.61 s ± 0.04 and -0.33 s ± 0.01. There is a slight azimuthal dependence of the Δt* with west back-azimuths having higher than average attenuation on the west end of the Cook Inlet. In both the Yakutat (Region 6) and Cook Inlet (Region 2) regions we see that the attenuation measurements are not obviously affected by the sediments as they do not show high attenuation signal at these frequencies (0.05 - 0.5 Hz).

2.3.6 Azimuthal Variations in the Data

This study groups ΔT and Δt* by azimuthal origin (Figure 2.7) of the earthquake events relative to stations. This distinguishes areas with variation in deep structure resulting in large azimuthal variations and areas with uniform deep structure or strong shallow signals like sedimentary basins resulting in minimal azimuthal variations. In Region (1) the Aleutian volcanic arc shows significant changes between west azimuths where both ΔT and Δt* are high compared to the east where both are low. In the Aleutian Forearc region (3) rays that travel from the east report lowered ΔT and Δt* region for west vs. east back azimuth events. By contrast, the Cook Inlet region (2) reports significantly less azimuthal variation for both ΔT and Δt* results.

The Continental Interior Region (4) shows little Δt* variation with azimuth but large ΔT variation, with slower arrivals for east originating events than west events. The extension of fast arrivals beyond the east edge of the WBZ reported in recent seismic velocity studies of the region (Wang and Tape 2014; Jiang et al. 2018) is clearly visible for west back-azimuths and reduced in eastward extent for east back-azimuths. Conversely the Yakutat region (6) shows little variation in ΔT but shows some variation in Δt*. While the specific structures that produce these variations are difficult to identify, looking at the azimuthal variation shown in Figure 2.6 it is mostly east to southeast back-azimuth rays that sample high attenuating structures. These results showcase the potential of Δt* results to discern upper mantle structure that is obscured in ΔT results due to shallow surface effects.

2.3.7 Frequency Dependence and Quality Control

This study also produced Δt* results assuming no frequency dependence for the purpose of comparison to previous attenuation studies of this and other regions that had the same

frequency dependence assumption (Figure 2.10). The results are compiled in Table A.2 and are broadly the same as those assuming a frequency dependence alpha of 0.27.

Alongside these results, we also employed several quality-control measures to determine which measurements show significant results. The first of these was to measure the standard error for Δt* S at each station, based on the standard deviations of each station per event. The mean standard deviation for every station is then calculated from the per event values after excluding outliers by trimming standard deviation values greater than 3 standard deviations from the mean standard deviation for that station. The trimmed mean standard deviation is then used to calculate the standard error per station (Figure 2.10). The standard error plot shows high standard error located in the Cook Inlet Basin, the Yakutat terrane, and the Copper River Valley, all locations with sizeable sedimentary structures that report generally slow travel time arrivals.

Using this standard deviation, a trimmed version of the Δt_S^* with no frequency dependence is shown where stations with standard error greater than 0.25, about 10% of the stations, are removed. The results of this (Figure 2.10) are broadly the same, with most of the stations trimmed located around the Cook Inlet Basin (Region 2) the Yakutat terrane (Region 6) where standard error values are the highest.

A final plot is shown where only stations whose signal (absolute value of Δt_S^*) is greater than twice their corresponding standard error. This process leaves only the stations overlying the strongest anomalies and from this we can still see all the major structures previously discussed. In the case of the Yakutat terrane (Region 6), this process leaves only a handful of stations that show a clearer pattern where low attenuation is structures are significant in the west and high attenuation structures in the east.

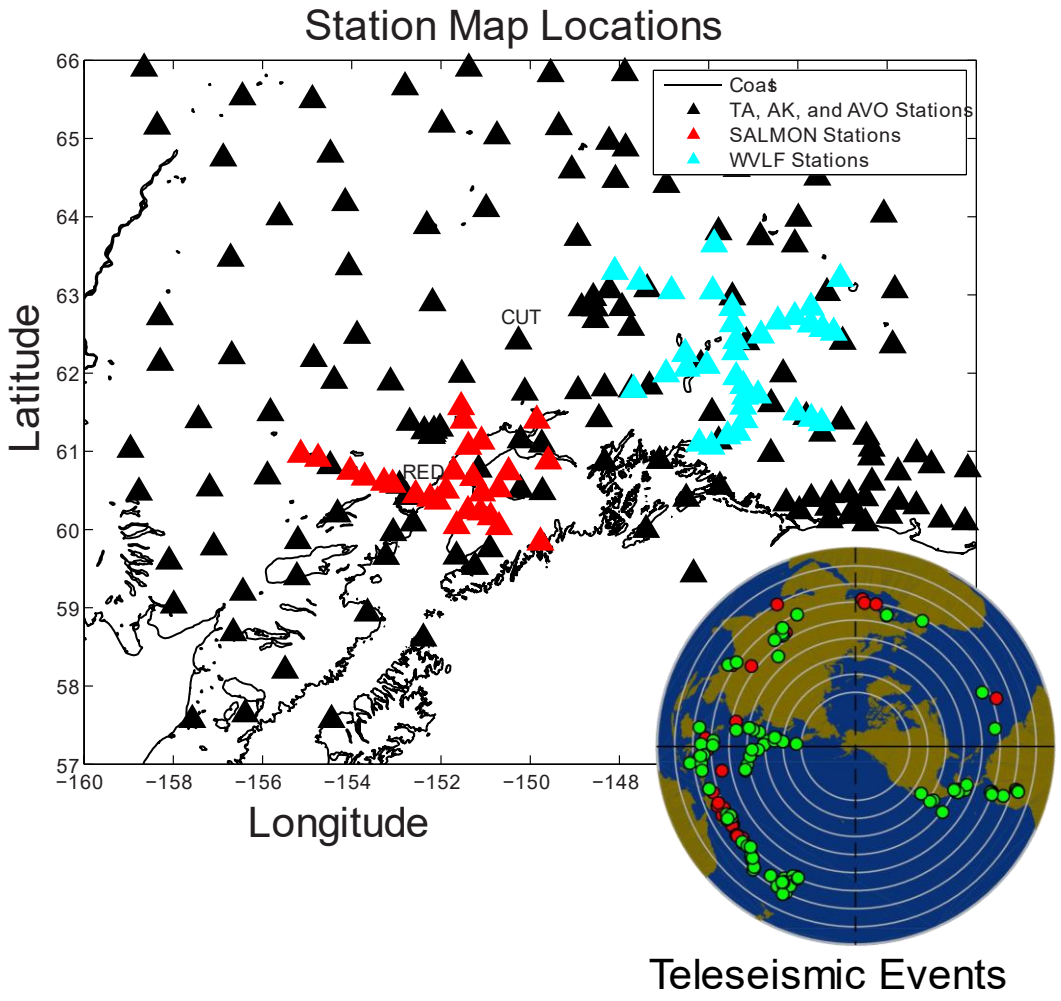

Figure 2.1 - Maps of station locations and teleseismic event data locations. Black triangles indicate stations from the Transportable Array (TA), Alaska Regional Network (AK), and Alaska Volcano Observatory (AVO) arrays. Red triangles indicate stations within the SALMON array and blue triangles indicate stations within the WVLF array. Stations RED and CUT used in Figure 2.2 are labeled on this map above the corresponding location. On inset map on bottom-right corner, colored circles indicate foci of teleseismic events. Green circles correspond to events used in S&P phase events and red circles correspond to events excluded for interference with S phase signal.

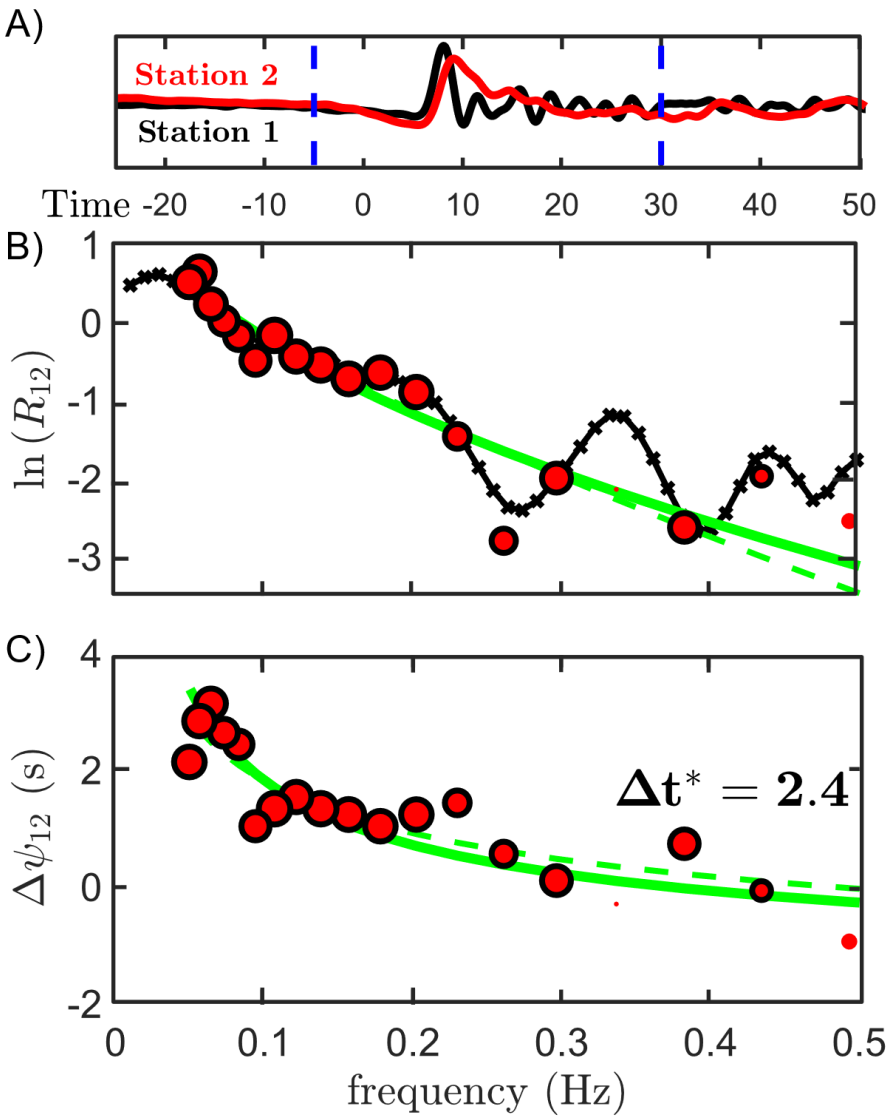

Figure 2.2 - Filtered data centered around the predicted S arrival at station 1 CUT (Chulitna, Alaska) and at station 2 RED (Mount Redoubt, Alaska). Blue lines indicate windows for spectra calculation. Red circles are the logarithm of amplitude ratios / phase differentials at each narrow band filter (as in the comb of filter methods described in Section 2.2.3) with green lines indicating best fit slopes. The solid green line represents the best fit assuming no frequency dependence of attenuation, and the dashed green line represents the best fit assuming the experimentally derived frequency dependence of 0.27 (Jackson and Faul 2010). Size reflects robustness of measurement of each narrow band. Black hatched line is the spectral ratio calculated by division of FFT (Fast Fourier Transform) amplitude spectra.

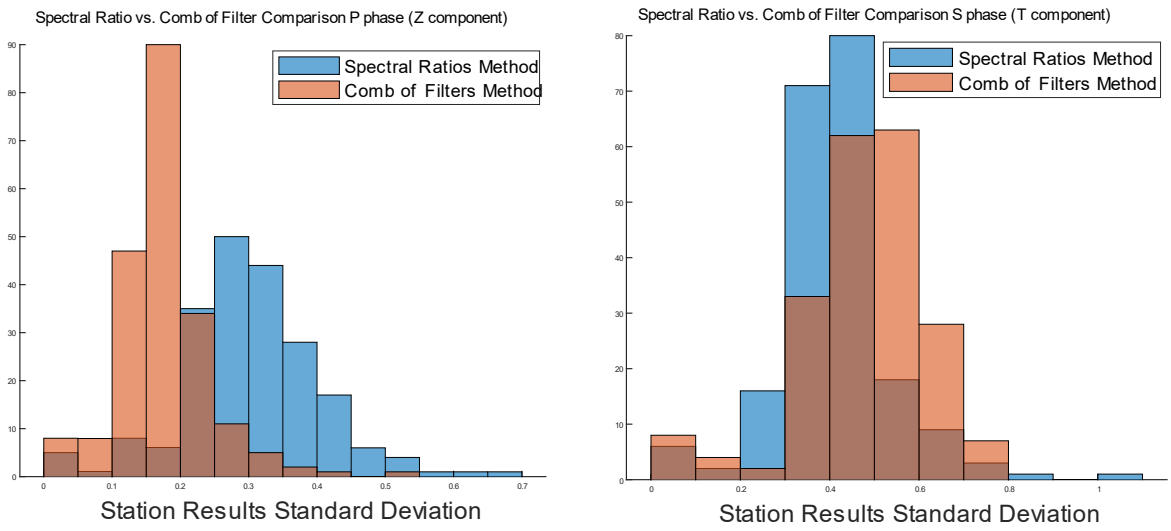

Figure 2.3 - Histograms of the standard deviations of all t* measurements made by both the method of spectral ratio calculation (similar to Roth et al. 1999) and the comb of filters method (Eilon and Abers 2017). The left side shows the histograms of the P phase measurements, and the right side shows the histograms of the S phase measurements. The blue bins correspond to the spectral ratios method and the orange bins correspond to the comb of filters method.

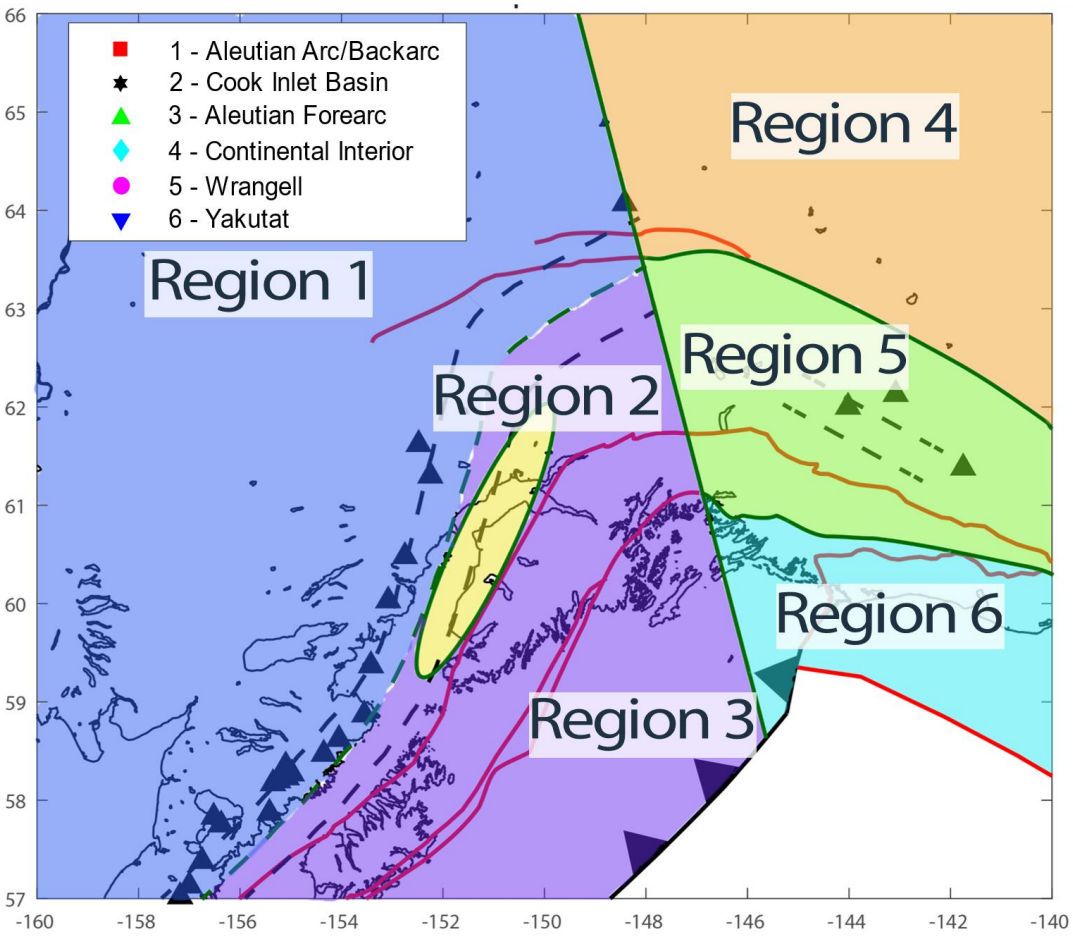

Figure 2.4 - Regionalization of the study area. Dashed lines indicate the depth of the subducting slab as indicated by WBZ seismicity in 25 km intervals. Black triangles indicate the location of volcanoes. Red lines indicate the location of large regional faults. Green dividing line indicates the west edge of the Alaska-Aleutian Wadati-Benioff seismicity. Region 1 is the Alaskan-Aleutian subduction arc and backarc region. Region 2 marks the approximate location of the Cook Inlet Basin. Region 3 marks the region of the Alaskan-Aleutian subduction forearc. Both Regions 2 and 3 are separated on the east from Regions 4-6 by the edge of the WBZ seismicity. Region 4 is the Continental Interior, bounded to the south by the Denali Fault. Region 5 is the Wrangell region, marking the Wrangell Volcanic Field and the surrounding areas. Finally, Region 6 is the Yakutat region, comprising the Yakutat terrane and proximal regions.

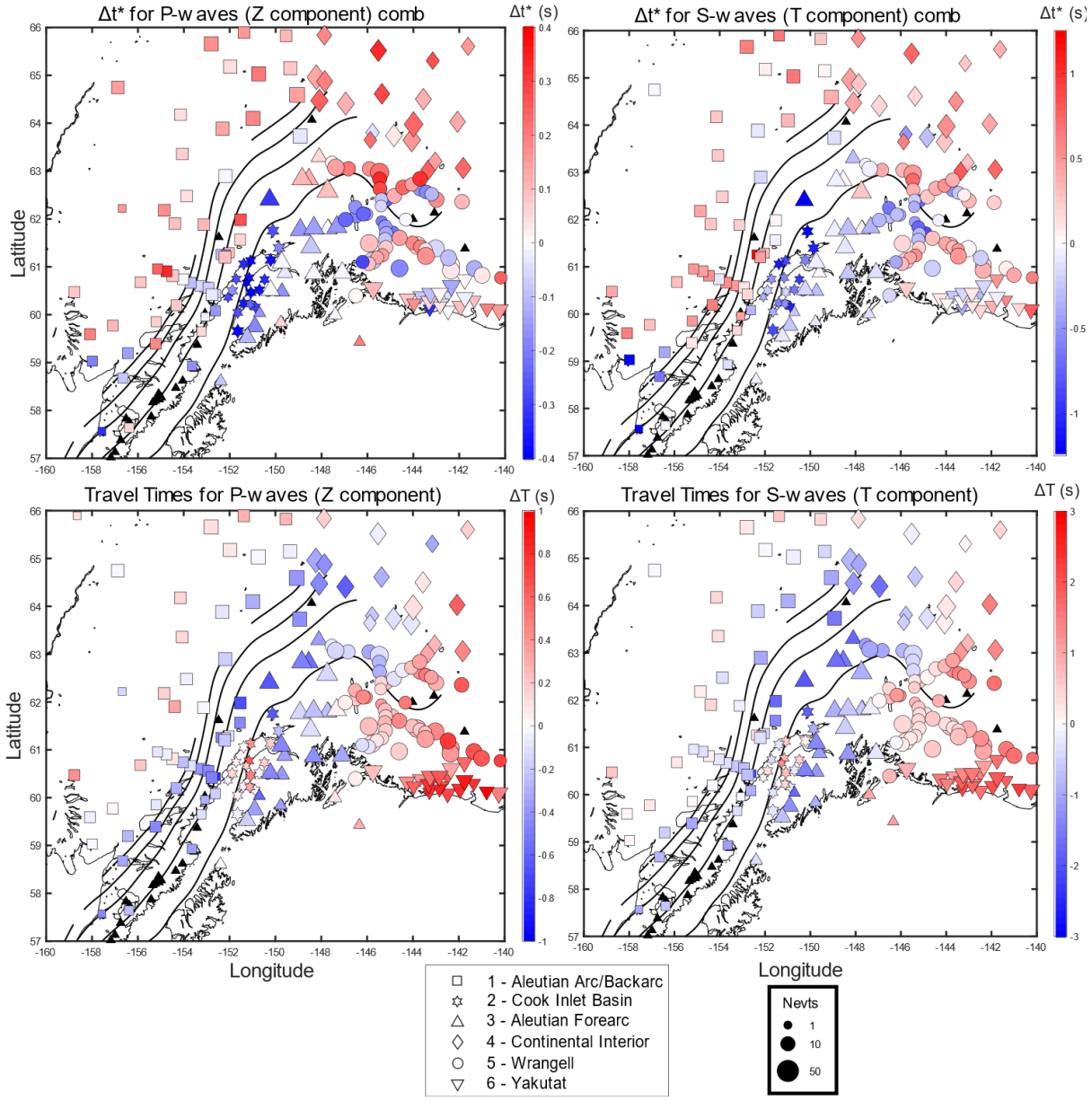

Figure 2.5 - Station averaged ΔT and Δt* results plotted as circles with size indicating number of observations at each station. Red color indicates high attenuation or high travel time delays, and blue indicates low attenuation or low travel time delays. Black lines indicate depth of subducting slab as indicated by WBZ seismicity at 40 km intervals (Hayes et al. 2018). Red lines indicate major fault locations. Black triangles refer the location of volcanoes. Station shapes correspond to the regionalization set forth in Figure 2.4 with color fill corresponding to ΔT and Δt* results. Size is corresponding to the number of observations taken at each station, with stations having less than 5 observations not reported.

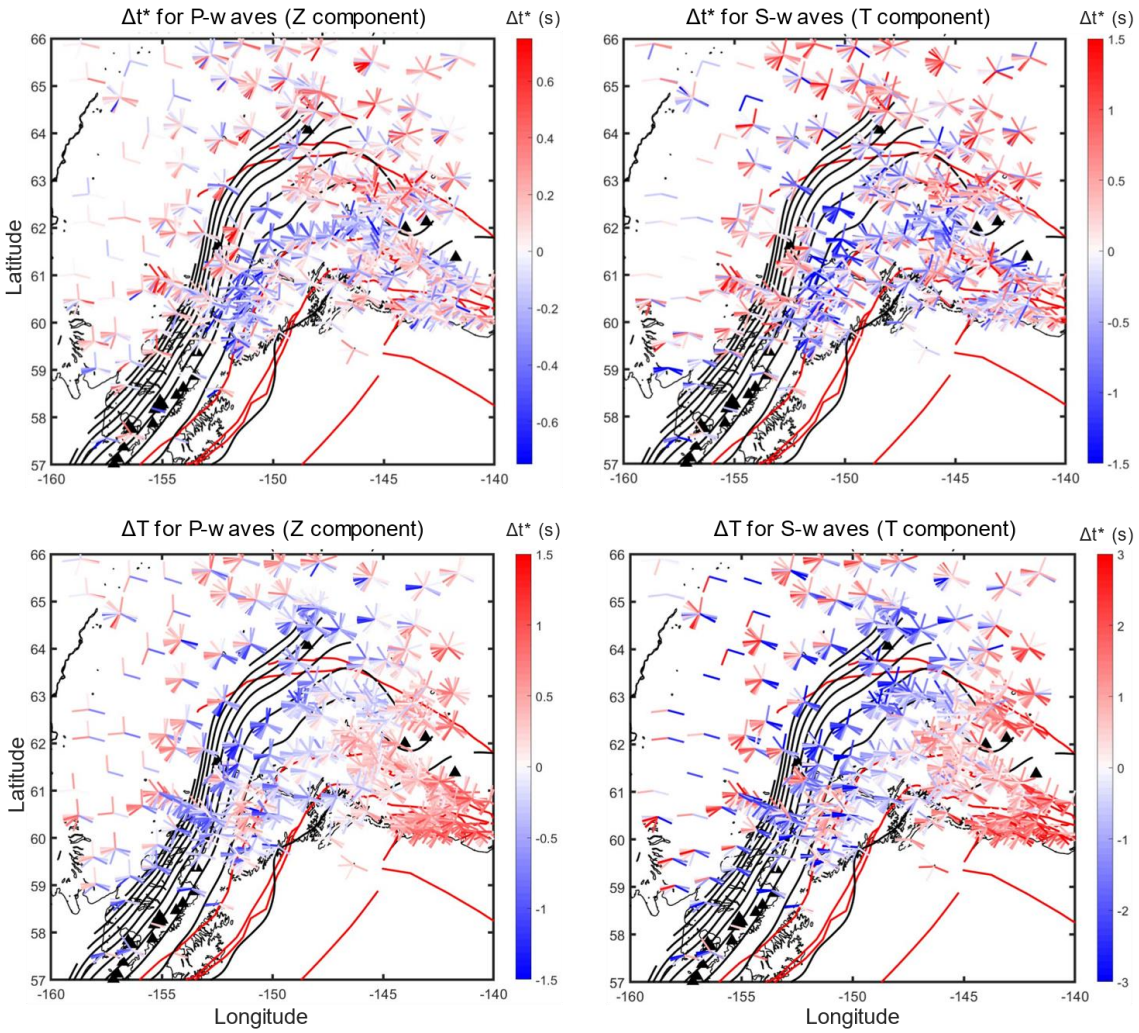

Figure 2.6 - Maps of differential attenuation and differential travel time, Δt* and ΔT, for each event, recorded at Transportable Array, Alaska Network, Alaska Volcano Observatory, WVLF and SALMON stations with spokes indicating back azimuth direction of corresponding event. Red (positive) Δt* values indicate relatively high attenuating rays and Blue (negative) Δt* values indicate relatively low attenuating rays. A) & B) are maps of P & S body wave measurements of Δt* along the vertical & transverse components respectively. C) & D) Similar to above but are measurements of ΔT along the vertical & transverse components respectively. Black lines indicate depth of subducting slab as indicated by WBZ seismicity at 20 km spacing. Red lines indicate major fault locations. Black triangles represent volcanoes.

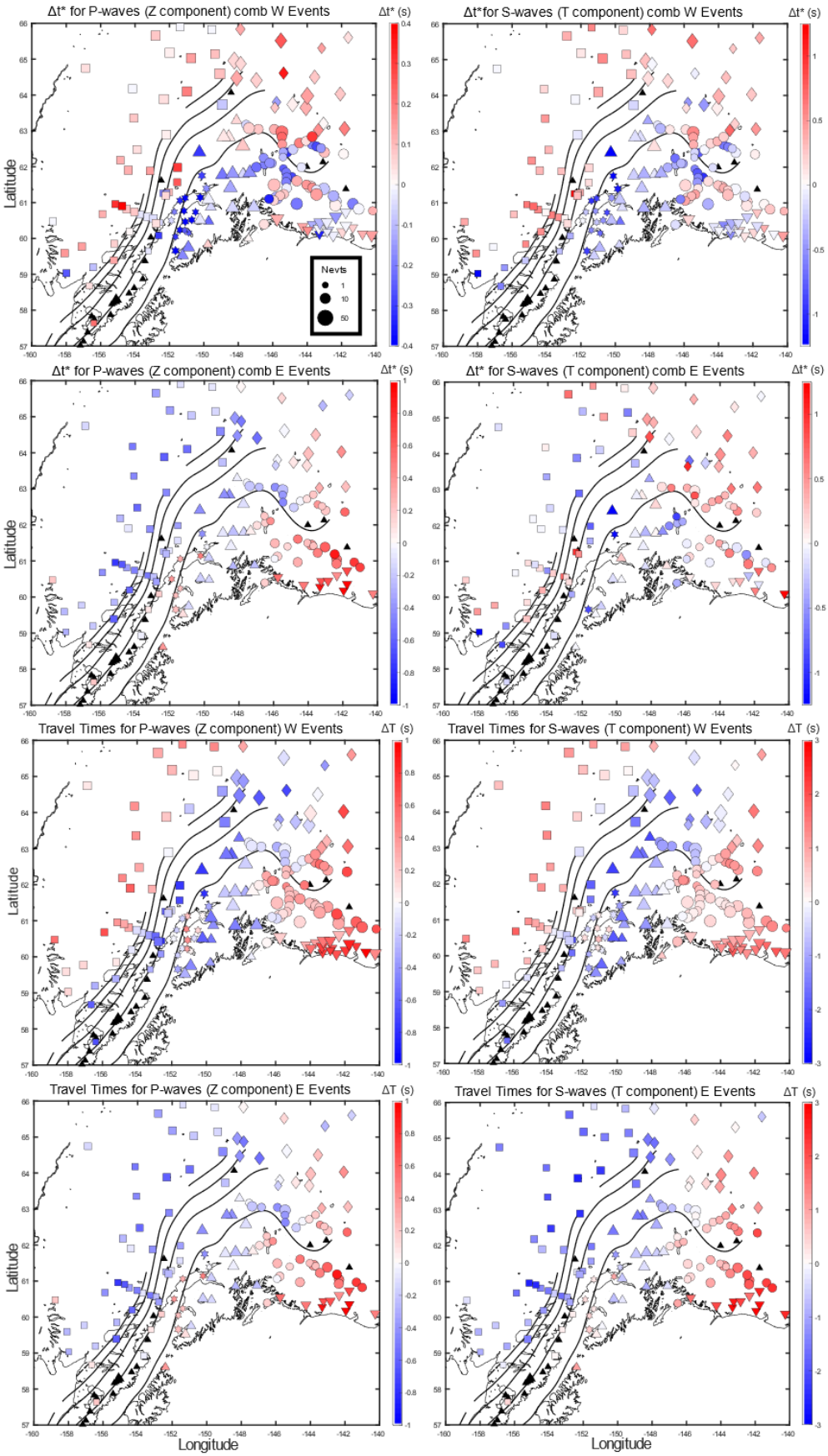
Δt* for P-waves (Z component) comb W Events
Δt* (s)
Δt*for S-waves (T component) comb W Events
Δt* (s)
Nevts
1
10
50
Δt* for P-waves (Z component) comb E Events
Δt* (s)
Δt* for S-waves (T component) comb E Events
Δt* (s)
Travel Times for P-waves (Z component) W Events
ΔT (s)
Travel Times for S-waves (T component) W Events
ΔT (s)
Travel Times for P-waves (Z component) E Events
ΔT (s)
Travel Times for S-waves (T component) E Events
ΔT (s)
Latitude
Longitude

Figure 2.7- Station averaged ΔT & Δt* results. Size, fill, and shape rules consistent with Figure 2.4. Black lines indicate depth of subducting slab as indicated by WBZ seismicity at 40 km intervals. Red lines indicate major fault locations. Black triangles refer the location of volcanoes. Results labeled East and West are station averages including only events originating in the west (180° to 360°) and east (0° to 180°) of the center of the study region respectively. Top row shows Δt* results for west events. Upper middle row shows Δt* results for east events. Lower middle row shows ΔT results for west events. Bottom row shows ΔT results for east events.

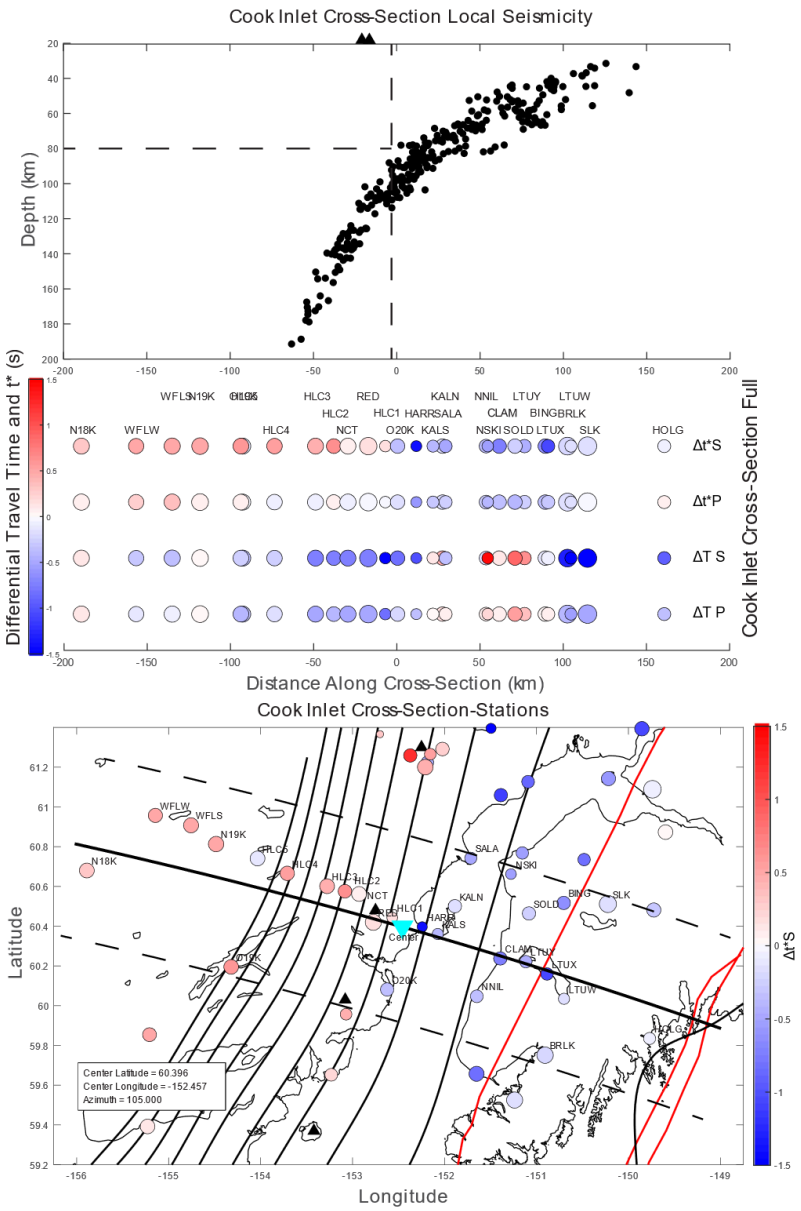

Figure 2.8 - Cross-section across the Cook Inlet indicates the forearc/backarc transition along the Alaskan-Aleutian subduction zone. Top panel plots local seismicity up to 25km away. Dashed lines in the top panel mark the depth and distance of low to high attenuation transition. Local seismicity was obtained from the USGS seismic database from June 2016 to June 2018 with events of depth errors > 1km and rms values > 0.75. Middle panel presents Δt_S^*, Δt_P^*, ΔT_S , ΔT_P from top to bottom of the stations located within 50 km of the cross-section (black-dotted lines). Bottom panel stations plot Δt_S^* values. Black contours indicate slab depth based on Slab 2.0 model (Hayes et al. 2018) at 20 km depth intervals.

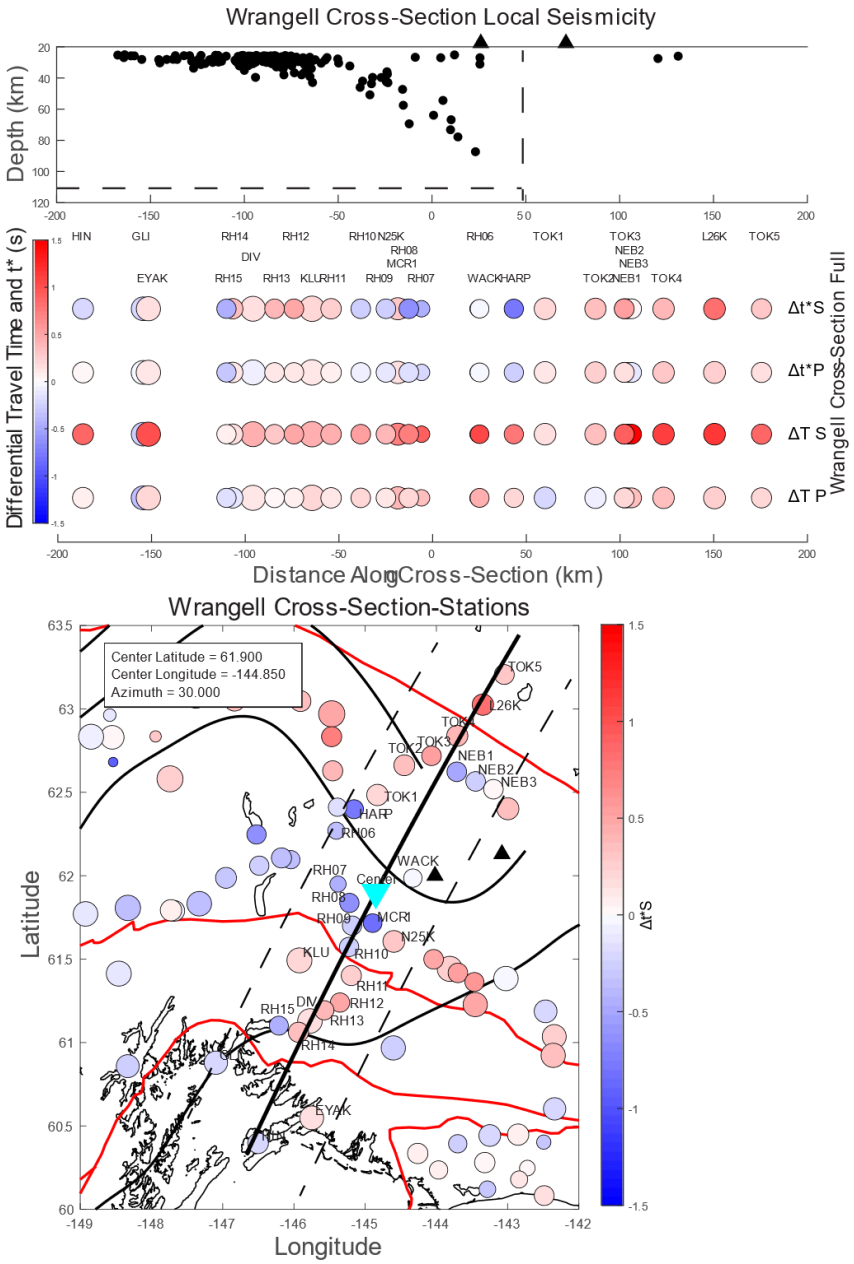

Figure 2.9 - Cross-section across the WVF indicating transition of the WVF subduction zone from forearc to arc and backarc. Top panel indicates local seismicity along cross-section (black bolded line) up to 25km away. Data obtained as described in Figure 2.8. Middle section presents Δt_S^*, Δt_P^*, ΔT_S , ΔT_P also as defined in Figure 2.8. Shapes are the same as described in Figure 2.4. Bottom section stations indicate Δt_S^* values. Black contours indicate slab depth based on Slab 2.0 model (Hayes et al. 2018) at 20 km depth intervals.

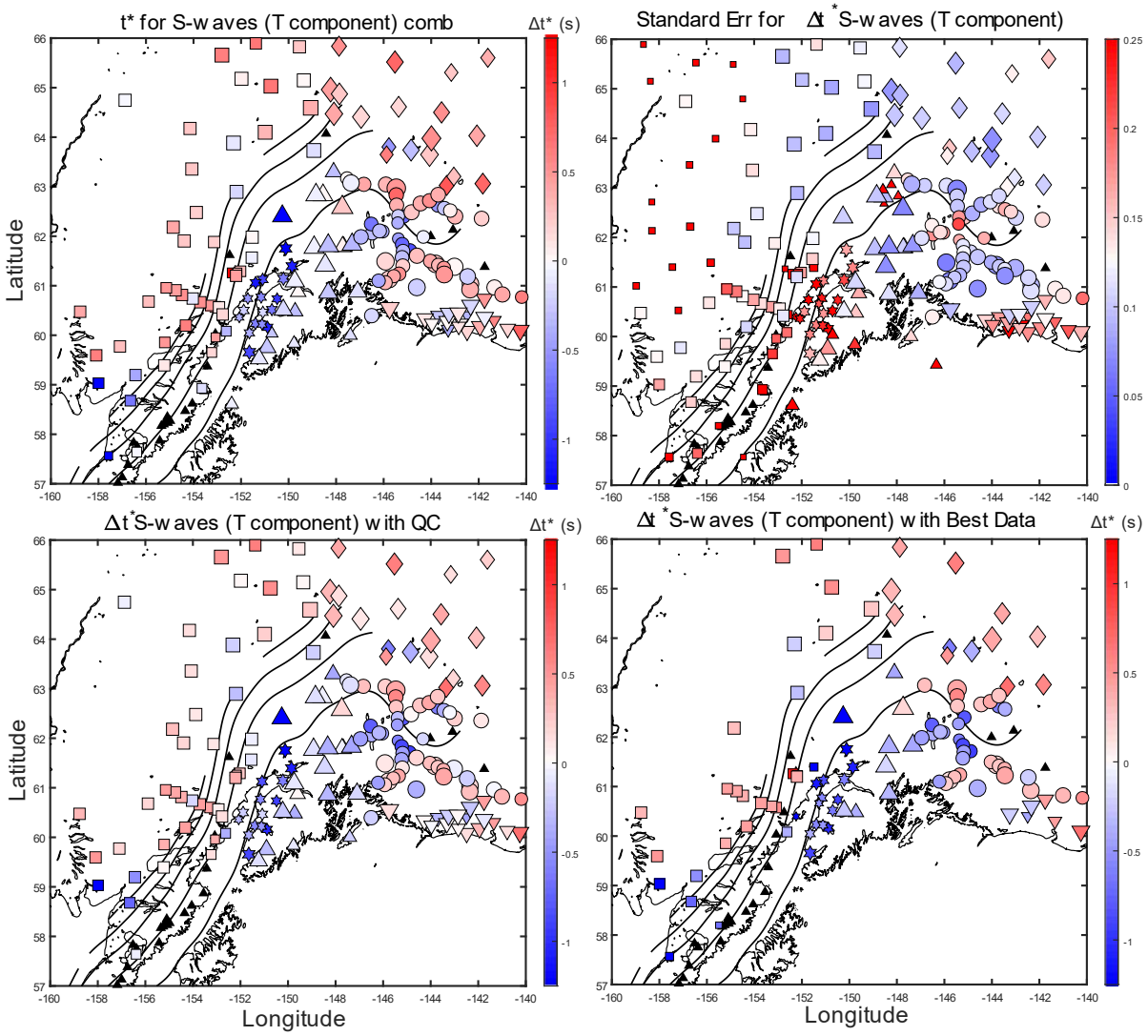

Figure 2.10 - Top left panel shows the station averaged Δt^*_S results assuming no frequency dependence ($\alpha = 0$) for the whole study region. The top right panel shows the standard error values for the results on the top left panel. These standard error values are calculated from the outlier-trimmed mean of the standard deviations per event at each station. The bottom left panel plots the aforementioned Δt^*_S results with stations containing at least 5 events of data and standard error values less than or equal to 0.25, for quality control. The bottom right panel plots Δt^*_S where the station averaged value (signal) is at least twice the size of the standard error, to identify the most significant signals. Fill, color, size and shape of stations follow the pattern described in Figure 2.4. Black lines indicate depth of subducting slab as indicated by WBZ seismicity at 40 km intervals. Black triangles refer the location of volcanoes.

Table 2.1 - Δt^* & ΔT in seconds, Results by Region – All Azimuths

Δt^*_S	Region 1 Aleutian Arc/Backarc	Region 2 Cook Inlet	Region 3 Aleutian Forearc	Region 4 Continental Interior	Region 5 Wrangell	Region 6 Yakutat
Median (s)	0.21	-0.61	-0.14	0.40	0.185	0.05
Mean (s)	0.10	-0.71	-0.18	0.38	0.056	0.08
2 Sigma	0.014	0.04	0.02	0.03	0.02	0.03
# of Events w/ Data	62	37	73	81	76	56

Δt^*_P	Region 1 Aleutian Arc/Backarc	Region 2 Cook Inlet	Region 3 - Aleutian Forearc	Region 4 Continental Interior	Region 5 Wrangell	Region 6 Yakutat
Median (s)	0.07	-0.33	-0.01	0.187	0.016	0.009
Mean (s)	0.03	-0.33	0.00	0.177	0.014	0.015
2 Sigma	0.005	0.010	0.011	0.009	0.006	0.013
# of Events w/ Data	63	38	74	82	77	57

ΔT_S	Region 1 Aleutian Arc/Backarc	Region 2 Cook Inlet	Region 3 Aleutian Forearc	Region 4 Continental Interior	Region 5 Wrangell	Region 6 Yakutat
Median (s)	-0.44	0.10	-1.13	0.11	0.71	1.76
Mean (s)	-0.60	0.06	-0.95	0.02	0.64	1.80
2 Sigma	0.02	0.08	0.06	0.09	0.03	0.04
# of Events w/ Data	62	37	73	81	76	56

ΔT_P	Region 1 Aleutian Arc/Backarc	Region 2 Cook Inlet	Region 3 Aleutian Forearc	Region 4 Continental Interior	Region 5 Wrangell	Region 6 Yakutat
Median (s)	-0.144	0.07	-0.369	-0.14	0.192	0.63
Mean (s)	-0.183	0.10	-0.334	-0.10	0.191	0.64
2 Sigma	0.007	0.03	0.02	0.03	0.010	0.02
# of Events w/ Data	63	38	74	82	77	57

Table 2.2 - Δt* & ΔT Results by Region – Azimuthally Split East Events

Δt^*_S - East	Region 1 Aleutian Arc/Backarc	Region 2 Cook Inlet	Region 3 Aleutian Forearc	Region 4 Continental Interior	Region 5 Wrangell	Region 6 Yakutat
Median	0.01	-0.81	-0.07	0.38	0.042	0.23
Mean	0.00	-0.76	-0.13	0.31	0.009	0.26
2 Sigma	0.03	0.04	0.03	0.04	0.02	0.05
# of Events w/ Data	45	25	52	56	52	39

Δt_P^* - East	Region 1 Aleutian Arc/ Backarc	Region 2 Cook Inlet	Region 3 Aleutian Forearc	Region 4 Continental Interior	Region 5 Wrangell	Region 6 Yakutat
Median	-0.03	-0.29	-0.06	0.14	0.00	0.02
Mean	-0.04	-0.28	-0.06	0.15	0.00	0.03
2 Sigma	0.007	0.010	0.011	0.013	0.007	0.014
# of Events w/ Data	45	25	52	56	52	39

ΔT_S - East	Region 1 Aleutian Arc/ Backarc	Region 2 Cook Inlet	Region 3 Aleutian Forearc	Region 4 Continental Interior	Region 5 Wrangell	Region 6 Yakutat
Median (s)	-1.35	0.32	-0.53	0.17	0.70	2.58
Mean (s)	-1.37	0.37	-0.39	0.20	0.77	2.51
2 Sigma	0.014	0.08	0.02	0.03	0.011	0.03
# of Events w/ Data	45	25	52	56	52	39

ΔT_P - East	Region 1 Aleutian Arc/ Backarc	Region 2 Cook Inlet	Region 3 Aleutian Forearc	Region 4 Continental Interior	Region 5 Wrangell	Region 6 Yakutat
Median (s)	-0.323	0.24	-0.17	0.03	0.199	0.65
Mean (s)	-0.332	0.25	-0.13	-0.02	0.184	0.75
2 Sigma	0.014	0.04	0.02	0.03	0.011	0.03
# of Events w/ Data	45	25	52	56	52	39

Table 2.3 - Δt* & ΔT Results by Region – Azimuthally Split West Events

Δt^*_S - West	Region 1 Aleutian Arc/ Backarc	Region 2 Cook Inlet	Region 3 Aleutian Forearc	Region 4 Continental Interior	Region 5 Wrangell	Region 6 Yakutat
Median (s)	0.340	-0.63	-0.27	0.30	-0.014	-0.02
Mean (s)	0.292	-0.67	-0.30	-0.06	-0.058	-0.07
2 Sigma	0.020	0.04	0.02	0.03	0.015	0.03
# of Events w/ Data	17	12	21	25	24	17

Δt^*_P - West	Region 1 Aleutian Arc/ Backarc	Region 2 Cook Inlet	Region 3 Aleutian Forearc	Region 4 Continental Interior	Region 5 Wrangell	Region 6 Yakutat
Median (s)	0.058	-0.36	-0.05	0.08	-0.023	-0.01
Mean (s)	0.058	-0.35	-0.05	0.11	-0.035	0.00
2 Sigma	0.010	0.01	0.01	0.01	0.006	0.01
# of Events w/ Data	18	13	22	26	25	18

ΔT_S - West	Region 1 Aleutian Arc/ Backarc	Region 2 Cook Inlet	Region 3 Aleutian Forearc	Region 4 Continental Interior	Region 5 Wrangell	Region 6 Yakutat
Median (s)	0.096	-0.13	-1.13	-0.02	0.415	-1.13
Mean (s)	0.180	-0.28	-1.10	-0.18	-0.229	1.32
2 Sigma	0.066	0.08	0.06	0.11	0.026	0.04
# of Events w/ Data	17	12	21	25	24	17

ΔT_P - West	Region 1 Aleutian Arc/ Backarc	Region 2 Cook Inlet	Region 3 Aleutian Forearc	Region 4 Continental Interior	Region 5 Wrangell	Region 6 Yakutat
Median (s)	-0.115	-0.07	-0.37	-0.12	0.241	0.63
Mean (s)	-0.067	-0.04	-0.36	-0.07	0.243	0.61
2 Sigma	0.026	0.06	0.02	0.04	0.010	0.02
# of Events w/ Data	18	13	22	26	25	18

CHAPTER 3

Discussion & Conclusions

3.1 Discussion Overview

Broadly, our results coincide with our expectations within the Alaskan-Aleutian subduction region. First, ΔT results show slow arrivals above the Cook Inlet (Region 2) and relatively slower arrivals above the arc and back arc (Region 1) relative to the forearc (Region 3). In comparison, Δt* results show low attenuation above the forearc and Cook Inlet and high attenuation above the arc and backarc. On the west side of the Continental Interior region (Region 4), ΔT results show fast arrivals that indicate likely subducting material as seen in recent seismic velocity analyses based on similar data (Wang and Tape, 2014; Martin-Short et al., 2018). The Δt* results of high attenuation in the same region support this interpretation as this pattern closely resembles the arc and back arc region (Region 1) high attenuation results for slab depths of 80km or greater.

These results suggest that Δt* results are highly sensitive to high temperature and possibly melt within the wedge while ΔT results are probably less sensitive to those features and more sensitive to the cold slab beneath. By contrast, Δt* above Cook Inlet (Region 1) is the lowest attenuation feature in the study region, seemingly not affected by the sediment effects that are likely the cause for arrivals. Similar patterns of low attenuation provide evidence for subduction in the WVF. The ΔT results in also show an overall slowing of arrivals jointly with low attenuation. The Yakutat region (Region 4) attenuation results reveal underlying complexity that is otherwise obscured by the slow ΔT results there. In addition to the large-scale tectonic

interpretations, this analysis also demonstrates the strengths of teleseismic attenuation measurements for discerning geologic structure beneath seismically slow sedimentary basin.

3.2 Attenuation in South Central Alaska

3.2.1 The Aleutian Subduction System

The teleseismic attenuation methods employed by this study (Eilon and Abers 2017) have not been used before to study subduction zones. We hope to gage the effectiveness in this setting by studying the attenuation results within a baseline region (Regions 1,2,3) of typical subduction behavior. The Alaskan-Aleutian subduction region was chosen due to the dense seismic arrays there, the abundance of intermediate-depth earthquakes that clearly define the subducting Pacific plate, and the existence of a well-defined volcanic arc. Comparing these results to previous attenuation results in the area (Stachnik et al. 2004) and previous geologic interpretations from seismic velocities (Eberhart-Phillips et al. 2006; Kim et al. 2014; Wang and Tape 2014; Jiang et al. 2018; Martin-Short et al. 2018) provides context to better interpret results in more complex regions like the WVF (Region 5) and in future subduction zone studies.

The Δt* results from Figure 2.5 indicate a broad region of low attenuation from the Kenai Peninsula to the edge of the volcanic arc, adjacent to a broad region of high attenuation at greater slab depths. This pattern resembles previous local earthquake attenuation results (Stachnik et al. 2004). We also look at Δt_S^* results assuming no frequency attenuation, in addition to employing various quality control measures like excluding high standard error stations or excluding stations whose absolute value is less than their standard error (Figure 2.10). Even in these cases, the main signals of the low attenuating, cold forearc and the high attenuating, hot mantle wedge are clear.

This suggests that these teleseismic Δt* results can adequately assess attenuation and are sensitive to mantle wedge structure, not deeper.

3.2.2 Attenuation as Evidence for Subduction in the Continental Interior

In the Continental Interior region (Region 4) some recent velocity studies see a high velocity anomaly indicative of a subducting slab east of the edge of the WBZ (Wang and Tape 2014; Jiang et al. 2018) and some do not (Martin-Short et al. 2018). Our Δt* results indicate highest median Δt* values of the whole study area in this region. This broad swath of high attenuation is most similar to the volcanic Arc/Backarc Region (1) results, both in uniformity and in magnitude. This comparison would suggest that the high attenuation could be caused by high mantle temperatures and/or melt derived from an extension of Pacific/Yakutat slab subduction in this region east of the WBZ.

3.2.3 Subduction Origins of Attenuation in the WVF

In the WVF region (Region 5), Δt* (Figure 2.5) shows a clear low connected to the Aleutian subduction low attenuation region to the west and high attenuation regions to the north and south. This low attenuation region corresponds to the inferred for subduction beneath the WVF local WBZ seismicity (Daly et al. 2019) and receiver function imaging (Mann et al. 2019) (Figure 2.8). Thus, we can interpret the presence of a slab beneath the WVF as suggested by recent studies of seismic velocity in the region (Jiang et al. 2018).

To understand the complex pattern of attenuation in the WVF region (Region 5), it is useful to compare this region with the Aleutian subduction region (Figures 2.8, 2.9). In the latter (Figure 2.8), low attenuation corresponds to fast arrivals in the forearc (outside the Cook Inlet) and extends to stations overlying slab depths of down to 80 km. Assuming both the attenuation

and slowing of the results at these stations can be attributed exclusively to the mantle wedge between the slab and station, we can compare these results with previous tomography studies of the region. Our results suggest a boundary of lower attenuation to higher attenuation at a similar depth (80 km) compared to the 75 km reported in Stachnik et al. (2004). Comparing these observations to the WVF cross section (Figure 2.9), the low attenuation seems to begin at stations overlying slab depths of approximately 40 km and extend to a deeper depth of 100 km. The terminal depth of 100 km is deeper than the results from both the Aleutian subduction cross section (Figure 2.8) and previous studies of the Aleutian subduction zone attenuation, but within uncertainty. The similarities in overall pattern also suggests a subduction arc volcanism source for the attenuation and magmatism of the WVF.

There is a zone of high attenuation directly south of the WVF ends that extends to 40 km and corresponds to a region of high shallow seismicity across depths from 25 to 40 km. This zone does not align with our expectations of local slab geometry based on local seismicity data and previous results. One possible explanation for this high attenuation anomaly could be crustal processes from the accretion of the Yakutat terrane to the south, but ultimately additional study will be required to provide more definitive interpretations.

Overall, the teleseismic Δt^* results strongly resemble local earthquake attenuation (Stachnik et al. 2004) but provide much wider areal coverage. Although most recent seismic velocity studies (Wang and Tape 2014; Jiang et al. 2018; Martin-Short et al. 2018) are unclear as to the existence of the subducting slab in this region, this study benefits from the WVLF seismic array data that boosts resolution in this key region. These are the first images of attenuation east of the Aleutian subduction region as well as for subduction beneath the Wrangell Volcanic Field. These images also support the existence of a subducting slab beneath and continuing to the

northeast of the WVF Region (Region 5). The source of the high attenuation anomaly directly south of this region is still not well understood, but the boundary from low to high attenuation near where the slab is 100 km deep closely resembles the Aleutian region. The attenuation results do not directly image the subducting slab segment extending beyond the edge of the WBZ in the Continental Interior (Region 4).

3.3 Slab Geometry - Evidence from Travel Times

The primary use of ΔT data in this study is for the purpose of jointly interpreting it alongside Δt* data to provide context for the influence of temperature, surficial sediments, and the presence of melt on attenuation. Increased temperature leads to decreased seismic velocity and an increase in attenuation (Romanowicz, 1995; Jackson et al. 2002). The porosity of sediments significantly slows velocities with little effect on attenuation (Darot and Gueguen 1981) and the geometry of melt in pores either has little effect on attenuation and significant effect on shear velocity (Hammond and Humphreys 2000a,b; Takei 2000) or has a significant effect on attenuation and less effect on velocity (Jackson et al. 2004; Dalton et al. 2009; McCarthy et al. 2011; Holtzmann 2016). Throughout the study region, the ΔT results are consistent with the thermal influences of subduction structures and with the sediment-induced slowing through basins.

The swath of fast arrivals in the Alaskan-Aleutian forearc (Region 3), arc and back-arc (Region 1) and Continental Interior regions (4) can be attributed to the cold subducting material of Pacific and Yakutat plates in these regions (Kim et al. 2014; Wang and Tape 2014; Abers et al. 2006). This is further supported by the gradient toward slower arrivals at stations overlying deeper slab depths seen in the ΔT results of Region 1, reflective of increasing temperatures

further into the back-arc of the subduction region (Syracuse et al. 2010). This gradient of slowing arrivals in the direction of increasing slab depths continues beyond the edge of the Wadati-Benioff Zone (WBZ) seismicity and north of the Denali Fault, reflecting a possible extension of Pacific plate subduction suggested by seismic velocity analyses (Martin-Short et al. 2016; Jiang et al. 2018).

This subduction zone influence is not seen in the ΔT results in the WVF (Region 5) where instead the arrivals are just broadly slow. This stands in contrast to the WBZ seismicity (Daly et al. 2019) seen in Figure 2.9 and some seismic velocity tomography studies (Jiang et al. 2018) that indicate a likely slab presence in the region. The seismicity and imaging only indicate a slab extending to 100 km, so it is possible that in contrast to the Alaska-Aleutian subduction, subduction in the WVF does not extend deeper and the lack of fast arrivals reported are a result of that.

3.4 Sedimentary Structures - Attenuation and Travel Times

Attenuation and travel time results overlying sedimentary structures generally show large deviation from the relationship between travel time and attenuation observed in the Aleutian Subduction region (Regions 1, 3) (Figure 3.1). Cook Inlet Basin (Region 2) geology is linked with lowered Δt* in the region, especially for the P phase, even in comparison to the low attenuation forearc region (3). The broad pattern of low attenuation in the region is difficult to adequately explain, given the slowed ΔT results that are likely induced by sediments. The extent of both the low attenuation yet slow travel time arrivals are limited to within the Cook Inlet Basin. Curiously, the same pattern does not describe the Yakutat terrane (Region 6) Δt* results which display a mix of high and low attenuation. To get a better understanding of the underlying

signal, we look to the quality controlled Δt* results that only show stations whose signal is twice their respective standard error (Figure 2.10). There is a clear division in structure from the low Δt* in the west of the Yakutat terrane that transitions quickly to high Δt* in the east. The difference in attenuation results between the regions suggests that either the effects of the shallow sedimentary Cook Inlet Basin are not the same as those of the sedimentary cover sequence of the Yakutat region, or that deep structure signals in the Yakutat region are imaged by the attenuation.

The influence of sediments from the Cook Inlet Basin and Yakutat Terrane (Plafker and Berg 1994; Swenson 1997) on travel times can be interpreted in regions 2 and 6 respectively of the study region, possibly obfuscating deep structure signals. The Cook Inlet Basin (Region 2) ΔT results demonstrate that slow arrivals dominate the region regardless of the cold subducting slab situated directly underneath. Similarly, the Yakutat Terrane shows broadly slow arrivals, in contrast to the complex pattern of high and low Δt* results. These findings suggest that these sediments are likely to be a complicating factor for interpretations in more complicated tectonic regions (Region 6). This idea is supported by previous studies of seismic velocity tomography in the area that also show strong low velocity anomalies in the shallow structure of the same regions (Eberhart-Phillips et al. 2006; Ward 2015; Martin-Short et al. 2018; Jiang et al. 2018). We also note a similar phenomenon occurring in the Copper River Valley located just west of the WVF, where ΔT is broadly high and Δt* is low.

When comparing the ΔT results of these slow arrival regions to the Δt* results, we might expect that porous sediments would lead to increased attenuation, but the results show that not to be the case. Instead generally low attenuation is reported in these regions, which could be explained by seismic wavelengths much larger than the thicknesses of basins which might

otherwise cause scattering. This would suggest that teleseismic attenuation is a powerful tool for imaging deep structure otherwise obscured by sedimentary basins.

3.5 Constraining the Impact of Temperature and Melt with Travel Time Data

The covariation of ΔT for P and S can act as a proxy for the material properties such as temperature (Hales and Doyle, 1967). Because the effects of temperature, melt and oxygen fugacity jointly impact attenuation as previously described, it is useful to constrain the potential impact of temperature separately. This study calculates $\Delta(\ln V_S)/\Delta(\ln V_P)$ as a measure of the covariation of ΔT for P and S. It is compared to previous estimates from experimental studies (Hammond and Humphreys 2000b; Takei 2002) and used to interpret whether temperature alone (Koper et al. 1999; Wiens et al. 2008) could be contributing to attenuation. When gauging the impact of temperature, $\Delta(\ln V_S)/\Delta(\ln V_P)$ values from 1.2 to 1.4 have been attributed to temperature effects at mantle wedge pressure and temperatures (Anderson et al. 1992) though some studies have attributed values as high as 2 to temperature effects alone at high temperatures where Q is important (Wiens et al. 2008). At high temperatures, the effects of Q will lead to higher $\Delta(\ln V_S)/\Delta(\ln V_P)$ values (Karato, 1993). With regards to the impact of melt, textually equilibrated melt geometry could be responsible for values from 1 to 1.5 and higher values of 1.7 to 2.3 could be attributed to melt or fluid distributed in dikes and veins (Takei 2002).

This study follows the methods of Koper et al. (1999) to constrain the effects of temperature along the Aleutian subduction system (Regions 1,3) and the WVF (Region 5). For a perturbation in velocity due to material properties, the perturbation of travel times to first order follows the equation (Koper et al. 1999):

$$\delta T = -L \frac{\delta V}{V^2}, \tag{17}$$

Where δV and δT are the velocity and travel time perturbations, L is the path length of the seismic rays from where they diverge between stations and V is the path-averaged velocity. Assuming the effect of path geometries are negligible when compared to the effect from velocity perturbations, there exists a linear relationship between P and S travel time residuals following the equations (Hales and Doyle, 1967):

$$\delta T_S = a\delta T_P + b, \tag{18}$$

Where,

$$a = \frac{\delta \ln V_S}{\delta \ln V_P} * \frac{V_P}{V_S} . \tag{19}$$

The parameter a as the slope of the best-fit linear trend between T_S & T_P. Here, V_S & V_S are the P and S phase velocities, and $\Delta(\ln V_S)/\Delta(\ln V_P)$ as their relative fractional covariation. This relative variation value is calculated from the estimates for a, assuming V_S/V_P ranging from 1.73 to 1.85.

The regionalized T_S & T_P data (Figure 2.4) in Regions 1 and 3 form the reference Alaskan-Aleutian subduction region outside of the Cook Inlet Basin. The $\Delta T_S/\Delta T_P$ slope is calculated with the Reduced Major Axis (RMA) regression method (Wessel 2016), and the upper and lower 95% confidence intervals were calculated through bootstrapping with 1000 trials (Figure 3.2). The resulting best fit slope $\Delta T_S/\Delta T_P$ for measurements from western back azimuths is 2.8 (95% confidence range [2.5 - 3.1]) and the $\Delta(\ln V_S)/\Delta(\ln V_P)$ ratio is 1.5 [1.4 – 1.7] for V_S/V_P = 1.81 (Dziewonski and Anderson, 1981). In comparison, the east back azimuths for the same region have a slope $\Delta T_S/\Delta T_P$ of 4.3 [3.6 - 5.4] giving $\Delta(\ln V_S)/\Delta(\ln V_P)$ ratios of 2.4 [2.0 – 3.0], significantly higher than for the west back azimuths. Previous estimates of $\Delta(\ln V_S)/\Delta(\ln V_P)$ (Anderson et al. 1992; Takei 2002) suggest values of 1.5 are slightly higher than expected for

temperature alone (1.2-1.4) and similar to expectations for textually equilibrated melt (1-1.5), although this is still within the range of values attributed to temperature when physical dispersion is considered (1.5-1.8) (Wiens et al. 2008). By contrast east back azimuth $\Delta(\ln V_S)/\Delta(\ln V_P)$ of 2.3 are much higher than what have been attributed to temperature alone or text equilibrated melt and instead fall within the outer range of what has been attributed to melt or fluid arranged in a dike or vein geometry (1.7-2.3) (Takei 2002) as observed in other areas like Iceland and northeastern Japan (Gebrande et al. 1980; Nakajima et al. 2001).

The west back-azimuth events in this region sample the mantle wedge beneath the arc and backarc (Region 1), where the velocity perturbations are likely driven by a combination of high temperature and textually equilibrated melt distribution. This combination of effects is in line with our expectations for a mantle wedge with arc volcanism driven by melt. By contrast, the east back-azimuth rays interpreted as sample the dehydrating segment of the subducting slab, where the geometry of fluids can induce greater changes in V_S than predicted by temperature or textually equilibrated fluids. One possible interpretation is that the melt in the wedge is present and textually equilibrated, and the presence of dikes and veins of melt or fluid around the dehydrating subducting slab is responsible for the difference in results.

Regressions for the Wrangell Volcanic Field (Region 5, Figure 3.3) indicate lower $\Delta T_S/\Delta T_P$ than those recorded in the Aleutian subduction region, giving a $\Delta(\ln V_S)/\Delta(\ln V_P)$ ratio of 1.4 [1.2 – 1.7] for western back azimuths and 1.2 [0.9 – 1.4] for eastern back azimuths. These suggest that the source could be contributed entirely to temperature (Anderson et al. 1992) or a textually equilibrated melt pattern (Takei 2002). The west back-azimuth results are the generally same as the results for the Alaskan Aleutian regions (Regions 1,3) suggesting temperature alone or textually equilibrated melt could be responsible for these as well. The east back-azimuth

results show the opposite pattern of very low $\Delta(\ln V_S)/\Delta(\ln V_P)$ values, suggesting either lower temperatures, less melt or fluid and/or more textually equilibrated melt or fluid in high-aspect ratio pores within WVF than the Alaskan-Aleutian Region (Takei, 2002). This azimuthal difference within the WVF (Region 5) could be attributed to the orientation of slab geometry beneath the WVF and extending to the northeast in this region.

3.6 Comparison of Travel Times and Tstar Results

We compare ΔT and Δt* using the ratio of Δt* to ΔT across a region that is geologically simple (Alaskan-Aleutian Region 1,3) to predict ΔT from Δt* in regions that are more geologically complex (Continental Interior, Wrangell, & Yakutat Regions 4,5,6). The misfit between predicted and observed ΔT data provides insight into their covariation (Figure 3.1). The areas with greatest spatial variation are then interpreted as experiencing the most non-temperature effects. To perform this analysis, the best fit slopes between ΔT and Δt* for both S and P phases are calculated for the west-azimuth events for the Aleutian subduction region (Regions 1,3) because the ray-paths of the west-originating events best sample the mantle wedge to the west and show $\Delta(\ln V_S)/\Delta(\ln V_P)$ ratio of 1.4 ~ 1.5 consistent with a temperature source for the attenuation. The correlation slope dt^*/dT is approximately 0.49 for both P and S. We define a reduced travel time $\Delta T_{RED} = (\Delta T - \Delta t^*/0.49)$ for both P and S. The process is performed for each phase and azimuthally divided to produce 4 residual plots for the whole study region (Figure 3.1).

Patterns fall into one of two categories, the first where arrival times are slower (more positive) than predicted by attenuation, which correspond to the Cook Inlet Basin and the Copper River Valley (Regions 2, 5). The results from these regions suggest the sediments affect the travel times more strongly than the attenuation. The second category is where attenuation

predicts slower arrival times than observed (i.e. the residuals are negative), and this occurs along the Aleutian forearc and volcanic arc (Regions 1, 3) and in the Continental Interior and north of the WVF (Regions 4,5). This pattern can be predominantly attributed to the high attenuation areas in these regions that simultaneously report relatively fast arrivals, possibly due to the greater influence temperature plays on attenuation than seismic velocities or melt effects. While the Continental Interior region has no active volcanism to speak of, in both the WVF and the Aleutian volcanic arc region, the largest variation occurs behind the volcanic arc relative to subduction.

3.7 Effect of Bulk Modulus Relaxation

Intrinsic attenuation can be broken down into components of shear modulus relaxation and bulk modulus relaxation, and their ratio can indicate what processes are responsible (Faul et al. 2004; Wiens et al. 2008; Jackson and Faul 2010). We can obtain this ratio by using equation (3) assuming a V_P/V_S ratio of 1.81 from the Preliminary Reference Earth Model (PREM by Dziewonski and Anderson 1981) at 410 km depth. First the RMS slope of the Δt_S^*-Δt_P^* regression is calculated (Figures 3.4, 3.5) to produce a $\Delta t_S^*/\Delta t_P^*$, which is $(Q_P/Q_S)(V_S/V_P)$. Then we divide by the V_P/V_S ratio to estimate Q_P/Q_S. Results (Table 3.1) indicate that in all cases but the Aleutian Forearc and Continental Interior regions (Regions 3, 4) Q_P/Q_S ratios are within error margin of the one-one line indicating nearly equal bulk and shear attenuation. This suggests either bulk modulus relaxation is present, possibly due to bulk fluid flow (Wiens et al. 2008), or some source of extrinsic attenuation is responsible.

3.8 Extrinsic Vs. Intrinsic Attenuation

Measurements of Δt* indicate apparent attenuation in our study region – although the discussion has only considered intrinsic effects (energy loss during propagation), extrinsic attenuation (changes in frequency content due to elastic processes) may be important. Extrinsic effects include frequency-dependent elastic scattering, short-period defocusing and long-period focusing. Most models of elastic scattering would predict $Q_P \approx Q_S$ (Richards and Menke, 1983), and our earlier measurements of Q_P/Q_S (Table 3.1) that this condition is true for the Aleutian Forearc (Region 3) and Yakutat Terrane (Region 6) data, meaning we should be concerned about elastic scattering in those regions increasing the apparent attenuation measured. Elastic scattering would also cause strong coda energy for arrivals with high apparent attenuation, which we did not find to be the case in our high attenuation regions.

To address possible focusing locally around the subducting slabs, we look to previous studies (Allen et al. 1999) that indicate high travel time delays (~5 s) relative to unscattered arrivals could indicate short period defocusing. Our results are made at ≤ 0.5 Hz frequency and probably controlled by the highest frequencies we observe (Stachnik et al., 2004). Calculating the thickness of a scatterer using the frequency and velocity give us length scales of 30 km to 90 km needed to defocus the body waves depending on depth and phase, and we only see delays across those distances within the Cook Inlet. Most of the variations in Δt* we observe are at much longer wavelengths. It is conceivable that high frequency energy is focused in the Cook Inlet as a result of the slab and it could explain the anomalously low Δt* seen in the region. However, the lack of azimuthal variation seen in Δt* seems to indicate that there is no such focusing happening at depth. Otherwise, it is possible at these length scales for the slab to be acting as a scatterer, but given the travel time delays change gradually across the study area and

t* results are persistent over larger areas than could be affected by a scatterer of the slab's thickness, this seems unlikely.

3.9 Comparison to Previous Studies

To compare the Δt* results reported in this study against results from previous subduction zone attenuation studies both in Alaska and around the world, we convert the Δt* results to Q^{-1} values and use the results that assume no frequency dependence (Table A.2). To make this conversion, a reference length L and an average velocity must be assumed and Δt* results must be fixed at a minimum value corresponding to $Q^{-1} = 0$. This study uses an approximation to Equation (2) to convert Δt* results to Q^{-1} values:

$$(\Delta t^*_{station} - \Delta t^*_{baseline}) = \frac{410\ km}{9.19\ \frac{km}{s}} * \frac{1}{Q}, \quad (20)$$

To find a minimum Δt*, the Δt^*_S & Δt^*_P are regressed against each other for each station, and then any stations further than 3 standard deviations from the best fit line are trimmed away. The lowest 10th percentile from the remaining Δt^*_S & Δt^*_Presults are selected as the baseline Δt* value which is subtracted from all Δt* results (Figure 3.6). The 10th percentile cutoff is chosen to trim outlier data that lies far from the core clustering of Δt* data. We create 2 separate models with different lengths L and corresponding average velocities. Results are corrected to 1Hz assuming frequency dependence of $\alpha = 0$ for better comparison to previous attenuation results in the region (Stachnik et al. 2004).

The first model interprets the source of attenuation constrained to the lithosphere so an L of 220 km is used corresponding to the depth of the low velocity asthenosphere and a V_P & $V_S$of 8.56 and 4.64 km/s derived from the PREM model (Dziewonski & Anderson, 1981). The second

model interprets the source of attenuation as occurring within the upper mantle to a length L of 410 km for a V_P & V_S of 9.19 km/s and 4.96 km/s respectively, also from PREM. The second model is a more conservative model since the attenuation source is spread over a wider length thus lowering 1/Q. Figure 3.6 shows the converted Δt* results as $1000/Q$ values to match the notation used by Stachnik et al. (2004). The $1000/Q$ results show maximum values of 14-16 and 17-21 for P and S with the upper mantle model, located in the Aleutian backarc (Region 1), the Continental Interior Region (4), and north and south of the WVF (Region 5). Attenuation is lowest in the Cook Inlet and at the center of the amagmatic volcanism of the Alaska range, ranging mostly from 0-2 in P and 0-5 in S results.

Comparing these results to those of Stachnik et al. (2004), most of our study region reports higher attenuation than described in Stachnik et al. They report their highest attenuation in $1000/Q_S$ values of 3-4.5 within the mantle wedge assuming no frequency dependence. To compare, we calculate the mean of the $1000/Q_S$ values with no frequency dependence in regions we think represent the mantle wedge, the Continental Interior and Aleutian Arc (Regions 4, 1) (Figure 3.6), which is 23.5 for the most similar path length model (220km). The higher frequency data (9 Hz) used by Stachnik et al. should skew higher frequencies towards lower attenuation results (Stachnik et al. 2004) if you assume some frequency dependence of attenuation (Jackson et al. 2002). It is also important to note that the path lengths used in Stachnik et al. are much shorter (generally 80-150 km) than the path length of the shortest model used here (220 km). This means that our study accumulated attenuation over a larger path, which could also contribute to the difference in reported attenuation values.

To study if the effects of frequency would be enough to explain the difference, we can estimate the frequency dependence needed to correct for the differences, using the following equation that can be directly derived from equation (6):

$$\log(Q_2/Q_1) = \alpha * \log\left(\frac{f_{R1}}{f_{R2}}\right) \quad (21)$$

Where Q_1 and Q_2 are the calibrated 1000/Q results of Stachnik et al. and this study and f_{R1} and f_{R2} are their respective highest frequencies used in calculating attenuation, which for this study was 0.5 Hz and for Stachnik et al. at the mantle wedge was 9 Hz. Assuming both results are sampling the same signal, we can alter equation 21 to solve for the α that would be needed to compensate for the difference in results. Performing the calculation suggests that an $\alpha = 0.63$ would be required to compensate for the difference in results between the studies assuming they sample the same signal, which is greater than the 0.27 from previous observational and experimental results (e.g., Faul and Jackson, 2005; Rychert et al., 2008; Stachnik et al., 2004). Therefore, it is likely that the difference in frequency would not be enough to compensate for the difference in results and instead the difference in the paths sampled would be responsible.

The $1000/Q_P$ results can also be used to compare this subduction zone to others. The most recent such attenuation study is Wei and Wiens (2018) in the Lau back-arc basin, which assumes frequency dependence of 0.27 and reported similarly high $1000/Q_P$ attenuation values of nearly 20 observed in the backarc. In this case, that study corrected the data to 1 Hz, diminishing the impact of frequency differences. The authors suggest that the Lau back-arc basin is higher attenuating than Alaska as their comparison to Stachnik et al. suggests; other subduction zone temperature estimates support this conclusion (Abers et al 2014). Other subduction zone studies that also assume a frequency dependence of 0.27 report maximum

$1000/Q_S$ values of 30 beneath the Marianas volcanic arc (Pozgay et al. 2009) and 23 and 15 beneath Nicaragua and Costa Rica (Rychert et. al 2008). Compared to our peak reported $1000/Q_S$ values of 33-36 and considering the path lengths sampled are shorter, it can be said that both regions report higher attenuation and are likely hotter that our study area. Other subduction zone studies reflect much lower maximum $1000/Q$ values like $1000/Q_P$ near 5 in Kanto, Japan (Nakajima 2014), or near 5 beneath the volcanic section of the north island of New Zealand (Eberhart-Phillips et al. 2008). Comparisons with attenuation studies in other subduction zones indicate lower attenuation beneath south central Alaska than reported in the most attenuating subduction zones. The results trend to higher attenuation in comparison to previous studies of the region (Stachnik et al. 2004) likely due to the path lengths sampled and they expand the study region to a much wider scale.

3.10 Conclusions

This study applies a new teleseismic body-wave attenuation technique in a subduction zone setting, allowing us to characterize a tectonically complex region that would have suffered from poor sampling due to a lack of local seismicity in key areas of interest. Our results show that results from this method correspond closely to previous local earthquake attenuation results after accounting for frequency, and so could be used in the future to expand the coverage of attenuation studies in subduction zones across regions with little to no seismicity. These results can also help supplement the result of previous surface wave attenuation studies as teleseismic body waves provide finer horizontal resolution that is particularly useful in the heterogenous environments of subduction zones.

1. Attenuation shows a clear boundary between the hot mantle wedge and the cold forearc throughout the Alaska-Aleutian subduction and the Yakutat subduction system.
2. Attenuation is less obscured by basin effects than travel times, although Cook Inlet basin seems to induce low attenuation in addition to slow arrivals.
3. The Aleutian-Alaskan subduction region attenuation corresponds closely in magnitude and location of boundaries with Stachnik et al. 2004 attenuation results, and recent velocity tomography studies.
4. Analysis of $\Delta(\ln V_S)/\Delta(\ln V_P)$ from travel times suggests high temperatures and textually equilibrated melt or fluid in the mantle wedge of the arc to backarc (Region 1) and fluid in dike or vein geometries in the cold nose and forearc (Region 3) of the Alaska Aleutian subduction region.
5. In the WVF (Region 5), $\Delta(\ln V_S)/\Delta(\ln V_P)$ results indicate delays that could be attributed to temperature effects alone, or a combination of temperature and textually equilibrated melt.
6. Attenuation results support the existence of the eastward extension of the Pacific/Yakutat plate subduction past the east edge of the WBZ seismicity in the Alaskan Range, with low attenuation transitioning to high attenuation resembling the Aleutian Arc/Backarc transition from cold slab to hot mantle wedge.
7. The subduction of the Yakutat plate extends beneath the WVF and continues to the northeast as suggested by some recent velocity tomography studies (Wang and Tape 2014; Jiang et al. 2018).

8. The 1000/Q results suggest that south central Alaskan subduction is cooler than the hottest subduction zones worldwide.
9. Comparison to Q results from Stachnik et al. (2004) results in an estimate of frequency dependence 0.63, suggesting the main differences are due to path lengths sampled.

Ultimately, the travel time results serve as a strong support for interpreting attenuation and gauging the comparative strengths of each method for imaging deep structure in subduction zones. The results helps to identify the extension along strike of Pacific/Yakutat plate subduction in the Continental Interior region (4) that has been seen in some previous studies (Wang and Tape 2014; Jiang et al. 2018) but not seen in others (Martin-Short et al. 2018). The ΔT results are also greatly influenced by surficial geology like in the Cook Inlet in a way that obscures deeper subduction structures. The Δt^* results by contrast are more greatly influenced by deep Earth structure than by the sedimentary basins and so they can provide evidence for WVF subduction volcanism mechanics where ΔT data cannot. These results suggest that the measurement of teleseismic Δt^* in other subduction zones for joint interpretation alongside seismic velocity models would be able to expand our current understanding of the underlying structure in those regions, particularly where local earthquakes are scarce.

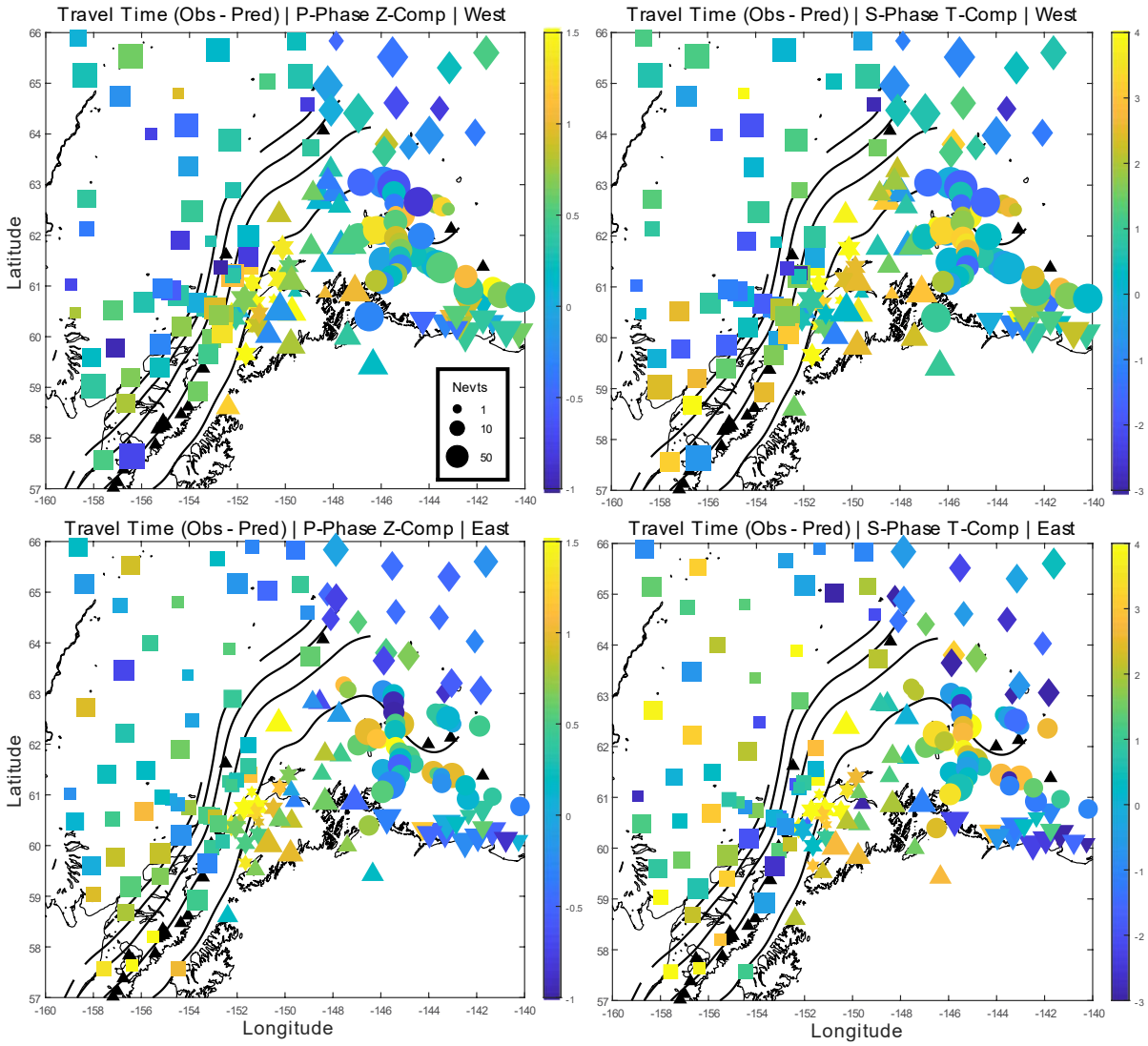

Figure 3.1 - Comparison of ΔT & Δt* at each station of observed ΔT minus predicted ΔT for both S and P phases and east and west originating events. The predicted ΔT is calculated using the best fit slope of the ΔT and Δt*, for the P and S phases of the west events (which are used as the baseline). The corresponding intercept value to the best fit slope is subtracted from the station averaged Δt* values and the result is divided by the best fit slope of the corresponding phase, to obtain a predicted ΔT value to calculate the residual with. The residual is plotted as the color of the circles that correspond to the station locations, and whose sizes depend on the number of measurements at each station. Shapes correspond to the regionalization on Figure 2.4.

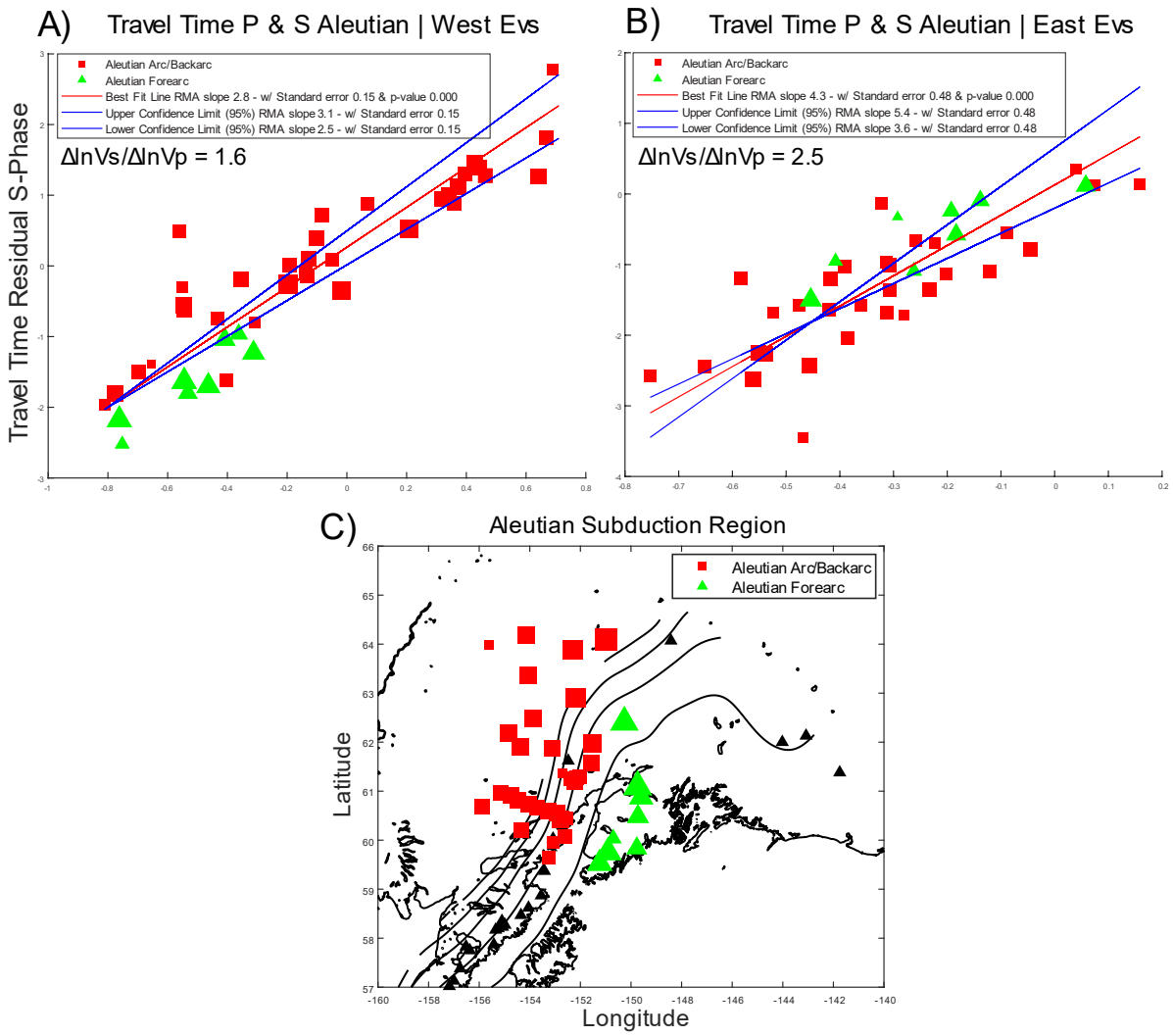

Figure 3.2 - Comparison of ΔT S and P phase results to obtain the relative slopes with corresponding standard error estimate. In panels A) & B) the red line is best fit line, and blue lines are upper and lower 95% confidence intervals of best fit line. The best fit slopes are used to produce $\Delta(\ln V_S)/\Delta(\ln V_P)$ ratios. The $\Delta(\ln V_S)/\Delta(\ln V_P)$ ratio for panel A) results are a best fit ratio of 1.5 and an upper limit of 1.7 and lower limit of 1.4. The $\Delta(\ln V_S)/\Delta(\ln V_P)$ ratio for the panel B) results are a best fit ratio of 2.4 and an upper limit of 3.0 and lower limit of 2.0.

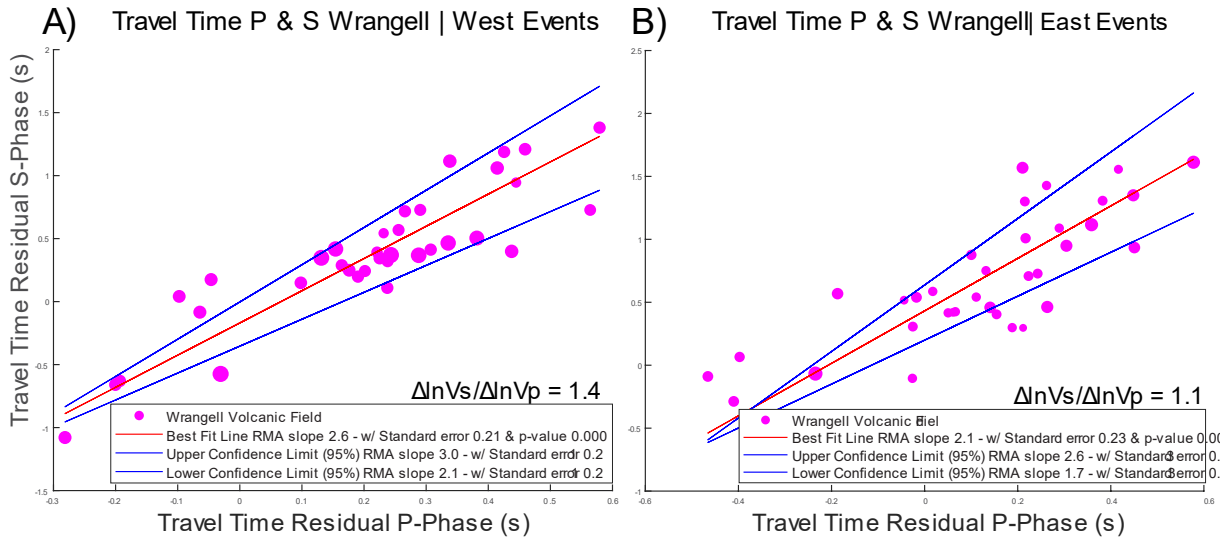

Figure 3.3 - Comparison of ΔT S and P phase results for the Wrangell region (5). In panels A) & B) the red line is best fit line, and blue lines are upper and lower 95% confidence intervals of best fit line. Best fit slopes are used to produce $\Delta(\ln V_S)/\Delta(\ln V_P)$ ratios. The $\Delta(\ln V_S)/\Delta(\ln V_P)$ ratio for panel A) results are a best fit ratio of 1.4 and an upper limit of 1.7 and lower limit of 1.2. The $\Delta(\ln V_S)/\Delta(\ln V_P)$ ratio for the panel B) results are a best fit ratio of 1.2 and an upper limit of 1.4 and lower limit of 0.9.

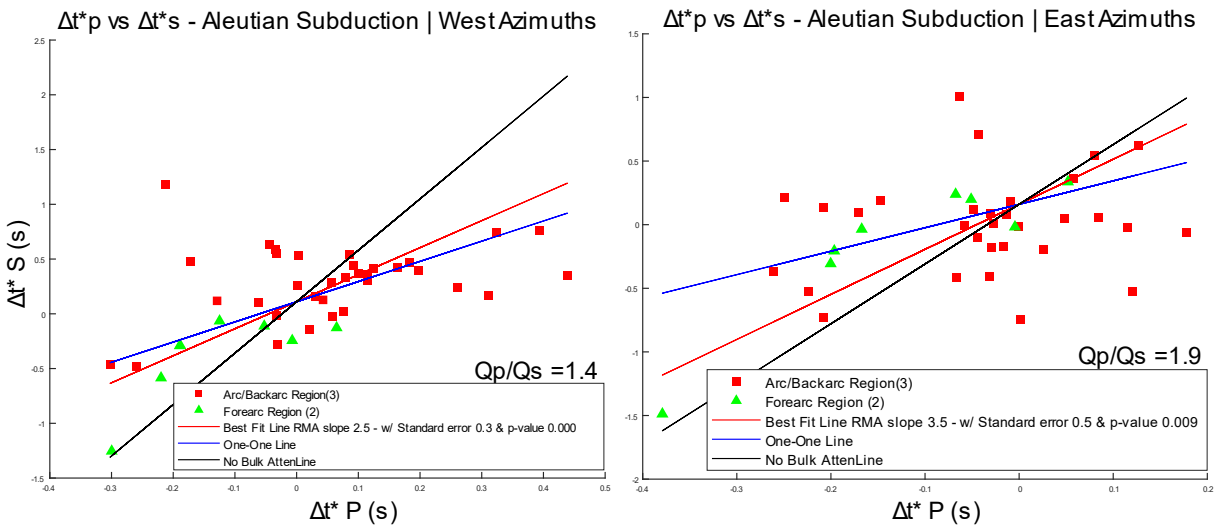

Figure 3.4 - Comparison of Δt* to obtain the relative slopes with corresponding standard error estimate. The green triangles and red squares are station averaged data of the Aleutian forearc and arc/backarc regions respectively. West events are shown on the left and east events on the right. Panels A) & B) Calculate best fit slopes that are then used to estimate Q_P/Q_S ratios by dividing by a V_P/V_S ratio of 1.81. The red line indicates best fit line, the blue line indicates when bulk and shear attenuation (Q_K & Q_μ) are approximately equal in proportion (Q_P/Q_S = 1) and the black line indicates when bulk attenuation is negligible (Q_P/Q_S ~ 2.45 for V_P/V_S = 1.81). The calculated Q_P/Q_S for the left panel is 1.4 with a standard error of 0.2, and the Q_P/Q_S for the right panel is 1.9 with a standard error of 0.3. The stations chosen to correspond to the station map shown on Figure 3.1.

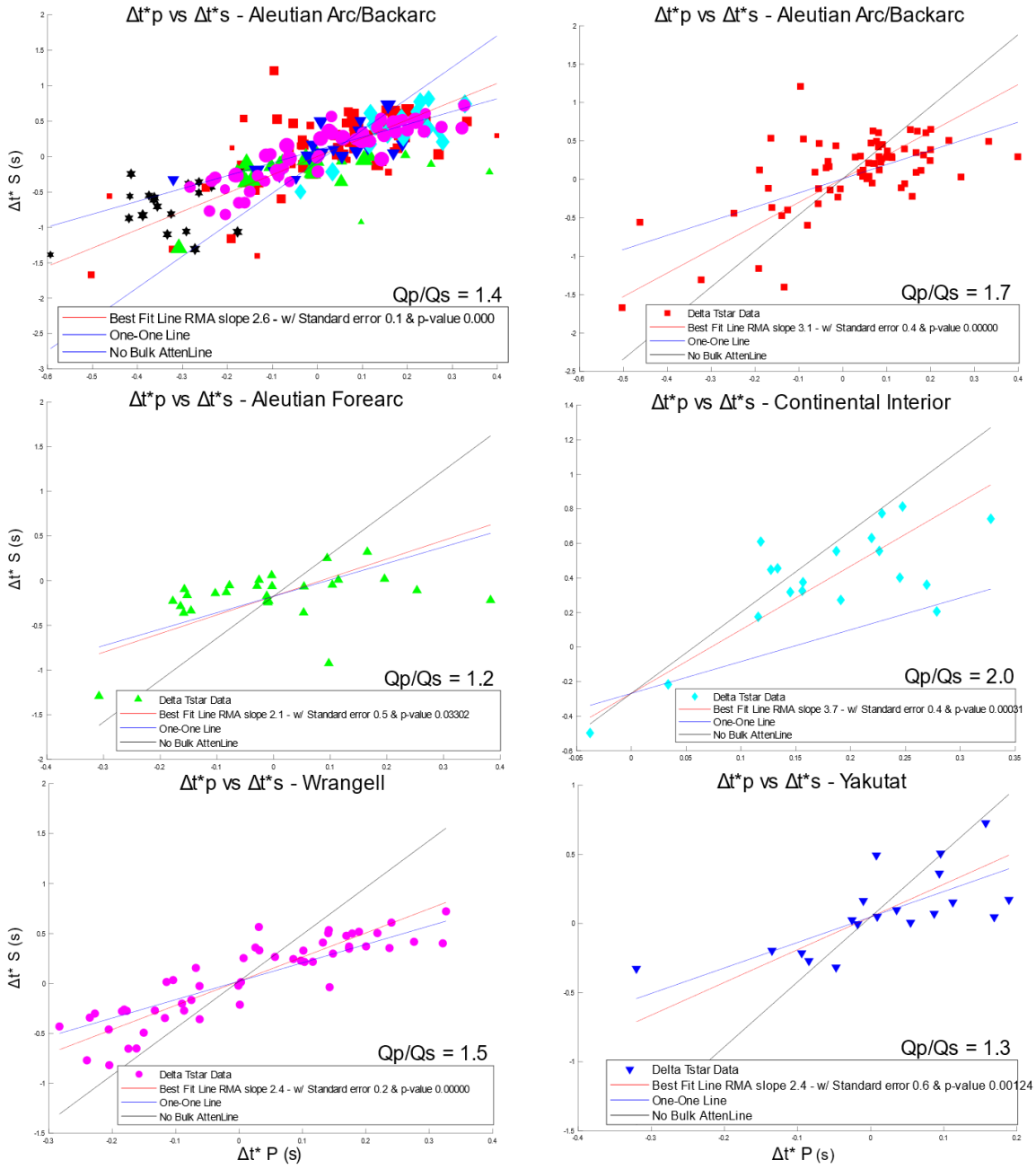

Figure 3.5 - Δt_S^* and Δt_P^* comparisons for each region with symbols following Figure 2.4. Regression is performed (Red line) and divided by a V_P/V_S ratio of 1.81. Region 2, Cook Inlet, is excluded because the best fit was not significant. The first panel includes all regions. The blue line indicates bulk and shear attenuation (Q_K& Q_μ) are approximately equal (Q_P/Q_S= 1). The black line indicates negligible bulk

attenuation is (Q_P/Q_S= 2.25). The calculated $Q_P/Q_S$for the top left is 1.4 ± 0.08, top right is 1.7 ± 0.2, middle left is 1.2 ± 0.3, middle right is 2.0 ± 0.2, bottom left is 1.5 ± 0.1, bottom right is 1.3 ± 0.3.

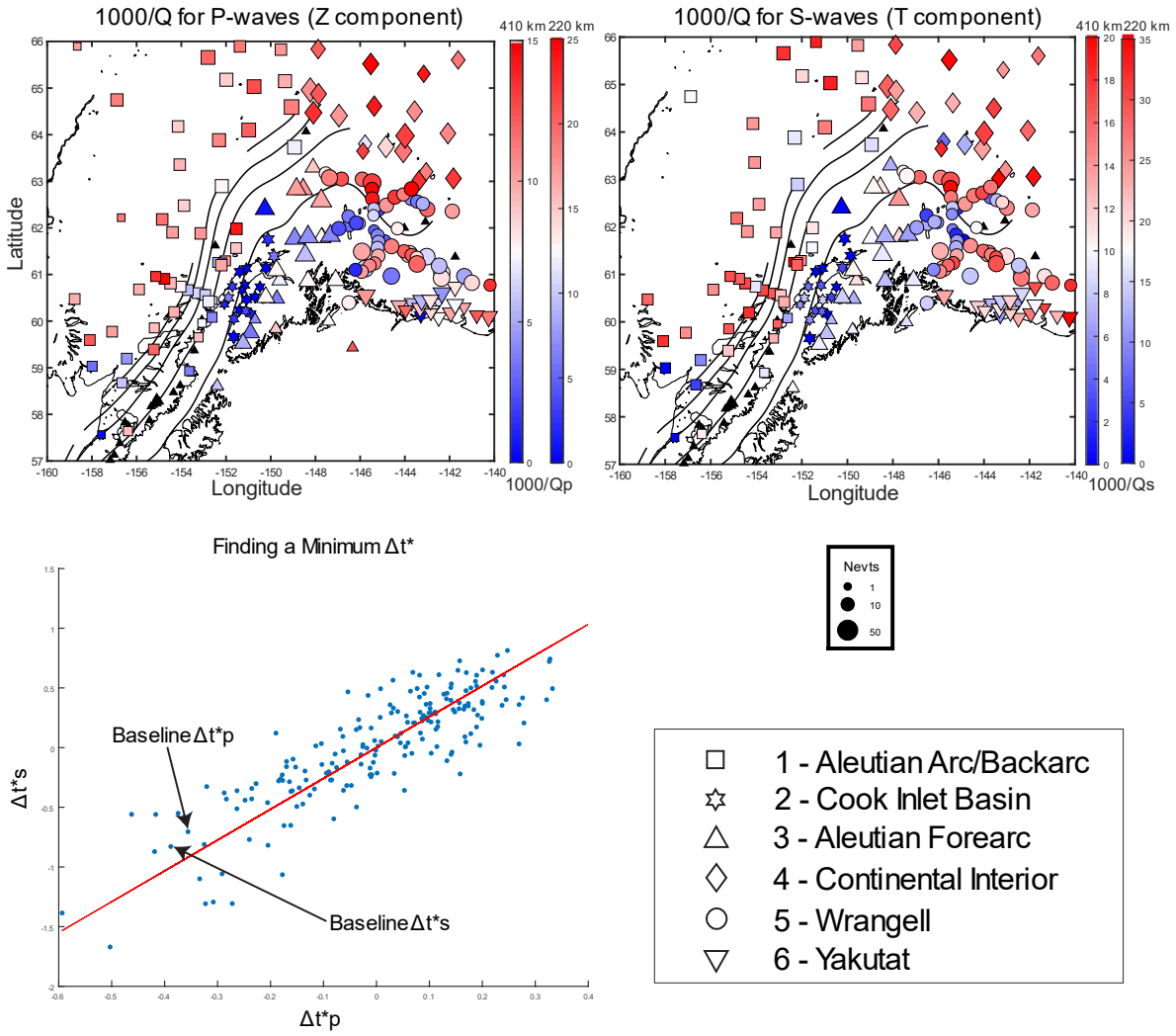

Figure 3.6 - Station averaged 1000/Q results plotted for both S and P phase results using two different length models, one with length scale of 220 km and velocity from the PREM (Dziewonsky and Anderson 1981) model and the other with length scale of 410 kms and velocities from the PREM. Fill, color, size and shape of stations follow the pattern described in Figure 2.4. Black lines indicate depth of subducting slab as indicated by WBZ seismicity at 20 km intervals. Red lines indicate major fault locations. Black triangles refer the location of volcanoes. Bottom panel shows the Δt* measurements chosen to establish a baseline, after trimming based on distance to RMS slope, the 10th lowest measurement is used.

Table 3.1 - Q_P/Q_S Estimates & $1000/Q_P$, $1000/Q_S$ Mean Regional Measurements

Q_P/Q_S Results	Region 1 Aleutian Arc/ Backarc	Region 2 Cook Inlet	Region 3 Aleutian Forearc	Region 4 Continental Interior	Region 5 Wrangell	Region 6 Yakutat	Alaska-Aleutian West Azimuth	Alaska-Aleutian East Azimuth
$\Delta t_P^*/\Delta t_S^*$	3.1	3.6	2.1	3.7	2.4	2.4	2.5	3.5
Q_P/Q_S	1.7	2.0	1.2	2.0	1.3	1.3	1.4	1.9
Standard Error - Q_P/Q_S	0.2	0.3	0.3	0.2	0.1	0.3	0.2	0.3
P-values - Q_P/Q_S	4.21E-09	0.185	0.033	3.11E-04	4.41E-18	1.20E-03	3.28E-04	0.009
Mean $1000/Q_S$ (1/s)| L = 410km, alpha = 0	12.1	1.7	8.6	15.1	11.3	11.8		
Mean $1000/Q_P$ (1/s)| L = 410km, alpha = 0	8.1	0.04	7.4	11.4	7.8	7.8		

REFERENCES

Abers, G. A., & Hacker, B. R. (2016). A MATLAB toolbox and E xcel workbook for calculating the densities, seismic wave speeds, and major element composition of minerals and rocks at pressure and temperature. Geochemistry, Geophysics, Geosystems, 17(2), 616-624.

Abers, G. A., Fischer, K. M., Hirth, G., Wiens, D. A., Plank, T., Holtzman, B. K., ... & Gazel, E. (2014). Reconciling mantle attenuation-temperature relationships from seismology, petrology, and laboratory measurements. Geochemistry, Geophysics, Geosystems, 15(9), 3521-3542.

Abers, G. A., Mann, M. E., Daly, K. A., Soto Castaneda, R., Christensen, D. H. (2019) Oblique subduction at the end of the Aleutian slab beneath the Wrangell Volcanic Field, Abstr. Amer. Geophys. Un. 2019 Fall Meeting, San Francisco, 9-13 Dec.

Abers, G. A., van Keken, P. E., Kneller, E. A., Ferris, A., & Stachnik, J. C. (2006). The thermal structure of subduction zones constrained by seismic imaging: Implications for slab dehydration and wedge flow. Earth and Planetary Science Letters, 241(3-4), 387-397.

Aki, K., & Richards, P. G. (1980). Quantitative seismology: theory and methods (p. 13). Freeman.

Allen, R. M., Nolet, G., Morgan, W. J., Vogfjörd, K., Bergsson, B. H., Erlendsson, P., ... & Ragnarsson, S. (1999). The thin hot plume beneath Iceland. Geophysical Journal International, 137(1), 51-63.

Anderson, D. L., & Hart, R. S. (1978). Q of the Earth. Journal of Geophysical Research: Solid Earth, 83(B12), 5869-5882.

Anderson, D. L., Ben-Menahem, A., & Archambeau, C. B. (1965). Attenuation of seismic energy in the upper mantle. Journal of Geophysical Research, 70(6), 1441-1448.

Anderson, O. L., Isaak, D., & Oda, H. (1992). High-temperature elastic constant data on minerals relevant to geophysics. Reviews of Geophysics, 30(1), 57-90.

Bohm, M., Haberland, C., & Asch, G. (2013). Imaging fluid-related subduction processes beneath Central Java (Indonesia) using seismic attenuation tomography. Tectonophysics, 590, 175-188.

Brocher, T. M., Fuis, G. S., Fisher, M. A., Plafker, G., Moses, M. J., Taber, J. J., & Christensen, N. I. (1994). Mapping the megathrust beneath the northern Gulf of Alaska using wide-angle seismic data. Journal of Geophysical Research: Solid Earth, 99(B6), 11663-11685.

Bruns, T. R. (1983). Model for the origin of the Yakutat block, an accreting terrane in the northern Gulf of Alaska. Geology, 11(12), 718-721.

Cafferky, S., & Schmandt, B. (2015). Teleseismic P wave spectra from USArray and implications for upper mantle attenuation and scattering. Geochemistry, Geophysics, Geosystems, 16(10), 3343-3361.

Chen, T., & Clayton, R. W. (2012). Structure of central and southern Mexico from velocity and attenuation tomography. Journal of Geophysical Research: Solid Earth, 117(B9).

Christeson, G. L., Gulick, S. P., van Avendonk, H. J., Worthington, L. L., Reece, R. S., & Pavlis, T. L. (2010). The Yakutat terrane: Dramatic change in crustal thickness across the Transition fault, Alaska. Geology, 38(10), 895-898.

Chung, W. Y., & Kanamori, H. (1980). Variation of seismic source parameters and stress drops within a descending slab and its implications in plate mechanics. Physics of the Earth and Planetary Interiors, 23(2), 134-159.

Cline II, C. J., Faul, U. H., David, E. C., Berry, A. J., & Jackson, I. (2018). Redox-influenced seismic properties of upper-mantle olivine. Nature, 555(7696), 355.

Colpron, M., Nelson, J. L., & Murphy, D. C. (2007). Northern Cordilleran terranes and their interactions through time. GSA today, 17(4/5), 4.

Cross, T. A., & PILGER Jr, R. H. (1982). Controls of subduction geometry, location of magmatic arcs, and tectonics of arc and back-arc regions. Geological Society of America Bulletin, 93(6), 545-562.

Dalton, C. A., & Göran, E. (2006). Constraints on global maps of phase velocity from surface-wave amplitudes. Geophysical Journal International, 167(2), 820-826.

Dalton, C. A., Ekström, G., & Dziewonski, A. M. (2009). Global seismological shear velocity and attenuation: A comparison with experimental observations. Earth and Planetary Science Letters, 284(1-2), 65-75.

Daly, K.A., G.A. Abers, S. Roecker, M.E. Mann and D.H. Christensen (2019), A Wadati-Benioff zone beneath the Wrangell Volcanic Field revealed by the WVLF broadband array, Abstr., Amer. Geophys. Un. 2019 Fall Meeting, San Francisco, 9-13 Dec.

Darot, M., & Gueguen, Y. (1981). High-temperature creep of forsterite single crystals. Journal of Geophysical Research: Solid Earth, 86(B7), 6219-6234.

De Siena, L., Del Pezzo, E., & Bianco, F. (2010). Seismic attenuation imaging of Campi Flegrei: Evidence of gas reservoirs, hydrothermal basins, and feeding systems. Journal of Geophysical Research: Solid Earth, 115(B9).

Dong, M. T., & Menke, W. H. (2017). Seismic high attenuation region observed beneath southern New England from teleseismic body wave spectra: Evidence for high asthenospheric temperature without melt. Geophysical Research Letters, 44(21), 10-958.

Durand, S., Chambat, F., Matas, J., & Ricard, Y. (2012). Constraining the kinetics of mantle phase changes with seismic data. Geophysical Journal International, 189(3), 1557-1564.

Dutta, U., Biswas, N. N., Adams, D. A., & Papageorgiou, A. (2004). Analysis of S-wave attenuation in South-Central Alaska. Bulletin of the Seismological Society of America, 94(1), 16-28.

Dziewonski, A. M., & Anderson, D. L. (1981). Preliminary reference Earth model. Physics of the earth and planetary interiors, 25(4), 297-356.

Dziewonski, A., Bloch, S., & Landisman, M. (1969). A technique for the analysis of transient seismic signals. Bulletin of the seismological Society of America, 59(1), 427-444.

Eberhart-Phillips, D., Christensen, D. H., Brocher, T. M., Hansen, R., Ruppert, N. A., Haeussler, P. J., & Abers, G. A. (2006). Imaging the transition from Aleutian subduction to Yakutat collision in central Alaska, with local earthquakes and active source data. Journal of Geophysical Research: Solid Earth, 111(B11).

Eberhart-Phillips, D., Reyners, M., Chadwick, M., & Stuart, G. (2008). Three-dimensional attenuation structure of the Hikurangi subduction zone in the central North Island, New Zealand. Geophysical Journal International, 174(1), 418-434.

Eilon, Z. C. (2016). New Constraints on Extensional Environments through Analysis of Teleseisms (Doctoral dissertation, Columbia University).

Eilon, Z. C., & Abers, G. A. (2017). High seismic attenuation at a mid-ocean ridge reveals the distribution of deep melt. Science advances, 3(5), e1602829.

Fang, Y., & Müller, G. (1991). Seismic-wave attenuation operators for arbitrary Q. Geophysical Journal International, 106(3), 703-707.

Faul, U. H., & Jackson, I. (2005). The seismological signature of temperature and grain size variations in the upper mantle. Earth and Planetary Science Letters, 234(1-2), 119-134.

Ferris, A., Abers, G. A., Christensen, D. H., & Veenstra, E. (2003). High resolution image of the subducted Pacific (?) plate beneath central Alaska, 50–150 km depth. Earth and Planetary Science Letters, 214(3-4), 575-588.

Fuis, G. S., Moore, T. E., Plafker, G., Brocher, T. M., Fisher, M. A., Mooney, W. D., ... & Levander, A. R. (2008). Trans-Alaska Crustal Transect and continental evolution involving subduction underplating and synchronous foreland thrusting. Geology, 36(3), 267-270.

Gebrande, H., Miller, H., & Einarsson, P. (1980). Seismic structure of Iceland along RRISP-Profile I. Journal of Geophysics, 47(1), 239-249.

Grove, T. L., Chatterjee, N., Parman, S. W., & Médard, E. (2006). The influence of H2O on mantle wedge melting. Earth and Planetary Science Letters, 249(1-2), 74-89.

Haberland, C., & Rietbrock, A. (2001). Attenuation tomography in the western central Andes: A detailed insight into the structure of a magmatic arc. Journal of Geophysical Research: Solid Earth, 106(B6), 11151-11167.

Haeussler, P. J., Freymueller, J. T., & Wesson, R. L. (2008). An overview of the neotectonics of interior Alaska: Far-field deformation from the Yakutat microplate collision. Active tectonics and seismic potential of Alaska, 179, 83-108.

Hales, A. L., & Doyle, H. A. (1967). P and S travel time anomalies and their interpretation. Geophysical Journal International, 13(4), 403-415.

Hammond, W. C., & Humphreys, E. D. (2000a). Upper mantle seismic wave attenuation: Effects of realistic partial melt distribution. Journal of Geophysical Research: Solid Earth, 105(B5), 10987-10999.

Hammond, W. C., and Humphreys, E. D. (2000b), Upper mantle seismic wave velocity: Effects of realistic partial melt geometries, J. Geophys. Res., 105(B5), 10975– 10986

Harris, F. J. (1978). On the use of windows for harmonic analysis with the discrete Fourier transform. Proceedings of the IEEE, vol. 66, no. 1, pp. 51-83

Hayes, G. P., Moore, G. L., Portner, D. E., Hearne, M., Flamme, H., Furtney, M., & Smoczyk, G. M. (2018). Slab2, a comprehensive subduction zone geometry model. Science, 362(6410), 58-61.

Holtzman, B. K. (2016). Questions on the existence, persistence, and mechanical effects of a very small melt fraction in the asthenosphere. Geochemistry, Geophysics, Geosystems, 17(2), 470-484.

IRIS - Incorporated Research Institutions. (n.d.). Transportable Array. Retrieved November 18, 2019, from http://www.usarray.org/researchers/obs/transportable.

Jackson, I., & Faul, U. H. (2010). Grainsize-sensitive viscoelastic relaxation in olivine: Towards a robust laboratory-based model for seismological application. Physics of the Earth and Planetary Interiors, 183(1-2), 151-163.

Jackson, I., Faul, U. H., Fitz Gerald, J. D., & Tan, B. H. (2004). Shear wave attenuation and dispersion in melt-bearing olivine polycrystals: 1. Specimen fabrication and mechanical testing. Journal of Geophysical Research: Solid Earth, 109(B6).

Jackson, I., Fitz Gerald, J. D., Faul, U. H., & Tan, B. H. (2002). Grain-size-sensitive seismic wave attenuation in polycrystalline olivine. Journal of Geophysical Research: Solid Earth, 107(B12), ECV-5.

Jackson, I., Paterson, M. S., & Fitz Gerald, J. D. (1992). Seismic wave dispersion and attenuation in Åheim dunite: an experimental study. Geophysical Journal International, 108(2), 517-534.

Jadamec, M. A., & Billen, M. I. (2010). Reconciling surface plate motions with rapid three-dimensional mantle flow around a slab edge. Nature, 465(7296), 338.

Jadamec, M. A., & Billen, M. I. (2012). The role of rheology and slab shape on rapid mantle flow: Three-dimensional numerical models of the Alaska slab edge. Journal of Geophysical Research: Solid Earth, 117(B2).

Jadamec, M. A., Billen, M. I., & Roeske, S. M. (2013). Three-dimensional numerical models of flat slab subduction and the Denali fault driving deformation in south-central Alaska. Earth and Planetary Science Letters, 376, 29-42.

Jiang, C., Schmandt, B., Ward, K. M., Lin, F. C., & Worthington, L. L. (2018). Upper Mantle Seismic Structure of Alaska From Rayleigh and S Wave Tomography. Geophysical Research Letters, 45(19), 10-350.

Karato, S. (1993). Importance of anelasticity in the interpretation of seismic tomography. Geophysical Research Letters, 20(15).

Karato, S. I. (2003). Mapping water content in upper mantle. Geophysical Monograph-American Geophysical Union, 138, 135-152.

Karato, S. I. (2006). Influence of hydrogen-related defects on the electrical conductivity and plastic deformation of mantle minerals: a critical review. GEOPHYSICAL MONOGRAPH-AMERICAN GEOPHYSICAL UNION, 168, 113.

Kim, Y., Abers, G. A., Li, J., Christensen, D., Calkins, J., & Rondenay, S. (2014). Alaska Megathrust 2: Imaging the megathrust zone and Yakutat/Pacific plate interface in the Alaska subduction zone. Journal of Geophysical Research: Solid Earth, 119(3), 1924-1941.

Koper, K. D., Wiens, D. A., Dorman, L., Hildebrand, J., & Webb, S. (1999). Constraints on the origin of slab and mantle wedge anomalies in Tonga from the ratio of S to P velocities. Journal of Geophysical Research: Solid Earth, 104(B7), 15089-15104.

Lekić, V., Matas, J., Panning, M., & Romanowicz, B. (2009). Measurement and implications of frequency dependence of attenuation. Earth and Planetary Science Letters, 282(1-4), 285-293.

Li, L. (2010). Bulk attenuation in the earth's mantle due to phase transitions. Physics of the Earth and Planetary Interiors, 183(3-4), 473-477.

Li, X., & Cormier, V. F. (2002). Frequency-dependent seismic attenuation in the inner core, 1. A viscoelastic interpretation. Journal of Geophysical Research: Solid Earth, 107(B12), ESE-13.

Liu, X., & Zhao, D. (2015). Seismic attenuation tomography of the Southwest Japan arc: new insight into subduction dynamics. Geophysical Journal International, 201(1), 135-156.

Liu, X., Zhao, D., & Li, S. (2014). Seismic attenuation tomography of the Northeast Japan arc: Insight into the 2011 Tohoku earthquake (Mw 9.0) and subduction dynamics. Journal of Geophysical Research: Solid Earth, 119(2), 1094-1118.

Mann, M.E., G.A. Abers, K.A. Daly and D.H. Christensen (2019), High-resolution receiver function imaging of crustal structure and subduction across Southcentral Alaska, Abstr., Amer. Geophys. Un. 2019 Fall Meeting, San Francisco, 9-13 Dec.

Martin-Short, R., Allen, R. M., & Bastow, I. D. (2016). Subduction geometry beneath south central Alaska and its relationship to volcanism. Geophysical Research Letters, 43(18), 9509-9517.

Martin-Short, R., Allen, R., Bastow, I. D., Porritt, R. W., & Miller, M. S. (2018). Seismic imaging of the Alaska subduction zone: Implications for slab geometry and volcanism. Geochemistry, Geophysics, Geosystems, 19(11), 4541-4560.

Mavko, G., and Nur, A. (1975), Melt squirt in the asthenosphere, J. Geophys. Res., 80(11), 1444–1448

McCarthy, C., Takei, Y., & Hiraga, T. (2011). Experimental study of attenuation and dispersion over a broad frequency range: 2. The universal scaling of polycrystalline materials. Journal of Geophysical Research: Solid Earth, 116(B9).

Minster, J. B., & Anderson, D. L. (1981). A model of dislocation-controlled rheology for the mantle. Philosophical Transactions of the Royal Society of London. Series A, Mathematical and Physical Sciences, 299(1449), 319-356.

Nakajima, J. (2014). Seismic attenuation beneath Kanto, Japan: evidence for high attenuation in the serpentinized subducting mantle. Earth, Planets and Space, 66(1), 12.

Nakajima, J., Matsuzawa, T., Hasegawa, A., & Zhao, D. (2001). Seismic imaging of arc magma and fluids under the central part of northeastern Japan. Tectonophysics, 341(1-4), 1-17.

Nokleberg, W. J. (2001). Phanerozoic tectonic evolution of the Circum-North Pacific (No. 1626). US Department of the Interior, US Geological Survey.

O'Driscoll, L. J., & Miller, M. S. (2015). Lithospheric discontinuity structure in Alaska, thickness variations determined by Sp receiver functions. Tectonics, 34(4), 694-714.

Page, R. A., Stephens, C. D., & Lahr, J. C. (1989). Seismicity of the Wrangell and Aleutian Wadati-Benioff zones and the North American plate along the Trans-Alaska crustal transect, Chugach Mountains and Copper River basin, southern Alaska. Journal of Geophysical Research: Solid Earth, 94(B11), 16059-16082.

Park, J., Lindberg, C. R., and Vernon, F. L. (1987), Multitaper spectral analysis of high-frequency seismograms, J. Geophys. Res., 92(B12), 12675– 12684

Pearce, J. A., Baker, P. E., Harvey, P. K., & Luff, I. W. (1995). Geochemical evidence for subduction fluxes, mantle melting and fractional crystallization beneath the South Sandwich island arc. Journal of Petrology, 36(4), 1073-1109.

Pérez-Campos, X., Kim, Y., Husker, A., Davis, P. M., Clayton, R. W., Iglesias, A., ... & Gurnis, M. (2008). Horizontal subduction and truncation of the Cocos Plate beneath central Mexico. Geophysical Research Letters, 35(18).

Plafker, G. (1987). Regional geology and petroleum potential of the northern Gulf of Alaska continental margin.

Plafker, G., & Berg, H. C. (1994). Overview of the geology and tectonic evolution of Alaska. The Geological Society of America, Boulder, Co, 989-1021.

Ponko, S. C., & Peacock, S. M. (1995). Thermal modeling of the southern Alaska subduction zone: insight into the petrology of the subducting slab and overlying mantle wedge. Journal of Geophysical Research: Solid Earth, 100(B11), 22117-22128.

Pozgay, S. H., Wiens, D. A., Conder, J. A., Shiobara, H., & Sugioka, H. (2009). Seismic attenuation tomography of the Mariana subduction system: Implications for thermal structure, volatile distribution, and slow spreading dynamics. Geochemistry, Geophysics, Geosystems, 10(4).

Preece, S. J., & Hart, W. K. (2004). Geochemical variations in the< 5 Ma Wrangell Volcanic Field, Alaska: implications for the magmatic and tectonic development of a complex continental arc system. Tectonophysics, 392(1-4), 165-191.

Ratchkovski, N. A., & Hansen, R. A. (2002). New constraints on tectonics of interior Alaska: Earthquake locations, source mechanisms, and stress regime. Bulletin of the Seismological Society of America, 92(3), 998-1014.

Ricard, Y., Matas, J., & Chambat, F. (2009). Seismic attenuation in a phase change coexistence loop. Physics of the Earth and Planetary Interiors, 176(1-2), 124-131.

Richards, P. G., & Menke, W. (1983). The apparent attenuation of a scattering medium. Bulletin of the Seismological Society of America, 73(4), 1005-1021.

Richter, D. H., Smith, J. G., Lanphere, M. A., Dalrymple, G. B., Reed, B. L., & Shew, N. (1990). Age and progression of volcanism, Wrangell volcanic field, Alaska. Bulletin of Volcanology, 53(1), 29-44.

Romanowicz, B. (1987). Multiplet-multiplet coupling due to lateral heterogeneity: asymptotic effects on the amplitude and frequency of the Earth's normal modes. Geophysical Journal International, 90(1), 75-100.

Romanowicz, B. (1995). A global tomographic model of shear attenuation in the upper mantle. Journal of Geophysical Research: Solid Earth, 100(B7), 12375-12394.

Romanowicz, B. (2002). Inversion of surface waves: a review. International Geophysics Series, 81(A), 149-174.

Romanowicz, B., & Mitchell, B. J. (2007). 1.21—Deep Earth structureQ of the Earth from crust to core. Treatise on geophysics, 731-774.

Rondenay, S., Montési, L. G., & Abers, G. A. (2010). New geophysical insight into the origin of the Denali volcanic gap. Geophysical Journal International, 182(2), 613-630.

Roth, E. G., Wiens, D. A., Dorman, L. M., Hildebrand, J., & Webb, S. C. (1999). Seismic attenuation tomography of the Tonga-Fiji region using phase pair methods. Journal of Geophysical Research: Solid Earth, 104(B3), 4795-4809.

Rychert, C. A., Fischer, K. M., Abers, G. A., Plank, T., Syracuse, E., Protti, J. M., ... & Strauch, W. (2008). Strong along-arc variations in attenuation in the mantle wedge beneath Costa Rica and Nicaragua. Geochemistry, Geophysics, Geosystems, 9(10).

Shellenbaum, D. P., & LJ Delaney, P. R. (2010). Top Mesozoic unconformity depth map of the Cook Inlet basin, Alaska.

Sipkin, S. A., & Jordan, T. H. (1979). Frequency dependence of QScS. Bulletin of the Seismological Society of America, 69(4), 1055-1079.

Smith, K., & Tape, C. (2019). Seismic noise in central Alaska and influences from rivers, wind, and sedimentary basins. Journal of Geophysical Research: Solid Earth, 124, 11678– 11704.

Smith, K., & Tape, C. (2019). Seismic response of Cook Inlet sedimentary basin, southern Alaska. Seismological Research Letters.

Stachnik, J. C., Abers, G. A., & Christensen, D. H. (2004). Seismic attenuation and mantle wedge temperatures in the Alaska subduction zone. Journal of Geophysical Research: Solid Earth, 109(B10).

Stein, S., & Wysession, M. (2003). An introduction to seismology. Earthquakes, and Earth.

Swenson, R. F. (1997). Introduction to Tertiary tectonics and sedimentation in the Cook Inlet basin.

Syracuse, E. M., van Keken, P. E., & Abers, G. A. (2010). The global range of subduction zone thermal models. Physics of the Earth and Planetary Interiors, 183(1-2), 73-90.

Takei, Y. (2000). Acoustic properties of partially molten media studied on a simple binary system with a controllable dihedral angle. Journal of Geophysical Research: Solid Earth, 105(B7), 16665-16682.

Tape, C., Christensen, D., Moore-Driskell, M. M., Sweet, J., & Smith, K. (2017). Southern Alaska Lithosphere and Mantle Observation Network (SALMON): A seismic experiment covering the active arc by road, boat, plane, and helicopter. Seismological Research Letters, 88(4), 1185-1202.

Thorkelson, D. J. (1996). Subduction of diverging plates and the principles of slab window formation. Tectonophysics, 255(1-2), 47-63.

Tilmann, F. J., McKenzie, D., & Priestley, K. F. (1998). P and S wave scattering from mantle plumes. Journal of Geophysical Research: Solid Earth, 103(B9), 21145-21163.

Trop, J. M., Ridgway, K. D., Glen, J. M. G., & O'Neill, J. M. (2007). Mesozoic and Cenozoic tectonic growth of southern Alaska: A sedimentary basin perspective. SPECIAL PAPERS-GEOLOGICAL SOCIETY OF AMERICA, 431, 55.

van Keken, P. E. (2003). The structure and dynamics of the mantle wedge. Earth and planetary science letters, 215(3-4), 323-338.

van Keken, P. E., Hacker, B. R., Syracuse, E. M., & Abers, G. A. (2011). Subduction factory: 4. Depth-dependent flux of H2O from subducting slabs worldwide. Journal of Geophysical Research: Solid Earth, 116(B1).

van Keken, P. E., Wada, I., Abers, G. A., Hacker, B. R., & Wang, K. (2018). Mafic High-Pressure Rocks Are Preferentially Exhumed From Warm Subduction Settings. Geochemistry, Geophysics, Geosystems, 19(9), 2934-2961.

VanDecar, J. C., & Crosson, R. S. (1990). Determination of teleseismic relative phase arrival times using multi-channel cross-correlation and least squares. Bulletin of the Seismological Society of America, 80(1), 150-169.

Wang, Y., & Tape, C. (2014). Seismic velocity structure and anisotropy of the Alaska subduction zone based on surface wave tomography. Journal of Geophysical Research: Solid Earth, 119(12), 8845-8865.

Ward, K. M. (2015). Ambient noise tomography across the southern Alaskan Cordillera. Geophysical Research Letters, 42(9), 3218-3227.

Wech, A. G. (2016). Extending Alaska's plate boundary: Tectonic tremor generated by Yakutat subduction. Geology, 44(7), 587-590.

Wei, S. S., & Wiens, D. A. (2018). P-wave attenuation structure of the Lau back-arc basin and implications for mantle wedge processes. Earth and Planetary Science Letters, 502, 187-199.

Wessel, P. (2016). Introduction to Statistics and Data Analysis [1.522]. Retrieved from http://www.soest.hawaii.edu/wessel/DA/index.html.

Wiens, D. A., Conder, J. A., & Faul, U. H. (2008). The seismic structure and dynamics of the mantle wedge. Annu. Rev. Earth Planet. Sci., 36, 421-455.

Worthington, L. L., Van Avendonk, H. J., Gulick, S. P., Christeson, G. L., & Pavlis, T. L. (2012). Crustal structure of the Yakutat terrane and the evolution of subduction and collision in southern Alaska. Journal of Geophysical Research: Solid Earth, 117(B1).

Yang, Y., Forsyth, D. W., & Weeraratne, D. S. (2007). Seismic attenuation near the East Pacific Rise and the origin of the low-velocity zone. Earth and Planetary Science Letters, 258(1-2), 260-268.

APPENDIX A

ATTENUATION & VELOCITY TOMOGRAPHY & RELATED CODE

Appendix A.1: Tomography

A preliminary attempt of tomography is applied here to the ΔT and Δt* results to obtain attenuation (Q_S, Q_P) and Velocity (V_S, V_P) at depth throughout the study region. The resulting tomography model is reported through horizontal and vertical cross sections (Figures A.1, A.2, A.3, A.4) which are still in a preliminary stage, but both align with recent velocity tomography results from previous studies and provide further context for the station-average values previously reported. The vertical slices show the model losing resolution at depth, but generally show strong alignment with the WBZ obtained from local seismicity depths.

The horizontal slices at 125 km depth are shown for all results to best interpret any upper mantle effects on attenuation and velocity. The dominant structure in these horizontal slices is the subducting slab beneath the Aleutian-Alaskan Arc, showing as a wide band of very low attenuation and fast velocities beneath the Aleutian arc/back-arc and Denali regions (3,5). For this structure, the extension of the subducting slab past the edge of the WBZ as previously discussed earlier in this study and in recent studies is clearly visible for the velocity tomography for both S and P phases, as well as for the S-phase attenuation and to a lesser extent the P-phase attenuation results. The attenuation tomography results much more clearly reflect of this extension of the subducting slab than the station-average values and helps clarify and further provide evidence for this interpretation. The vertical slices through cross sections A-B and C-D also show the alignment of the low attenuation and high velocity band with the local seismicity along the top of the subducting slab.

The S attenuation cross-section results for the C-D transect track less closely with the local seismicity, but this is likely related to the strong low attenuation signal that corresponds to location of the Wrangell subducting slab as interpreted in previous velocity studies and reflected in the velocity tomography here as a slight high velocity anomaly. This low attenuation anomaly is more accurately reflected in the E-F transect that follows closely with the cross-section in

Figure 2.9. The velocity tomography results here show a slight high velocity anomaly that corresponds to the local seismicity outlining the downgoing slab, and this anomaly is much greater in magnitude as a low attenuation anomaly for the S-phase attenuation cross section. These attenuation and velocity results at depth support our interpretation of attenuation as a useful tool to more cleanly image sub-surface effects.

This pattern is not as clearly reflected in the P attenuation, instead showing as a high attenuation anomaly. This result is difficult to interpret due to the combined influence of both bulk and shear modulus attenuation on P attenuation, but it is possible that a high V_P/V_S ratio could be responsible for the difference in phase results. Further work on constraining the V_P/V_S ratio of this region could be very useful in constraining these interpretations of high P and low S phase attenuation.

Appendix A.2: Location of Codes

All scripts are located at /home/ras656/MATLAB/AttenWork/TomoFiles/TOMO_R/Tomocode

Appendix A.3: Parameters

The parameters are loaded into the PARMS.m file and are listed below:

- datfile - **'Datatomo\data_dtstar_ST.dat'** - path to subdirectory with t* data.
- stafile - **'Datatomo\stations.dat'** - path to subdirectory with station info data.
- par(1).PS - **'1'** for P, **'2'** for S - body wave phase.
- par(1).t_ts - **'1'** for dT, **'2'** for dtstar - type of measurement to use for tomography.
- REBUILD - **'1'** to rebuild the model, '0' to skip - toggles rebuilding of the model.
- par.solver - **'bicg**' - choose between solving methods bicg and lsqr.
- par.synth_test - **'1'** or '0' - if 1 stops before performing actual inversion.
- par.crust_corr - '1' or **'0'** - if 1 performs crustal correction.
- par.wtdata - **'1'** or '0' - if 1 perform extra QC from wtdata.m function.
- par.squeeze - **'0'** - 0=no, 1=yes, 0<frac<1=force 2D for first frac of runs.
- par.zsqz - **'175'** - squeezing depth in kms.

- par.saveopt - **'1'** - save plots.
- par.age_smooth - **'0'** - option to smooth together based on age bins.
- par.damp - **'2'** - scaling for the whole damp matrix.
- par.damp_evt - **'1'** - absolute model damping to use for evt terms.
- par.damp_stn - **'1'** - absolute model damping to use for station terms.
- par.smooth - **'3'** - scaling for the whole smth mat. Baseline is 1.
- par.smth_zvh - **'0.3'** - Ratio of vertical to horizontal smoothing.
- par.scalereg - **'0'** - option to scale regularization matrices in make_F_f.
- par.plot_crutcorr - **'0'** - '1' to plot crustal correlation.
- par.plot_data - **'1'** - '1' to plot data.
- par.plot_inmodel - **'1'** - '1' to plot model mesh.
- par.plot_synout - **'1'** - '1' to plot synthetic output.
- par.plot_outputs - **'1'** - '1' to plot inversion output.
- par.plot_Zslices - **'1'** - '1' to plot vertical slices of model.
- par.plot_hitq - **'1'** - '1' to plot "hitmap".
- par.plot_raypath - **'0'** - '1' to plot raypaths.
- par.plot_everyNtime - **'1'** - '1' to plot model every N iterations.
- par.origin - **'[46.1914 -122.1956]'** - latitude longitude origin of model.
- par.map_proj - **'mercator'** - 'map projection chosen in mstructs.
- par.dh - **'10'** - horizontal spacing for nodes.
- par.dh_max - **'40'** - horizontal spacing max to which it scales at twice array aperture.
- par.dz - **'10'** - vertical spacing for nodes.
- par.dz_max - **'30'** - vertical spacing max to which it scales at twice array aperture.
- par.zmax - **'200'** - vertical spacing for nodes maximum vertical distance.
- par.zmin - **'15'** - top of model (above this must be accounted for by crust).
- par.kidd - **'5'** - along-ray segment lengths to calculate kernel at.
- par.Vavmod - **'1'** - sets starting model parameters 1=AK135, 2=Raj+Ferris, 3=STW105
- par.synth_noisy - **'1'** - '1' or '0'option to include realistic noice in synth data.
- sym.opt - **'checker'** - checker or custom synthetic pattern.
- sym.acx - **'[-580 -530 -470 -410 -310 -370 130]'** - vector of x cords for anomaly centres.

- sym.acy - **'[40 190 325 470 -240 -410 -50]'** - vector of y cords for anomaly centres.
- sym.acz - **'[70 70 70 70 70 70 180]'** - vector of z cords for anomaly centres.
- sym.awx - **'[80 60 80 80 80 60 100]'** - vector of z cords for anomaly centres.
- sym.awy - **'[140 60 80 80 80 60 100]'** - vector of z cords for anomaly centres.
- sym.awz - **'[90 90 90 90 90 90 300]'** - vector of z cords for anomaly centres.
- sym.adval - **'[5 5 5 5 5 5 -2]'** - vector of z cords for anomaly centres.
- sym.dval - **'400'** - in percent!
- sym.noise - **'0.05'** - standard of gaussian perturbations to data values (s)
- sym.estatic_sd - **'0.5'** - standard of gaussian perturbations input event terms (s)
- sym.sstatic_sd - **'0.5'** - standard of gaussian perturbations input station terms (s)

APPENDIX B

MAIN CODE/DATA LOCATION & WORKFLOW

Appendix B.1: Location of Codes

All scripts are located at /home/ras656/MATLAB_HomePC/, under the subdirectories as follows:

EilonCode/Matcode/	Travel time and attenuation calculation scripts
Figs/	Subdirectories for figure storage, by date creation.
DatalessDbs_AK2/	Antelope database headless files
Homog_DownData_AK_alph2/	Stores data in mid-processing format
Homog_DownData_AK_alph2_backup/	Backup directory
Homog_Results_AK_alph/	Stores result data formatted for use in figure making
Results_pairspecs/	Pairwise Atten calculations for each event, S & P
TerraneStaMap/	Subdirectory for map terrane data (slabs, faults etc.)

Tools/	Contains MATLAB tools for processing (mattaup)
UsefulScripts_Roque/	Additional MATLAB scripts for data processing

Appendix B.2: Parameters

Eilon/Matcode/

Contains the main computation and plotting codes written by Z. Eilon with alterations by R. Soto Castaneda and G. Abers. This directory also contains a README that provides some details regarding the usage of the scripts in this directory. The Master file in this directory contains the main data loading and processing scripts, in the appropriate order. Following that, the figure production scripts are listed, which can be used in any order. The scripts used in the production of the data & thesis figures are listed below, along with parameters & any additional notes.

/home/ras656/MATLAB_HomePC/Eilon/Matcode/evdata_1_DOWNLOAD_IRIS

Summary - First step of the data loading and pre-processing scripts. Downloads data from IRIS and stores it in mat files to build body wave dataset. Needs Antelope database software to access IRIS data effectively.

Parameters –

- wd - **'/home/ras656/MATLAB/AttenWork/EilonCode/Matcode'** - path to the working directory for Matcode subdirectory.
- datadir - **'/ld5/ras656_Atten/DatalessDbs_AK2'** - path to the subdirectory directory for the Antelope headless db files.
- resdir - **'/ld5/ras656_Atten/DownData_AK2_alph'** - path to the subdirectory for holding data during processing (not final format).
- dbnam - **'/Alaska_FullDB'** - name of Antelope database.
- dbdir - **'/ld5/ras656_Atten/DatalessDbs_AK2'** - same as datadir (for this script).
- datawind **- [-100 1700]** - time window of data obtained before and after event.
- phases - **'P,S,PKS,SKS'** - body wave phases to load.

- overwrite - **true** - sets whether to load in data that has been previously loaded.
- ifTest – **false** - when used with overwrite true, loads data in, but does not save (to test).
- unamepwd - **{'ras656@cornell.edu', 'wpmPh2hje6dg'}** - IRIS username and password for access to secure IRIS data.

Additional Notes – Should make sure that the most recent version of antelope is installed, and the path to it added to the top of the script (under the run tag). In addition, line 76 loads your origin IDs for the events you would like to obtain from the database origin file (so it only draws necessary events). This file must exist in the working directory or be replaced with one that does. The file used for this is AK_Orids_P_2.mat, located at the root of the working directory

/home/ras656/MATLAB_HomePC/Eilon/Matcode/evdata_2_ROTATE

Summary - Sifts through data and rotate each station's channel system if necessary.

Parameters –

- wd, datadir, resdir, dbnam, dbdir are all the same as evdata_1.

Additional Notes – Notes are the same as previous, regarding both the orid mat file and the Antelope version.

/home/ras656/MATLAB_HomePC/Eilon/Matcode/evdata_3_RMRESP_SACPZ

Summary - Removes instrument response from body wave data station channels. The instrument response files should be in SAC poles and zeros format with the naming style SAC_PZs_NWK_STA_CHAN where NWK is the 2-character network name, STA is the name of the station, and CHAN is the channel code.

Parameters –

- wd, datadir, resdir, dbnam, dbdir, overwrite - all the same as evdata_1.
- ifplot - **0** - to plot instrument response or not.
- respdir - **'/ld5/ras656_Atten/DatalessDbs_AK2'** - path to instrument response files.

Additional Notes – Notes are the same as previous, regarding both the orid mat file and the Antelope version.

/home/ras656/MATLAB_HomePC/Eilon/Matcode/evdata_4_ARRIVAL_STRUCT

Summary - Script cycles through data for each event and build data structures with all necessary data for each arrival of interest.

Parameters –

- wd, datadir, resdir, dbnam, dbdir, overwrite - all the same as evdata_1.
- phase - **'P'** and also **'S'** (2 different runs) - phase of data to create structure for.
- resamprate - **10** - new, common sample rate to downsample to.
- wind - **[-200 200]** - seconds before and after arrival to save data for.
- LatBound | LonBound - **[56 66]** | **[-159 -140]** - lat & lon limits for stations to use.

Additional Notes – Notes are the same as previous, regarding the orid mat file. Antelope can be used to get station details but is no longer necessary as there are alternative scripts to obtain the same information.

/home/ras656/MATLAB_HomePC/Eilon/Matcode/calc_1_Differential_TT

Summary - Script cycles through events and calculates differential travel time for all stations. It plots a record section that allows you to select a window of data to cross-correlate and calculate differential travel times, and then select a nominal phase onset time for the corrected arrivals.

Parameters –

- wd, resdir, dbnam, dbdir, overwrite - all the same as evdata_1.
- phase, resamprate – same as evdata_4.
- component - **'Z'** for P and **'T'** for S phases - instrument component to use (Z, R, T)

- filtfs - **1./[12 1]** for S & **1./[5 1]** for P - upper and lower frequency limits to analyze – format [f_low f_high].
- taperx - **0.2** - size of tukey taper window (from 0 to 1), relative to data window.
- datwind - **[-200, 200]** - size of data window loaded by evdata_4, before and after phase.
- prelimwind - **[-40 40]** - size of data window to show the user to pick cross-cor window.
- xcorlagmax - **6** - max allowed lag in seconds for use in xcortimes2.m script.
- acormin - **0.65** - minimum cross corr. max allowed, killing less correlated traces.
- ifsave - **true** - determines whether to save results (false to do test runs).
- manualkillstas - **{'M65A' 'CAST' 'FALS' 'KOTZ' 'SGA' 'TABL' 'RDDF' 'IVE' 'RND' 'FID' 'KTH' 'BWN' 'SII' 'CRQ' 'RAG' 'SUCK' 'BARN' 'CCB' 'RDWB' 'RDSO' 'RDJH' 'RDDF' 'IVE' 'ILW' 'ILSW' 'AUWS' 'AUSS' 'AUJA' 'AUQ' 'AUSB' 'AUL' 'AUCH' 'AU22' 'KAKN' 'KAI' 'KABU' 'GOAT' 'SWD' 'BRSE' 'SSN' 'BAGL' 'TGL' 'WHIP'}** - station names to pre-emptively remove due to low quality data.
- figdir - **'C:\Users\roque\Documents\MATLAB\Figs\'** - directory to store figures.
- scriptdir - **'C:\Users\roque\Documents\MATLAB\UsefulScripts_Roque'** - path to directory containing additional supplementary scripts.
- Taupdir - **'C:\Users\roque\Documents\MATLAB\Tools\mattaup'** - directory where mattaup is stored.

Additional Notes – Notes are the same as previous, regarding the orid mat file. Antelope is no longer used as the headless files are accessed via helper functions. Must add mattaup to javapath in order to use it for cross-correlation.

/home/ras656/MATLAB_HomePC/Eilon/Matcode/calc_2_SPECTRAL_RATIOS

Summary - Cycle through events and calculate tstar attenuation through the spectral ratios method for all stations. This is a pre-requisite to calculation with the comb of filters method and will calculate signal to noise ratio and frequency where the signal crosses pre-arrival noise.

Parameters –

- wd, resdir, dbnam, dbdir, overwrite, phase, component, resamprate, filtfs, taperx, datwind, ifsave, figdir, scriptdir, Taupdir - all the same as calc_1.
- specwind - **[-5 30]** - data window in seconds over which to obtain the spectral ratios.
- snrmin - **10** - minimum signal to noise ratio allowed.
- mavwind - **1** - length of moving average to smooth spectrum (1 for no smoothing).
- lofrq - **0.048** - lowermost frequency to fit.
- hifrq - **0.5005** - uppermost frequency to fit.
- ifplot - **false** - whether to show plots of spectra being calculated.

Additional Notes – Same as calc_1.

/home/ras656/MATLAB_HomePC/Eilon/Matcode/calc_3_COMBSPECTRA

Summary - Cycle through events and calculate attenuation for all stations by running a comb of filters over each pair of stations' traces to calculate t*.

Parameters –

- wd, resdir, dbnam, dbdir, overwrite, phase, component, resamprate, filtfs, taperx, datwind, ifsave, figdir, scriptdir, Taupdir, specwind, snrmin, ifplot - the same as calc_2.
- ifplotonly - **false** - only show plots, do not save the data calculated.
- parms.comb.Tmin - **0.5** - low end of the period of the data to analyze.
- parms.comb.Tmax - **20** - high end of the period of the data to analyze.
- parms.comb.Nwds - **30** - number of comb of filter windows to use.
- parms.comb.Tw_opt - **'scale'** - tag to set period windows for bandpass filter.
- parms.comb.npol - **4** - order of Butter filter to use.
- parms.wind.taperx - **0.1** - length of taper to add for filtering purposes.
- parms.qc.minacor - **0.5** - minimum cross correlation max allowed before trace is killed.
- parms.qc.maxphi - **5** - maximum phase difference allowed
- parms.inv.amp2phiwt - **5** - ratio of upweight of amplitude vs. phase spectra fit.
- parms.inv.fmin - **0.15** - minimum frequency to use in comb of filters

- parms.inv.fmax - **0.5** - nominal max frequency in comb, replaced by frequency where signal crosses prearrival noise.
- parms.inv.corr_c_skip - **true** - whether to correct for cycle skip
- parms.inv.ifwt - **true** - weight data by cross correlation value in fit of narrow-band filtered data between two stations.
- parms.inv.alpha - **0** - assumed frequency dependence of attenuation

Additional Notes – Same as calc_1.

/home/ras656/MATLAB_HomePC/Eilon/Matcode/calc_4_RESULTS_EXTRACT

Summary - Parses results into large nstas*nevts structures for use in figure creation.

Parameters –

- wd, resdir, dbnam, dbdir, phase, component, figdir, scriptdir, Taupdir - same as calc_1.
- mag_min - **5.7** - skips storing result data if the event below this magnitude.
- acor_min - **0.65** - skips storing result data if cross correlation max is below this value.
- snr_min - **10** - skips storing result data if the signal to noise ratio is below this value.

Additional Notes – Same as calc_1.

/home/ras656/MATLAB_HomePC/Eilon/Matcode/mkfig_CascMAP

Summary - Mapping script called within the other mapping scripts to produce the background coastlines, slab contour & major faults for the birds-eye-view maps of all other mapping scripts.

/home/ras656/MATLAB_HomePC/Eilon/Matcode/mkfig_Compare_dTdTstar

Summary - Plotting results around the focus regions of the Cook Inlet and Wrangell Volcanic Field, showing travel time and t* values with local seismicity cross-sections.

Parameters –

- wd, resdir, dbnam, dbdir, figdir, scriptdir - same as calc_1.
- ifTTime_Tstar_Compare - **true -** plots comparison of travel time to tstar.
- skippable - **true -** skips plots that are not the Cook Inlet cross-section plots.
- lonlims|latlims - **[-163 -140]** | **[56 66]**- longitude/latitude boundaries of the study area.
- LongBounds|LatBounds - **[-152 -149 -146]** | **[61 62.5 63.5]** - boundaries used for regionalization of the study area.
- CI_lonlims|CI_latlims - **[-156.25 -148.75]** | **[59.2 61.4]** - longitude and latitude boundaries for the Cook Inlet focus area.
- W_lonlims|W_latlims - **[-149 -142]** | **[60 63.5]** - longitude and latitude boundaries for the WVF focus area.
- CookE_p1|CookE_p2 & CookW_p1|CookW_p2 - **[-152.85, 58**] | **[-149.5, 61.5]** & **[-151.15, 62.4]** | **[-153.8, 58]** - Cook Inlet/Aleutian area boundaries.
- Slab_p1|Slab_p2 - **[-145, 57]** | **[-149.25, 66]** - WBZ derived edge of subducting slab.
- Yaklon|Yaklat - **-146** | **60.75** - Yakutat region boundaries.
- Den_p1|Den_p2 - **[-148.5, 64]** | **[-140, 62]** - Denali region boundaries.
- plotsize - **700** - size of the plots.
- scale - **60** - size of station markers.
- phases - **{'P','S'}** - body wave phase results to use.
- components - **{'Z','T'}** - instrument channel results to use.
- regs1, ... regs6, regsall - **'kh', 'rs', 'g^', 'bp', 'cd', 'mo', 'r'** - scatter plot data shape by regionalization.
- reg1, ... reg6 - **'h'**, **'s', '^'**, **'p'**, **'d'**, **'o'** - scatter plot data color by regionalization.
- modelChoice - **1** - when calculating Q from tstar, this chooses between thickness/seismic velocity models in mDepth, mVelp, mVels over which attenuation was accumulated.
- mDepth, mVelp, mVels - **[220, 410], [8.5589, 9.1851], [4.6439, 4.9617]** - Depth, P and S phase seismic velocities used in Q estimation.
- cmap - **blue2red** - colormap for use in non-regionalize figures.
- ifsave – **true -** whether to automatically save figures in figdir.

Additional Notes – This script contains a lot of preliminary figures which were often not used in the final version of the paper. To create only the cross-section figures that did appear in the paper, set skippable to true.

/home/ras656/MATLAB_HomePC/Eilon/Matcode/mkfig_DT_STAV_MAP

Summary - Script to plot mean differential travel time at each station. The mean value at each station is calculated after removal of event data greater than 3 standard deviations from the mean to remove outliers. In addition, this also plots individual measurements of differential travel time at each station as a function of back azimuth.

Parameters –

- wd, resdir, dbnam, dbdir, figdir, scriptdir, ifsave, lonlims/latlims, ifTTime_Tstar_Compare, LongBounds/LatBounds, CookE_p1,CookE_p2, CookW_p1, CookW_p2, Slab_p1, Slab_p2, Yaklon, Yaklat, Den_p1, Den_p2, plotsize, scale, components, phases, regs1, ... regs6, regsall, reg1, ... reg6, regall, cmap - same as mkfig_Compare_dTdTstar.
- method - **'comb'** - choose between comb of filters and spectral ratios results to plot.
- ifAzSep - **true -** whether to plot values regionalized by back-azimuth to event.
- Evnum_small - **true -** set to true if the number of events is too small for least squares regression method to work. Instead uses average after stripping outliers.
- StaNam, StaMidDex - **'MK10'**, **51** - station name & index for a station in the middle of study region.
- PlotNum - **0 -** should be initialized to 0, helps in counting figures when plotting.
- scaleL - **0.35** - length of line in back-azimuth spokes plot.
- tdftick **- 1** - tickmark spacing for color bar.
- minObs - **5 -** stations with less event data than this are not used in plots.
- keyloc, keysiz - **[-145.6,58.5], [2.5,1.9]** - mapkey location and size.

Additional Notes – None.

/home/ras656/MATLAB_HomePC/Eilon/Matcode/mkfig_DTSTAR_BAZ_MAP

Summary - Plots individual attenuation measurements of differential attenuation at each station as a function of back azimuth.

Parameters –

- wd, resdir, dbnam, dbdir, figdir, scriptdir, plotsize, scale, tdftick, keyloc, keysiz, components, phases, cmap - same as mkfig_Compare_dTdTstar.
- lonlims|latlims - **[-148 -141]** | **[60 63.5]** - latitude and longitude boundaries around a focus area (here WVF).

Additional Notes – None.

/home/ras656/MATLAB_HomePC/Eilon/Matcode/mkfig_DTSTAR_STAV_MAP

Summary - Script to plot mean differential attenuation at each station. The mean value at each station is calculated after removal of event data greater than 3 standard deviations from the mean to remove outliers.

Parameters –

- wd, resdir, dbnam, dbdir, figdir, scriptdir, ifsave, lonlims/latlims, LongBounds/LatBounds, CookE_p1,CookE_p2, CookW_p1, CookW_p2, Slab_p1, Slab_p2, Yaklon, Yaklat, Den_p1, Den_p2, plotsize, scale, components, phases, regs1, ... regs6, regsall, reg1, ... reg6, regall, cmap, modelChoice, mDepth, mVelp, mVels - same as mkfig_Compare_dTdTstar.
- Evnum_small, StaNam, StaMidDex, PlotNum, minObs, keyloc, keysiz, - same as mkfig_DT_STAV_MAP.
- Ifsave - **true** - whether to save output figures to figdir
- ifStaLook - **false** - this option looks at the station term values for a single station for all the available events with Non-NaN values and plots them.

- staRem, staRemLon, StaRemLat - **false, -145, 61** - whether to remove stations in a latlon bin, with top leftcorner at Lon,Lat and bin continues to the edge of study region.
- tstlimQpTop, tstlimQsTop - **[25 15]**, **[35 20]** - upper limit of colorbar for Qs/Qp, depending on model.

Additional Notes – None.

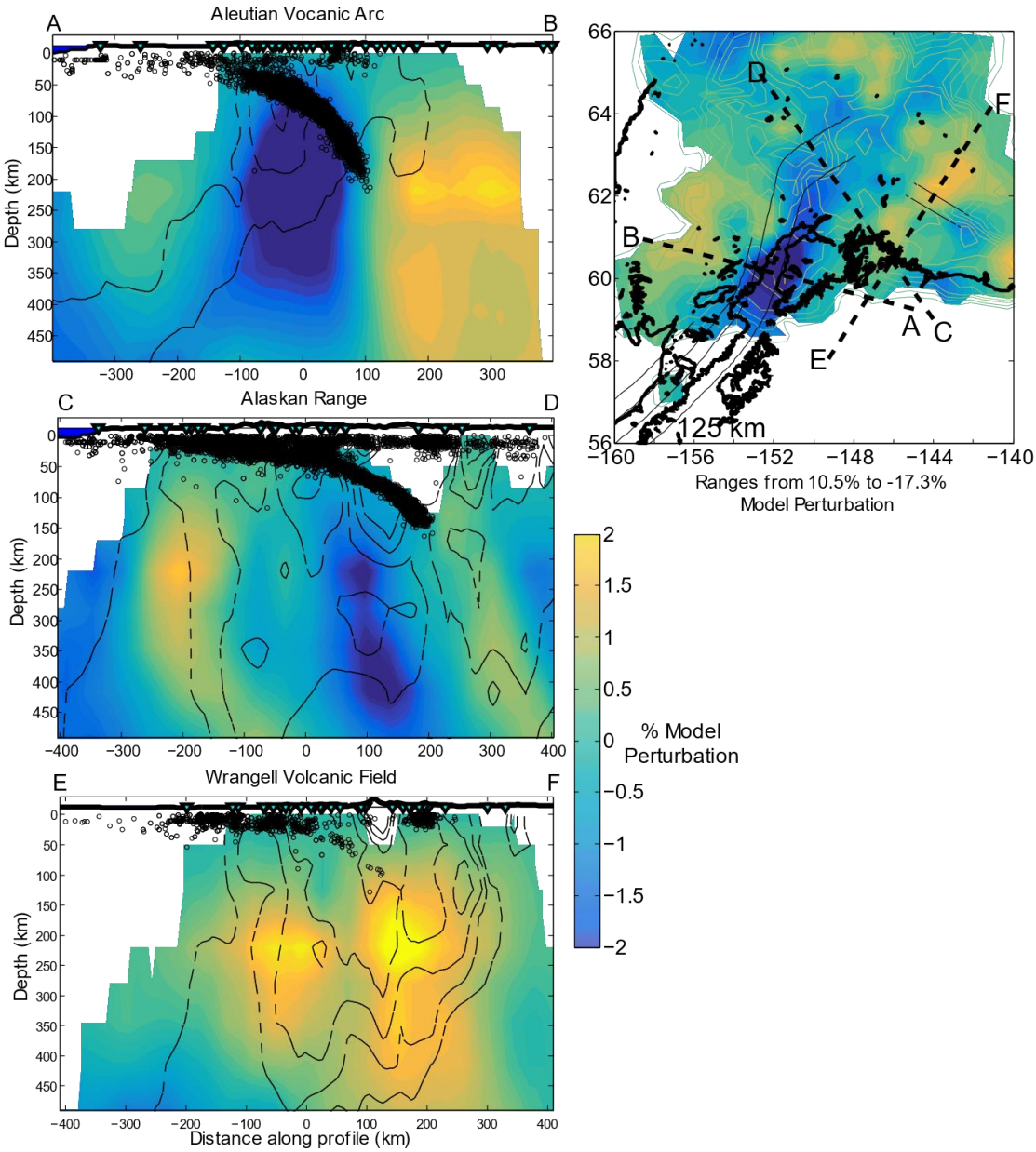

Figure A.1 - Vertical and Horizontal cross-sections of preliminary Q_P models based on Δt* data, with vertical cross sections cut perpendicular to slab geometry as derived from WBZ seismicity. In all panels, yellow indicates higher attenuation and blue indicates lower attenuation. Right panel is a horizontal slice of the model taken at 125 km depth, where thin black lines indicate the depth (50 km intervals) of the subducting plate plate (Plafker & Berg, 1994), Dashed black lines indicate cross section locations. Top, middle, and bottom panels are cross sections across the Aleutian volcanic arc, Alaskan Range, and WVF respectively. Results range from 10.5% to -17.3% model perturbation.

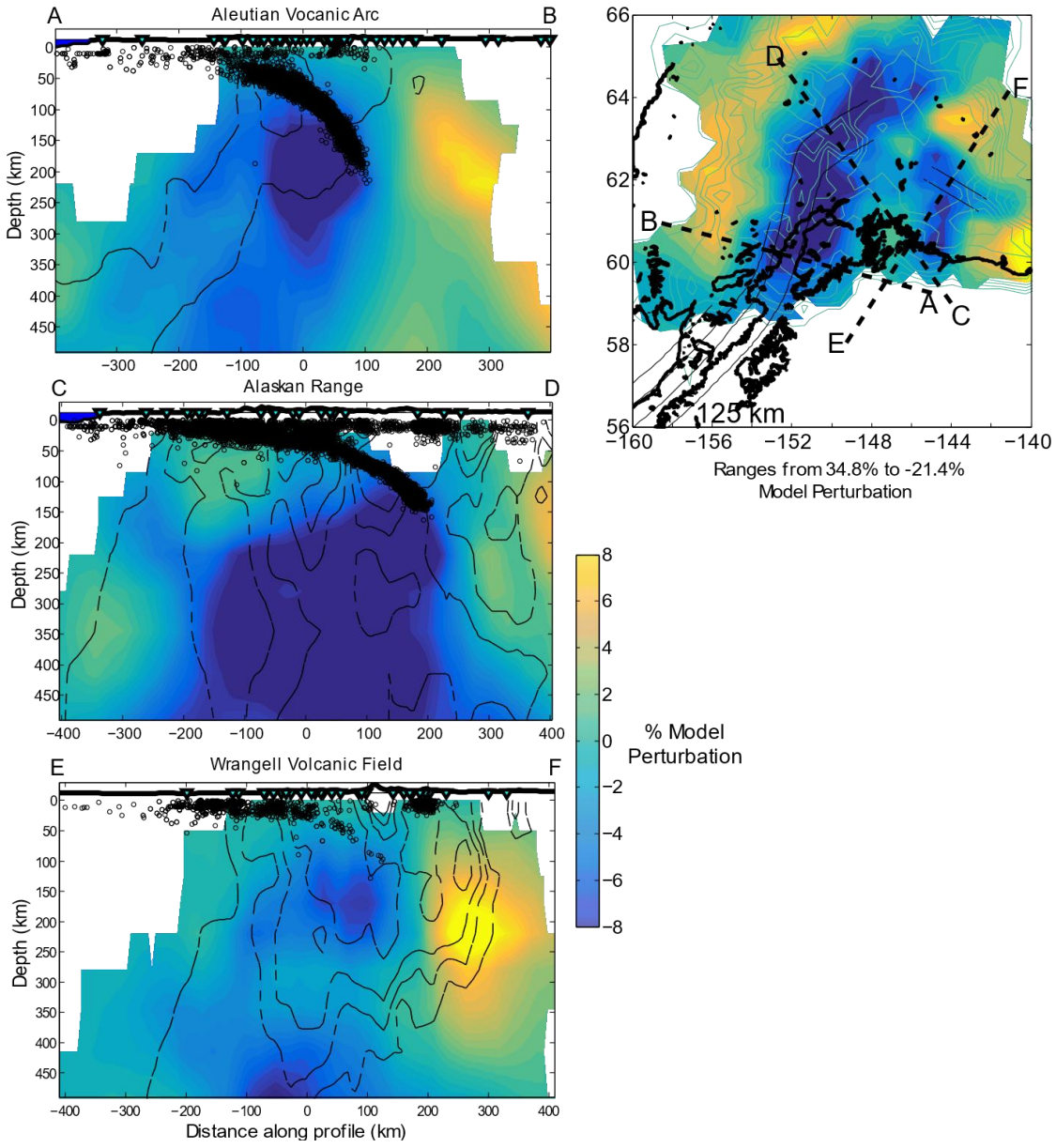

Figure A.2 - Vertical and Horizontal cross-sections of preliminary Q_S models based on Δt* data, with vertical cross sections cut perpendicular to slab geometry as derived from WBZ seismicity. In all panels, yellow indicates higher attenuation and blue indicates lower atttenuation. Right panel is a horizontal slice of the model taken at 125 km depth where thin black lines indicate the depth (50 km intervals) of the subducting plate (Plafker & Berg, 1994). Dashed black lines map cross section locations. Top, middle, and bottom panels are cross sections across the Aleutian volcanic arc, Alaskan Range, and WVF respectively. Results range from 34.8% to -21.4% model perturbation.

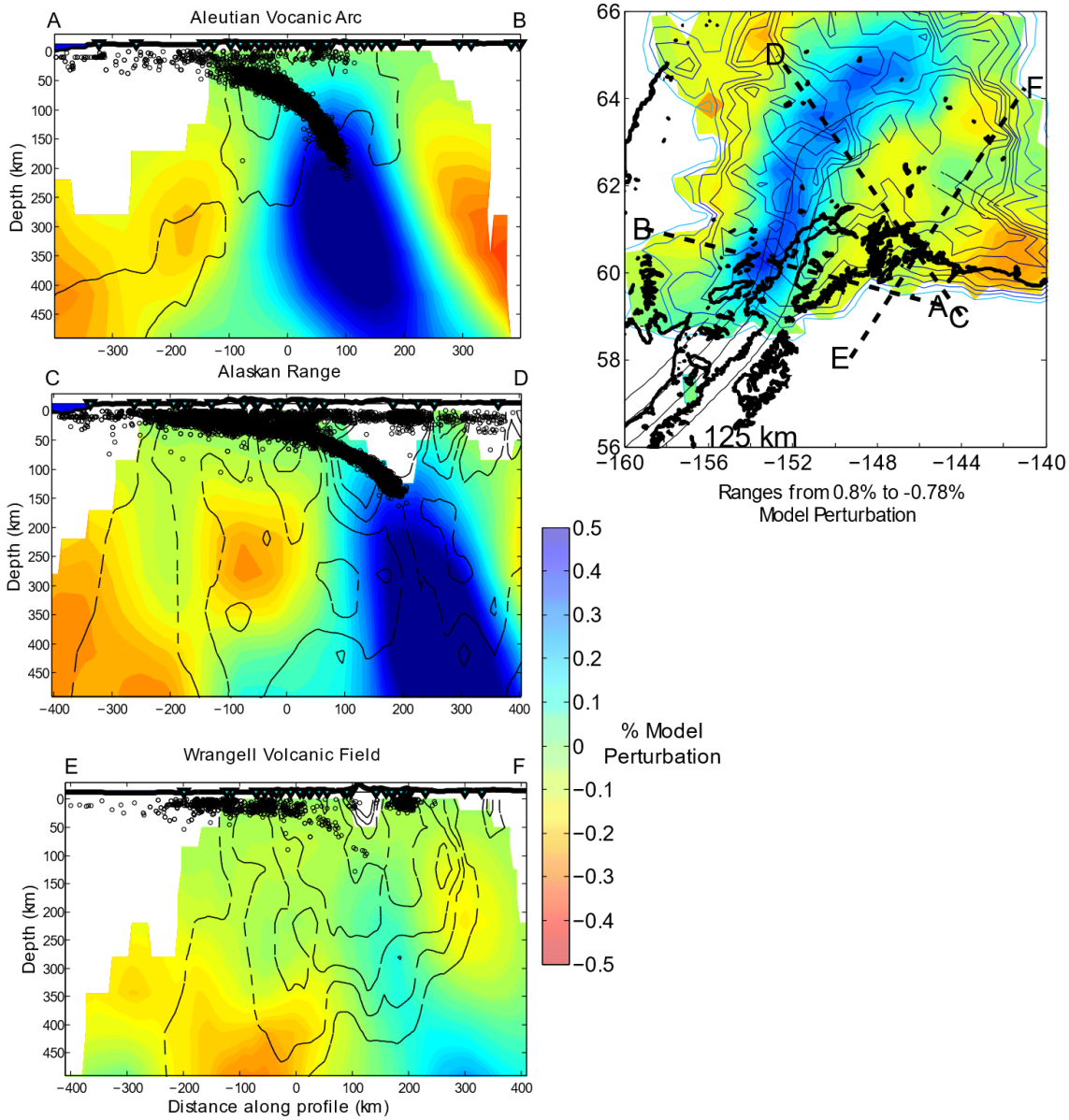

Figure A.3 - Vertical and Horizontal cross-sections of preliminary V_P models based on ΔT data, with vertical cross sections cut perpendicular to slab geometry as derived from WBZ seismicity. In all panels, warm colors indicate higher velocity and cool colors indicate lower velocity. Panel on the right is a horizontal slice of the model taken at 125 km depth where thick black lines indicate the coast, thin black lines indicate the depth (50 ft intervals) of the subducting plate. Dashed black lines map cross section locations. Top, middle, and bottom panels are cross sections across the Aleutian volcanic arc, Alaskan Range, and WVF respectively. Results range from 0.8% to -0.78% model perturbation.

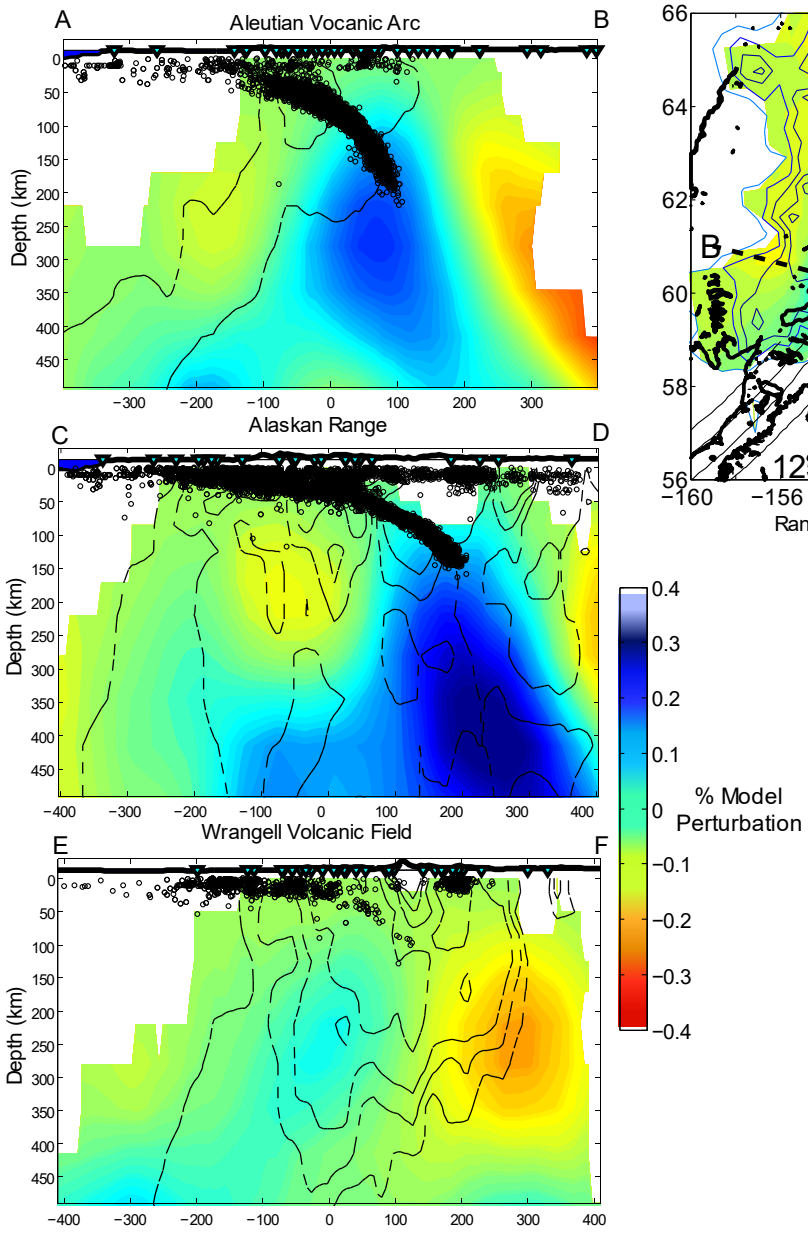

Figure A.4 - Vertical and Horizontal cross-sections of preliminary V_S models based on ΔT data, with vertical cross sections cut perpendicular to slab geometry as derived from WBZ seismicity. In all panels, warm colors indicate higher velocity and cool colors indicate lower velocity. Panel on the right is a horizontal slice of the model taken at 125 km depth where thin black lines indicate the depth (50 ft intervals) of the subducting plate. Dashed black lines map cross section locations. Top, middle, and bottom panels are cross sections across the Aleutian volcanic arc, Alaskan Range, and WVF respectively. Results range from 0.82% to -1.34% model perturbation.

Table A.1 - Station Information Table

Station Code	Latitude	Longitude	Network Code
'BAL'	61.0360	-142.3462	'AK'
'BARK'	60.4030	-142.4931	'AK'
'BERG'	60.3932	-143.7004	'AK'
'BGLC'	60.1205	-143.2841	'AK'
'BMR'	60.9677	-144.6051	'AK'
'BPAW'	64.0997	-150.9873	'AK'
'BRLK'	59.7511	-150.9063	'AK'
'CAPN'	60.7683	-151.1539	'AK'
'CHUM'	63.8827	-152.3152	'AK'
'CNP'	59.5251	-151.2373	'AK'
'CTG'	60.9649	-141.3401	'AK'
'CUT'	62.4058	-150.2625	'AK'
'CYK'	60.0823	-142.4872	'AK'
'DHY'	63.0753	-147.3759	'AK'
'DIV'	61.1292	-145.7749	'AK'
'DOT'	63.6482	-144.0697	'AK'
'EYAK'	60.5487	-145.7500	'AK'
'FIRE'	61.1426	-150.2164	'AK'
'GCSA'	64.7461	-156.8792	'AK'
'GHO'	61.7710	-148.9260	'AK'
'GLB'	61.4417	-143.8123	'AK'
'GLI'	60.8792	-147.0959	'AK'
'GRIN'	60.2805	-143.3210	'AK'
'GRNC'	60.7315	-141.7558	'AK'
'HDA'	64.4091	-146.9478	'AK'

'HIN'	60.3960	-146.5035	'AK'
'HMT'	60.3351	-144.2623	'AK'
'HOM'	59.6572	-151.6515	'AK'
'ISLE'	60.6024	-142.3406	'AK'
'KHIT'	60.4427	-143.2510	'AK'
'KIAG'	60.9231	-142.3605	'AK'
'KLU'	61.4924	-145.9227	'AK'
'KNK'	61.4131	-148.4585	'AK'
'KULT'	60.2474	-142.7234	'AK'
'LOGN'	60.8240	-141.0048	'AK'
'MCAR'	61.3836	-143.0240	'AK'
'MCK'	63.7318	-148.9373	'AK'
'MDM'	64.9602	-148.2319	'AK'
'MESA'	60.1785	-141.9505	'AK'
'MLY'	65.0304	-150.7442	'AK'
'NEA2'	64.5928	-149.0694	'AK'
'NICH'	60.2361	-143.9692	'AK'
'PAX'	62.9699	-145.4699	'AK'
'PIN'	60.0959	-140.2525	'AK'
'PPD'	65.5174	-145.5246	'AK'
'PPLA'	62.8962	-152.1894	'AK'
'PTPK'	61.1871	-142.4672	'AK'
'PWL'	60.8584	-148.3334	'AK'
'RC01'	61.0889	-149.7390	'AK'
'RIDG'	63.7399	-144.8462	'AK'
'RKAV'	60.2994	-141.3478	'AK'
'SAMH'	60.1294	-140.7828	'AK'
'SAW'	61.8070	-148.3316	'AK'
'SCM'	61.8320	-147.3290	'AK'
'SCRK'	63.9761	-143.9905	'AK'
'SKN'	61.9800	-151.5317	'AK'
'SLK'	60.5117	-150.2231	'AK'
'SSP'	60.1791	-142.8388	'AK'
'VRDI'	61.2275	-143.4545	'AK'
'WAT1'	62.8295	-148.5509	'AK'
'WAT2'	62.9628	-148.5855	'AK'
'WAT3'	62.6812	-148.5377	'AK'
'WAT5'	63.0624	-148.2286	'AK'
'WAT6'	62.5808	-147.7400	'AK'
'WAT7'	62.8331	-148.8476	'AK'
'WAX'	60.4480	-142.8529	'AK'
'WRH'	64.4715	-148.0916	'AK'
'YAH'	60.3583	-141.7510	'AK'

'WAT4'	62.8349	-147.9421	'AL'
'ANCK'	58.1981	-155.4961	'AV'
'ILS'	59.9570	-153.0703	'AV'
'NCT'	60.5621	-152.9293	'AV'
'RED'	60.4196	-152.7742	'AV'
'SPBG'	61.2591	-152.3722	'AV'
'SPCG'	61.2913	-152.0228	'AV'
'SPCN'	61.2244	-152.1854	'AV'
'SPCP'	61.2655	-152.1550	'AV'
'SPCR'	61.2003	-152.2091	'AV'
'SPNN'	61.3662	-152.7012	'AV'
'WACK'	61.9858	-144.3305	'AV'
'G18K'	65.8950	-158.6540	'TA'
'H18K'	65.1527	-158.3633	'TA'
'H19K'	65.5276	-156.4494	'TA'
'H20K'	65.4924	-154.8808	'TA'
'H21K'	65.6571	-152.8050	'TA'
'H22K'	65.8937	-151.3773	'TA'
'H23K'	65.8251	-149.5432	'TA'
'H24K'	65.8371	-147.8781	'TA'
'HARP'	62.3987	-145.1568	'TA'
'I20K'	64.7962	-154.4783	'TA'
'I21K'	65.1800	-151.9822	'TA'
'I23K'	65.1479	-149.3603	'TA'
'I26K'	65.3064	-143.1541	'TA'
'I27K'	65.6035	-141.6153	'TA'
'J18K'	63.4650	-156.7154	'TA'
'J19K'	63.9940	-155.6214	'TA'
'J20K'	64.1767	-154.1467	'TA'
'J25K'	64.6130	-145.3697	'TA'
'J26L'	64.5012	-143.5636	'TA'
'K17K'	62.7161	-158.3014	'TA'
'K20K'	63.3569	-154.0700	'TA'
'K24K'	63.8036	-145.7784	'TA'
'K27K'	64.0292	-142.0758	'TA'
'L17K'	62.1344	-158.2972	'TA'
'L18K'	62.2195	-156.6886	'TA'
'L19K'	62.1816	-154.8543	'TA'
'L20K'	62.4787	-153.8798	'TA'
'L26K'	63.0254	-143.3478	'TA'
'L27K'	63.0618	-141.8275	'TA'
'M16K'	61.0224	-158.9593	'TA'
'M17K'	61.4009	-157.4375	'TA'

'M18K'	61.4907	-155.8242	'TA'
'M19K'	61.9037	-154.3915	'TA'
'M20K'	61.8823	-153.1318	'TA'
'M22K'	61.7531	-150.1205	'TA'
'M23K'	61.7929	-147.7262	'TA'
'M24K'	62.1067	-146.1750	'TA'
'M26K'	62.4013	-142.9963	'TA'
'M27K'	62.3579	-141.8780	'TA'
'N16K'	60.4742	-158.7690	'TA'
'N17K'	60.5269	-157.1867	'TA'
'N18K'	60.6801	-155.8897	'TA'
'N19K'	60.8132	-154.4838	'TA'
'N20K'	61.2001	-152.2089	'TA'
'N25K'	61.6061	-144.5982	'TA'
'O16K'	59.5938	-158.0932	'TA'
'O17K'	59.7733	-157.0946	'TA'
'O18K'	59.8542	-155.2080	'TA'
'O19K'	60.1952	-154.3201	'TA'
'O20K'	60.0815	-152.6240	'TA'
'O22K'	60.4814	-149.7241	'TA'
'O28M'	60.7718	-140.1906	'TA'
'P16K'	59.0314	-157.9906	'TA'
'P17K'	59.1953	-156.4394	'TA'
'P18K'	59.3922	-155.2292	'TA'
'P19K'	59.6524	-153.2319	'TA'
'P23K'	59.9979	-147.4031	'TA'
'Q16K'	58.6774	-156.6556	'TA'
'Q19K'	58.9287	-153.6446	'TA'
'Q20K'	58.6097	-152.3942	'TA'
'Q23K'	59.4296	-146.3399	'TA'
'R16K'	57.5673	-157.5742	'TA'
'R17K'	57.6397	-156.3872	'TA'
'R18K'	57.5665	-154.4524	'TA'
'TCOL'	64.8735	-147.8618	'TA'
'DEN1'	63.0466	-145.9084	'YG'
'DEN3'	63.0487	-146.8329	'YG'
'DEN4'	63.1710	-147.5435	'YG'
'DEN5'	63.2970	-148.1052	'YG'
'GLN1'	62.0962	-146.0436	'YG'
'GLN2'	62.0601	-146.4865	'YG'
'GLN3'	61.9872	-146.9537	'YG'
'GLN4'	61.7895	-147.6796	'YG'
'LKLO'	62.2474	-146.5255	'YG'

'MCR1'	61.7157	-144.8952	'YG'
'MCR2'	61.4991	-144.0393	'YG'
'MCR3'	61.4176	-143.6980	'YG'
'MCR4'	61.3629	-143.4667	'YG'
'NEB1'	62.6228	-143.7135	'YG'
'NEB2'	62.5654	-143.4492	'YG'
'NEB3'	62.5184	-143.1996	'YG'
'RH01'	63.6483	-145.8756	'YG'
'RH03'	62.8334	-145.4710	'YG'
'RH04'	62.6286	-145.4562	'YG'
'RH05'	62.4106	-145.3882	'YG'
'RH06'	62.2697	-145.4051	'YG'
'RH07'	61.9500	-145.3817	'YG'
'RH08'	61.8370	-145.2216	'YG'
'RH09'	61.7009	-145.1846	'YG'
'RH10'	61.5732	-145.2256	'YG'
'RH11'	61.4014	-145.1947	'YG'
'RH12'	61.2398	-145.3532	'YG'
'RH13'	61.1934	-145.5741	'YG'
'RH14'	61.0617	-145.9367	'YG'
'RH15'	61.1012	-146.2122	'YG'
'TOK1'	62.4839	-144.8279	'YG'
'TOK2'	62.6620	-144.4506	'YG'
'TOK3'	62.7187	-144.0694	'YG'
'TOK4'	62.8391	-143.7069	'YG'
'TOK5'	63.2061	-143.0471	'YG'
'BING'	60.5169	-150.7037	'ZE'
'BULG'	61.1267	-151.0912	'ZE'
'CLAM'	60.2376	-151.3934	'ZE'
'CONG'	61.0594	-151.3870	'ZE'
'GOOS'	61.3936	-149.8535	'ZE'
'HARR'	60.3969	-152.2424	'ZE'
'HLC1'	60.4430	-152.5685	'ZE'
'HLC2'	60.5756	-153.0827	'ZE'
'HLC3'	60.6012	-153.2768	'ZE'
'HLC4'	60.6658	-153.7100	'ZE'
'HLC5'	60.7407	-154.0333	'ZE'
'HOLG'	59.8351	-149.7696	'ZE'
'HOPE'	60.8733	-149.5967	'ZE'
'JOES'	61.3955	-151.4943	'ZE'
'JUDD'	61.5668	-151.5481	'ZE'
'KALN'	60.5006	-151.8871	'ZE'
'KALS'	60.3604	-152.0732	'ZE'

'LTUW'	60.0346	-150.7006	'ZE'
'LTUX'	60.1595	-150.8850	'ZE'
'LTUY'	60.2216	-151.1153	'ZE'
'MPEN'	60.7351	-150.4819	'ZE'
'NNIL'	60.0473	-151.6491	'ZE'
'NSKI'	60.6622	-151.2772	'ZE'
'SALA'	60.7419	-151.7145	'ZE'
'SOLD'	60.4642	-151.0817	'ZE'
'WFLS'	60.9075	-154.7562	'ZE'
'WFLW'	60.9573	-155.1440	'ZE'

Table A.2 - Δt^* & ΔT Results by Station – Frequency Dependence $\alpha = 0$

Station Code	ΔT_S (s)	ΔT_S - STD	ΔT_P	ΔT_P - STD	Δt^*_S (s)	Δt^*_S - STD	Δt^*_P (s)	Δt^*_P - STD	# of Events	ΔT_S - err	ΔT_P - err	Δt^*_S - err	Δt^*_P - err
'ANCK'	0.28	0.08	0.18	0.04	-0.67	0.39	-0.51	0.12	2	0.06	0.03	0.28	0.08
'BAL'	1.16	0.13	0.42	0.05	0.17	0.51	-0.02	0.12	32	0.02	0.01	0.09	0.02
'BARK'	1.55	0.09	0.64	0.04	-0.40	0.42	-0.08	0.11	5	0.04	0.02	0.19	0.05
'BERG'	1.21	0.13	0.38	0.05	-0.33	0.59	-0.13	0.10	12	0.04	0.02	0.17	0.03
'BGLC'	2.16	0.14	0.86	0.14	-0.40	0.96	-0.28	0.15	8	0.05	0.05	0.34	0.05
'BING'	-0.08	0.09	-0.02	0.05	-0.63	0.78	-0.36	0.15	9	0.03	0.02	0.26	0.05
'BMR'	0.73	0.11	0.19	0.04	-0.36	0.43	-0.23	0.11	34	0.02	0.01	0.07	0.02
'BPAW'	-0.87	0.13	-0.29	0.07	0.23	0.59	0.14	0.10	44	0.02	0.01	0.09	0.02
'BRLK'	-1.36	0.19	-0.43	0.10	-0.29	0.82	-0.08	0.11	22	0.04	0.02	0.17	0.02
'BULG'	0.49	0.13	0.39	0.10	-0.85	0.57	-0.40	0.14	10	0.04	0.03	0.18	0.04
'CAPN'	0.94	0.43	0.68	0.06	-0.57	0.67	-0.39	0.19	8	0.15	0.02	0.24	0.07
'CHUM'	-0.50	0.15	-0.05	0.05	-0.21	0.59	0.10	0.10	38	0.02	0.01	0.10	0.02
'CLAM'	0.04	0.11	0.09	0.06	-0.58	0.56	-0.23	0.14	9	0.04	0.02	0.19	0.05
'CNP'	-0.73	0.11	-0.15	0.08	-0.14	0.62	-0.11	0.12	22	0.02	0.02	0.13	0.03
'CONG'	-0.19	0.12	0.05	0.16	-1.10	0.80	-0.35	0.16	10	0.04	0.05	0.25	0.05
'CTG'	1.78	0.11	0.67	0.04	-0.03	0.63	-0.13	0.11	23	0.02	0.01	0.13	0.02
'CUT'	-1.95	0.26	-0.63	0.06	-1.35	0.59	-0.34	0.13	33	0.05	0.01	0.10	0.02
'CYK'	1.65	0.21	0.69	0.11	0.12	0.73	-0.03	0.12	17	0.05	0.03	0.18	0.03
'DEN1'	-0.70	0.13	-0.33	0.06	0.21	0.51	0.09	0.11	21	0.03	0.01	0.11	0.02
'DEN3'	-1.09	0.09	-0.19	0.12	0.29	0.42	0.17	0.13	17	0.02	0.03	0.10	0.03
'DEN4'	-1.29	0.09	-0.11	0.04	-0.10	0.47	-0.05	0.11	12	0.03	0.01	0.14	0.03
'DEN5'	-1.70	0.10	-0.34	0.04	-0.40	0.59	-0.02	0.11	17	0.03	0.01	0.14	0.03
'DHY'	-1.08	0.12	-0.17	0.07	-0.14	0.49	0.11	0.12	31	0.02	0.01	0.09	0.02
'DIV'	0.46	0.09	0.15	0.04	0.14	0.40	-0.07	0.10	35	0.02	0.01	0.07	0.02
'DOT'	0.17	0.16	-0.07	0.05	0.15	0.49	0.10	0.11	41	0.03	0.01	0.08	0.02
'EYAK'	1.00	0.12	0.24	0.06	0.14	0.52	0.10	0.11	30	0.02	0.01	0.09	0.02

'FIRE'	0.13	0.13	0.18	0.04	-0.62	0.77	-0.34	0.17	13	0.04	0.01	0.21	0.05
'G18K'	-0.08	0.13	0.19	0.03	0.67	0.47	0.18	0.09	1	0.13	0.03	0.47	0.09
'GCSA'	-0.38	0.15	-0.11	0.09	-0.05	0.62	0.13	0.12	24	0.03	0.02	0.13	0.03
'GHO'	-0.92	0.15	-0.16	0.05	-0.15	0.58	-0.19	0.11	37	0.03	0.01	0.10	0.02
'GLB'	0.77	0.12	0.33	0.05	0.18	0.47	0.02	0.10	39	0.02	0.01	0.07	0.02
'GLI'	-0.23	0.11	-0.36	0.06	-0.17	0.46	-0.01	0.12	28	0.02	0.01	0.09	0.02
'GLN1'	1.16	0.20	0.41	0.13	-0.44	0.59	-0.15	0.14	12	0.06	0.04	0.17	0.04
'GLN2'	0.73	0.12	0.21	0.13	-0.38	0.63	-0.25	0.15	13	0.03	0.04	0.18	0.04
'GLN3'	0.01	0.11	0.08	0.05	-0.44	0.49	-0.24	0.10	19	0.03	0.01	0.11	0.02
'GLN4'	-0.66	0.13	-0.22	0.06	-0.17	0.47	-0.08	0.12	18	0.03	0.01	0.11	0.03
'GOOS'	-0.87	0.22	-0.24	0.04	-1.07	0.68	-0.17	0.12	14	0.06	0.01	0.18	0.03
'GRIN'	1.96	0.41	0.78	0.09	0.01	0.69	0.03	0.13	17	0.10	0.02	0.17	0.03
'GRNC'	1.67	0.29	0.58	0.05	0.45	0.65	-0.02	0.11	17	0.07	0.01	0.16	0.03
'H18K'	-0.54	0.30	0.14	0.04	0.71	0.65	0.37	0.06	1	0.30	0.04	0.65	0.06
'H19K'	-2.91	0.11	-0.66	0.03	-0.31	0.84	-0.09	0.09	2	0.08	0.02	0.59	0.07
'H20K'	-3.19	0.14	-0.71	0.03	0.33	0.80	0.18	0.13	1	0.14	0.03	0.80	0.13
'H21K'	0.02	0.15	0.04	0.06	0.48	0.59	0.13	0.11	41	0.02	0.01	0.09	0.02
'H22K'	0.45	0.12	0.19	0.06	0.60	0.57	0.13	0.14	17	0.03	0.01	0.14	0.03
'H23K'	0.42	0.22	0.21	0.05	0.11	0.58	0.07	0.11	24	0.04	0.01	0.12	0.02
'H24K'	0.23	0.24	0.12	0.08	0.42	0.52	0.06	0.10	21	0.05	0.02	0.11	0.02
'HARP'	0.63	0.14	0.27	0.14	-0.80	0.55	-0.23	0.15	13	0.04	0.04	0.15	0.04
'HARR'	-1.17	0.26	-0.32	0.18	-1.40	0.76	-0.58	0.11	3	0.15	0.11	0.44	0.07
'HDA'	-1.64	0.13	-0.61	0.05	0.10	0.62	0.06	0.11	36	0.02	0.01	0.10	0.02
'HIN'	0.81	0.09	0.04	0.04	-0.22	0.55	-0.01	0.10	18	0.02	0.01	0.13	0.02
'HLC1'	-2.27	0.33	-0.88	0.04	0.16	0.54	0.04	0.11	4	0.16	0.02	0.27	0.06
'HLC2'	-0.72	0.11	-0.35	0.07	0.54	0.48	0.04	0.12	13	0.03	0.02	0.13	0.03
'HLC3'	-0.53	0.10	-0.38	0.05	0.42	0.66	-0.03	0.11	15	0.03	0.01	0.17	0.03
'HLC4'	-0.31	0.10	-0.12	0.05	0.45	0.55	-0.11	0.12	16	0.02	0.01	0.14	0.03
'HLC5'	-0.15	0.14	-0.20	0.05	-0.16	0.66	0.00	0.12	16	0.03	0.01	0.17	0.03
'HMT'	1.67	0.18	0.40	0.05	0.03	0.61	0.07	0.12	18	0.04	0.01	0.14	0.03
'HOLG'	-0.95	0.30	-0.36	0.05	-0.11	0.59	0.09	0.10	7	0.11	0.02	0.22	0.04
'HOM'	-0.18	0.17	-0.03	0.09	-0.90	0.66	-0.41	0.14	17	0.04	0.02	0.16	0.03
'HOPE'	-0.97	0.13	-0.36	0.04	0.01	0.59	0.02	0.12	13	0.04	0.01	0.16	0.03
'I20K'	-3.56	0.87	-0.83	0.03	-1.35	1.09	-0.30	0.09	1	0.87	0.03	1.09	0.09
'I21K'	-0.10	0.26	0.06	0.07	0.02	0.57	0.00	0.11	35	0.04	0.01	0.10	0.02
'I23K'	-0.46	0.19	-0.03	0.05	0.01	0.65	0.02	0.10	29	0.04	0.01	0.12	0.02
'I26K'	0.01	0.13	-0.39	0.04	0.15	0.48	0.26	0.17	13	0.03	0.01	0.13	0.05
'I27K'	0.51	0.19	0.16	0.04	0.23	0.61	0.13	0.13	17	0.05	0.01	0.15	0.03
'ILS'	-0.09	0.09	-0.30	0.04	0.37	0.53	-0.04	0.09	7	0.04	0.02	0.20	0.03
'ISLE'	1.27	0.10	0.32	0.10	-0.24	0.51	-0.17	0.11	23	0.02	0.02	0.11	0.02
'J18K'	-3.20	1.07	-0.67	0.03	0.00	0.55	0.13	0.11	2	0.76	0.02	0.39	0.08
'J19K'	-3.44	1.22	-0.88	0.03	-0.17	1.03	0.03	0.09	2	0.86	0.02	0.73	0.06
'J20K'	0.20	0.19	0.04	0.09	0.15	0.62	-0.03	0.10	22	0.04	0.02	0.13	0.02

'J25K'	-0.58	0.16	-0.27	0.05	0.08	0.50	0.24	0.12	25	0.03	0.01	0.10	0.02
'J26L'	0.42	0.12	0.06	0.04	0.43	0.55	0.03	0.10	27	0.02	0.01	0.11	0.02
'JOES'	-1.30	0.12	-0.47	0.04	-1.62	0.55	-0.48	0.26	4	0.06	0.02	0.27	0.13
'JUDD'	-1.23	0.13	-0.46	0.08	-0.09	0.58	0.01	0.15	16	0.03	0.02	0.15	0.04
'K17K'	-2.85	0.07	-0.71	0.03	-0.38	0.74	-0.01	0.22	1	0.07	0.03	0.74	0.22
'K20K'	0.13	0.23	0.12	0.05	0.15	0.65	0.02	0.09	22	0.05	0.01	0.14	0.02
'K24K'	-0.54	0.12	-0.15	0.04	-0.59	0.58	-0.07	0.13	15	0.03	0.01	0.15	0.03
'K27K'	1.49	0.12	0.59	0.07	0.29	0.55	0.08	0.11	28	0.02	0.01	0.10	0.02
'KALN'	0.46	0.11	0.16	0.10	-0.22	0.55	-0.18	0.14	10	0.04	0.03	0.18	0.04
'KALS'	-0.02	0.13	-0.07	0.05	-0.33	0.53	-0.26	0.15	5	0.06	0.02	0.24	0.07
'KHIT'	1.56	0.11	0.55	0.06	-0.23	0.49	-0.07	0.13	22	0.02	0.01	0.11	0.03
'KIAG'	1.27	0.16	0.39	0.08	0.28	0.64	-0.01	0.10	33	0.03	0.01	0.11	0.02
'KLU'	0.48	0.12	0.26	0.04	0.10	0.40	0.06	0.12	38	0.02	0.01	0.07	0.02
'KNK'	-0.57	0.12	-0.11	0.06	-0.19	0.45	-0.10	0.11	40	0.02	0.01	0.07	0.02
'KULT'	1.57	0.20	0.63	0.04	0.01	0.70	-0.02	0.13	7	0.08	0.01	0.26	0.05
'L17K'	-2.31	0.12	-0.43	0.04	-0.05	0.42	0.04	0.09	2	0.08	0.03	0.30	0.06
'L18K'	-2.26	0.16	-0.53	0.35	-0.31	0.79	0.11	0.09	3	0.09	0.20	0.46	0.05
'L19K'	-0.03	0.15	0.09	0.06	0.28	0.47	0.15	0.12	22	0.03	0.01	0.10	0.02
'L20K'	-0.32	0.12	-0.05	0.07	0.11	0.54	0.00	0.10	23	0.03	0.02	0.11	0.02
'L26K'	1.25	0.17	0.34	0.05	0.68	0.58	0.18	0.11	21	0.04	0.01	0.13	0.02
'L27K'	1.56	0.16	0.44	0.04	0.57	0.52	0.15	0.11	25	0.03	0.01	0.10	0.02
'LKLO'	0.43	0.23	0.31	0.07	-0.75	0.51	-0.25	0.14	15	0.06	0.02	0.13	0.04
'LOGN'	1.91	0.25	0.68	0.06	0.35	0.65	0.00	0.13	23	0.05	0.01	0.14	0.03
'LTUW'	-1.61	0.37	-0.58	0.04	-0.29	0.84	-0.07	0.11	5	0.17	0.02	0.38	0.05
'LTUX'	-0.21	0.12	0.03	0.13	-1.04	0.74	-0.28	0.16	9	0.04	0.04	0.25	0.05
'LTUY'	0.69	0.10	0.35	0.05	-0.49	0.60	-0.19	0.12	7	0.04	0.02	0.23	0.05
'M16K'	-0.31	0.12	0.14	0.03	0.18	0.37	0.05	0.11	2	0.09	0.02	0.26	0.08
'M17K'	-2.06	0.10	-0.37	0.03	-0.49	0.82	-0.16	0.10	2	0.07	0.02	0.58	0.07
'M18K'	-1.71	0.19	-0.48	0.08	0.18	0.55	-0.09	0.08	3	0.11	0.05	0.32	0.05
'M19K'	0.23	0.16	0.26	0.05	0.17	0.45	0.08	0.11	22	0.04	0.01	0.10	0.02
'M20K'	-0.15	0.26	0.01	0.07	0.08	0.58	0.06	0.11	19	0.06	0.02	0.13	0.02
'M22K'	-1.80	0.14	-0.63	0.07	-1.34	0.67	-0.28	0.14	16	0.04	0.02	0.17	0.04
'M23K'	-0.66	0.15	-0.25	0.06	-0.04	0.48	-0.04	0.12	21	0.03	0.01	0.10	0.03
'M24K'	1.17	0.11	0.51	0.15	-0.35	0.56	-0.20	0.15	16	0.03	0.04	0.14	0.04
'M26K'	1.39	0.15	0.30	0.06	0.20	0.53	0.11	0.10	24	0.03	0.01	0.11	0.02
'M27K'	1.74	0.33	0.63	0.04	0.11	0.63	0.08	0.10	20	0.07	0.01	0.14	0.02
'MCAR'	1.06	0.14	0.48	0.10	-0.05	0.52	-0.11	0.11	36	0.02	0.02	0.09	0.02
'MCK'	-1.56	0.13	-0.39	0.05	-0.23	0.60	-0.05	0.10	44	0.02	0.01	0.09	0.02
'MCR1'	0.40	0.12	0.21	0.04	-0.92	0.39	-0.25	0.12	13	0.03	0.01	0.11	0.03
'MCR2'	0.46	0.14	0.26	0.13	0.31	0.35	0.09	0.10	15	0.04	0.03	0.09	0.03
'MCR3'	0.53	0.08	0.22	0.05	0.24	0.38	0.12	0.10	15	0.02	0.01	0.10	0.03
'MCR4'	0.65	0.08	0.25	0.04	0.39	0.42	0.00	0.11	13	0.02	0.01	0.12	0.03
'MDM'	-0.77	0.12	-0.31	0.05	0.34	0.53	0.05	0.11	49	0.02	0.01	0.08	0.02

'MESA'	2.16	0.38	0.89	0.14	0.32	0.76	0.09	0.14	18	0.09	0.03	0.18	0.03
'MLY'	-0.17	0.15	0.00	0.05	0.53	0.53	0.12	0.10	41	0.02	0.01	0.08	0.02
'MPEN'	0.67	0.16	0.21	0.15	-0.93	0.66	-0.30	0.17	8	0.06	0.05	0.23	0.06
'N16K'	0.57	0.09	0.40	0.05	0.34	0.51	0.04	0.11	16	0.02	0.01	0.13	0.03
'N17K'	-0.74	0.13	-0.03	0.03	0.17	0.59	-0.13	0.08	2	0.09	0.02	0.41	0.05
'N18K'	0.24	0.17	0.18	0.07	0.16	0.57	0.03	0.10	18	0.04	0.02	0.14	0.02
'N19K'	0.08	0.12	0.08	0.12	0.39	0.56	0.05	0.10	19	0.03	0.03	0.13	0.02
'N20K'	-0.35	0.11	-0.14	0.11	0.11	0.49	-0.09	0.11	12	0.03	0.03	0.14	0.03
'N25K'	0.73	0.13	0.48	0.05	0.18	0.47	0.08	0.10	23	0.03	0.01	0.10	0.02
'NCT'	-0.74	0.11	-0.43	0.08	0.06	0.52	-0.06	0.11	16	0.03	0.02	0.13	0.03
'NEA2'	-0.98	0.12	-0.35	0.05	0.26	0.52	0.09	0.10	46	0.02	0.01	0.08	0.01
'NEB1'	1.40	0.13	0.43	0.05	-0.62	0.52	-0.20	0.13	14	0.03	0.01	0.14	0.03
'NEB2'	1.44	0.31	0.53	0.12	-0.36	0.62	-0.19	0.14	15	0.08	0.03	0.16	0.03
'NEB3'	1.35	0.17	0.38	0.04	-0.03	0.53	-0.14	0.12	14	0.05	0.01	0.14	0.03
'NICH'	1.67	0.38	0.60	0.04	0.00	0.61	0.13	0.13	12	0.11	0.01	0.18	0.04
'NNIL'	-0.14	0.10	0.11	0.12	-0.37	0.51	-0.27	0.11	8	0.03	0.04	0.18	0.04
'NSKI'	1.22	0.09	0.63	0.05	-0.54	0.41	-0.43	0.16	4	0.04	0.02	0.21	0.08
'O16K'	-0.02	0.11	-0.05	0.13	0.51	0.52	0.15	0.12	17	0.03	0.03	0.13	0.03
'O17K'	0.12	0.12	-0.03	0.06	0.17	0.49	0.04	0.10	18	0.03	0.02	0.12	0.02
'O18K'	0.08	0.08	-0.05	0.05	0.36	0.51	0.03	0.12	13	0.02	0.01	0.14	0.03
'O19K'	-0.07	0.10	-0.29	0.10	0.46	0.45	0.03	0.10	17	0.03	0.03	0.11	0.02
'O20K'	-0.96	0.34	-0.20	0.18	-0.39	0.64	0.01	0.11	11	0.10	0.05	0.19	0.03
'O22K'	-1.21	0.27	-0.40	0.06	-0.38	0.54	-0.17	0.16	13	0.07	0.02	0.15	0.05
'O28M'	1.69	0.54	0.78	0.13	0.51	0.64	0.21	0.13	11	0.16	0.04	0.19	0.04
'P16K'	0.02	0.11	-0.03	0.11	-1.30	0.57	-0.25	0.15	12	0.03	0.03	0.17	0.04
'P17K'	-0.55	0.13	-0.26	0.10	-0.51	0.55	-0.16	0.12	16	0.03	0.03	0.14	0.03
'P18K'	-1.01	0.14	-0.44	0.10	0.02	0.52	0.11	0.10	17	0.03	0.02	0.13	0.02
'P19K'	-0.26	0.13	-0.10	0.06	0.14	0.67	0.03	0.10	9	0.04	0.02	0.22	0.03
'P23K'	1.02	0.15	0.13	0.11	-0.22	0.40	-0.04	0.11	8	0.05	0.04	0.14	0.04
'PAX'	-0.37	0.13	-0.10	0.05	0.40	0.46	0.17	0.10	49	0.02	0.01	0.07	0.01
'PIN'	2.09	0.36	0.48	0.10	0.70	0.76	0.10	0.15	23	0.08	0.02	0.16	0.03
'PPD'	-0.10	0.18	-0.09	0.06	0.61	0.51	0.20	0.17	31	0.03	0.01	0.09	0.03
'PPLA'	-0.89	0.14	-0.13	0.05	-0.29	0.55	-0.09	0.13	35	0.02	0.01	0.09	0.02
'PTPK'	1.48	0.17	0.78	0.05	-0.23	0.54	-0.08	0.12	25	0.03	0.01	0.11	0.02
'PWL'	-1.17	0.13	-0.46	0.05	-0.33	0.59	-0.03	0.11	29	0.02	0.01	0.11	0.02
'Q16K'	-0.73	0.11	-0.31	0.05	-0.72	0.51	-0.13	0.16	12	0.03	0.01	0.15	0.04
'Q19K'	-1.09	0.18	-0.37	0.06	-0.19	0.76	-0.20	0.12	9	0.06	0.02	0.25	0.04
'Q20K'	-0.29	0.18	-0.03	0.08	-0.13	0.87	-0.10	0.15	8	0.06	0.03	0.31	0.05
'Q23K'	1.34	0.06	0.29	0.09	-0.01	0.56	0.14	0.16	4	0.03	0.05	0.28	0.08
'R16K'	-1.14	0.14	-0.46	0.28	-1.32	1.07	-0.34	0.24	5	0.06	0.12	0.48	0.11
'R17K'	-0.31	0.12	-0.16	0.10	-0.05	0.60	0.04	0.14	9	0.04	0.03	0.20	0.05
'R18K'	1.76	0.15	0.45	0.04	0.00	0.28	-0.22	0.07	1	0.15	0.04	0.28	0.07
'RC01'	-1.37	0.13	-0.46	0.07	-0.10	0.60	-0.02	0.11	32	0.02	0.01	0.11	0.02

'RED'	-0.70	0.11	-0.46	0.05	0.15	0.53	-0.02	0.12	21	0.02	0.01	0.12	0.03
'RH01'	-0.56	0.12	-0.14	0.04	0.50	0.45	0.17	0.11	12	0.03	0.01	0.13	0.03
'RH03'	-0.41	0.11	-0.26	0.09	0.59	0.46	0.27	0.10	19	0.03	0.02	0.11	0.02
'RH04'	-0.42	0.13	-0.30	0.05	0.25	0.41	0.18	0.09	17	0.03	0.01	0.10	0.02
'RH05'	0.19	0.24	0.16	0.11	-0.31	0.61	-0.13	0.13	12	0.07	0.03	0.18	0.04
'RH06'	0.60	0.23	0.16	0.16	-0.46	0.64	-0.11	0.13	9	0.08	0.05	0.21	0.04
'RH07'	0.89	0.12	0.39	0.10	-0.62	0.43	-0.25	0.12	7	0.05	0.04	0.16	0.04
'RH08'	0.62	0.13	0.28	0.07	-0.87	0.43	-0.21	0.12	14	0.04	0.02	0.11	0.03
'RH09'	0.38	0.11	0.21	0.04	-0.44	0.46	-0.20	0.13	14	0.03	0.01	0.12	0.04
'RH10'	0.50	0.10	0.26	0.04	-0.41	0.39	-0.13	0.13	15	0.03	0.01	0.10	0.03
'RH11'	0.48	0.10	0.18	0.05	0.11	0.41	-0.02	0.10	16	0.03	0.01	0.10	0.03
'RH12'	0.46	0.13	0.13	0.08	0.40	0.36	0.09	0.11	15	0.03	0.02	0.09	0.03
'RH13'	0.37	0.14	0.08	0.04	0.29	0.34	0.06	0.11	12	0.04	0.01	0.10	0.03
'RH14'	0.19	0.13	-0.05	0.05	0.23	0.44	0.05	0.10	16	0.03	0.01	0.11	0.02
'RH15'	0.07	0.10	-0.13	0.05	-0.46	0.45	-0.33	0.13	13	0.03	0.01	0.12	0.04
'RIDG'	-0.34	0.11	-0.11	0.05	-0.37	0.51	-0.05	0.10	30	0.02	0.01	0.09	0.02
'RKAV'	2.30	0.46	0.84	0.13	0.46	0.56	0.10	0.13	8	0.16	0.04	0.20	0.05
'SALA'	-0.42	0.17	0.01	0.27	-0.49	0.77	-0.25	0.17	7	0.06	0.10	0.29	0.07
'SAMH'	2.40	0.33	1.04	0.25	0.13	0.74	0.16	0.13	13	0.09	0.07	0.21	0.04
'SAW'	-0.69	0.13	-0.23	0.06	-0.36	0.46	-0.18	0.12	42	0.02	0.01	0.07	0.02
'SCM'	-0.10	0.11	0.02	0.05	-0.41	0.44	-0.16	0.12	35	0.02	0.01	0.07	0.02
'SCRK'	0.27	0.12	0.11	0.05	0.42	0.51	0.16	0.10	53	0.02	0.01	0.07	0.01
'SKN'	-1.71	0.21	-0.63	0.05	-0.07	0.58	0.24	0.12	23	0.04	0.01	0.12	0.03
'SLK'	-1.54	0.19	-0.47	0.05	-0.24	0.62	0.01	0.11	27	0.04	0.01	0.12	0.02
'SOLD'	0.95	0.12	0.53	0.07	-0.17	0.53	-0.22	0.12	9	0.04	0.02	0.18	0.04
'SPBG'	0.36	0.17	-0.36	0.07	1.12	0.87	-0.15	0.12	11	0.05	0.02	0.26	0.04
'SPCG'	-0.30	0.11	-0.05	0.04	0.27	0.59	0.08	0.12	12	0.03	0.01	0.17	0.04
'SPCN'	-0.04	0.18	-0.19	0.06	-0.48	0.70	-0.26	0.15	9	0.06	0.02	0.23	0.05
'SPCP'	0.92	0.33	0.10	0.04	0.28	0.56	-0.18	0.16	6	0.13	0.02	0.23	0.07
'SPCR'	-0.31	0.12	-0.17	0.05	0.38	0.51	0.07	0.11	21	0.03	0.01	0.11	0.02
'SPNN'	-1.39	0.15	-0.66	0.03	0.35	0.60	0.44	0.17	1	0.15	0.03	0.60	0.17
'SSP'	1.80	0.16	0.86	0.16	0.03	0.49	0.01	0.12	10	0.05	0.05	0.16	0.04
'TCOL'	-0.93	0.12	-0.38	0.05	0.12	0.49	0.13	0.11	29	0.02	0.01	0.09	0.02
'TOK1'	0.13	0.15	-0.10	0.05	0.00	0.41	0.07	0.10	22	0.03	0.01	0.09	0.02
'TOK2'	0.34	0.13	-0.02	0.08	0.25	0.41	0.18	0.10	21	0.03	0.02	0.09	0.02
'TOK3'	0.84	0.16	0.22	0.08	0.42	0.46	0.10	0.10	17	0.04	0.02	0.11	0.02
'TOK4'	1.29	0.16	0.43	0.06	0.25	0.48	0.25	0.10	20	0.04	0.01	0.11	0.02
'TOK5'	0.86	0.13	0.29	0.19	0.17	0.45	0.05	0.10	16	0.03	0.05	0.11	0.02
'VRDI'	0.86	0.14	0.39	0.05	0.39	0.43	0.12	0.10	34	0.02	0.01	0.07	0.02
'WACK'	1.04	0.10	0.61	0.05	-0.16	0.52	-0.10	0.11	10	0.03	0.01	0.16	0.03
'WAT1'	-1.65	0.10	-0.53	0.05	-0.06	0.52	0.09	0.10	32	0.02	0.01	0.09	0.02
'WAT2'	-1.25	0.09	-0.52	0.06	-0.24	0.47	0.18	0.07	3	0.05	0.03	0.27	0.04
'WAT3'	-0.16	0.17	-0.25	0.09	-1.09	0.84	-0.04	0.04	1	0.17	0.09	0.84	0.04

'WAT4'	-1.19	0.07	-0.36	0.03	0.21	0.34	0.12	0.09	2	0.05	0.02	0.24	0.07
'WAT5'	-0.38	0.13	-0.08	0.54	-0.31	0.41	0.31	0.08	2	0.09	0.38	0.29	0.06
'WAT6'	-1.01	0.10	-0.15	0.05	0.16	0.47	0.07	0.10	45	0.02	0.01	0.07	0.01
'WAT7'	-1.70	0.10	-0.49	0.04	-0.12	0.61	0.06	0.11	38	0.02	0.01	0.10	0.02
'WAX'	1.72	0.18	0.65	0.05	0.04	0.55	-0.01	0.11	21	0.04	0.01	0.12	0.02
'WFLS'	-0.26	0.15	-0.06	0.04	0.40	0.75	0.33	0.11	16	0.04	0.01	0.19	0.03
'WFLW'	-0.16	0.14	-0.08	0.04	0.45	0.73	0.27	0.09	13	0.04	0.01	0.20	0.03
'WRH'	-1.14	0.12	-0.41	0.06	0.33	0.62	0.21	0.12	38	0.02	0.01	0.10	0.02
'YAH'	1.96	0.19	0.88	0.11	-0.12	0.60	-0.03	0.12	22	0.04	0.02	0.13	0.03